Design of a Planar Resonant Force Sensor with an application to Cell Mechanics

Denis Desmaële

Thèse de Doctorat présentée à

L'UNIVERSITÉ PIERRE ET MARIE CURIE

UPMC
SORBONNE UNIVERSITÉS

pour obtenir le grade de

DOCTEUR D'UNIVERSITÉ

Spécialité: **Sciences Mécaniques, Acoustique, Électronique et Robotique**

Design of a planar resonant force sensor with an application to cell mechanics

par **Denis Desmaële**

Soutenue le 13 décembre 2011 devant la commission d'examen :

Rapporteurs:	M. **Kallio Pasi**	Professeur, TUT, Tampere, Finlande
	Mme. **Prelle Christine**	Maître de Conférences (HDR), UTC, Compiègne
Examinateurs:	M. **Gautier Gérard**	Docteur, Laboratoire SYMME, Annecy-le-Vieux
	M. **Pouget Joël**	Professeur, UPMC-IJLRA, Paris
Directeur de thèse:	M. **Régnier Stéphane**	Professeur, UPMC-ISIR, Paris
Co-encadrant:	M. **Boukallel Mehdi**	Docteur-Ingénieur, CEA-LIST, Fontenay-aux-Roses

Doctoral dissertation submitted to the

UNIVERSITÉ PIERRE ET MARIE CURIE

UPMC
SORBONNE UNIVERSITÉS

for the degree of

DOCTOR OF PHILOSOPHY

in **Robotics**

Design of a planar resonant force sensor with an application to cell mechanics

presented by **Denis Desmaële**

the 13th of December 2011

Doctoral Committee:

Reviewers:	Mr. **Kallio Pasi**	Professor, TUT, Tampere, Finland
	Ms. **Prelle Christine**	Associate Professor (HDR), UTC, Compiègne
Examiners:	Mr. **Gautier Gérard**	Doctor, SYMME Laboratory, Annecy-le-Vieux
	Mr. **Pouget Joël**	Professor, UPMC-IJLRA, Paris
Advisor:	Mr. **Régnier Stéphane**	Professor, UPMC-ISIR, Paris
Co-advisor:	Mr. **Boukallel Mehdi**	Researcher, CEA-LIST, Fontenay-aux-Roses

Contents

List of Figures

Introduction

Context of the work

Living cells are the basic building blocks of all living organisms. Notwithstanding their microscopic size and their apparent simple anatomy, cells turn out to be real miniature protein factories capable of performing all the functions of life. Thereby, cells express genetic information, synthesize, sort, store and transport biomolecules. Cells, however, are far from being governed exclusively by biochemical reactions. They also transduce signals, maintain internal structures, and respond to external environments. Many of these processes actually involve mechanical aspects.

Within a living body, cells are indeed constantly exposed to various mechanical forces. For example, during human locomotion, tensile muscular forces and compressive loads act on cartilage and bones cells [1]. Heart cells are stretched during beating. Lung cells also experience stretching cycles during breathing [2]. Cells lining the interior walls of blood vessels are constantly subjected to pulsatile and continuous shear stresses from blood flows. Red blood cells (RCBs) can be subjected to about 100% deformation as blood flows through narrow capillaries [3].

The presence of such mechanical forces in the cell environment plays a dominant role in the cell behavior [4]. In fact, any alteration of the mechanical forces that cells undergo may cause a disruption in their normal functioning. Thereby, many normal and diseased conditions of cells are dependent on or regulated by their mechanical environment [3]. By way of illustration, slow stretching of the axon of neural cells helps neural cell growth, whereas severe stretching of the axon that occur during traumatic brain injury causes cell death [3]. Likewise, mechanical forces may induce profound effects on cellular functions as essential as growth, proliferation, contractility, migration or differentiation [1, 5, 6].

Cells can indeed sense, react and adapt themselves to mechanical forces. Mechanical and biochemical cues occurring at the cellular level actually prove to be intimately correlated through reciprocal mechanochemical conversion pathways. Thereby, cells can
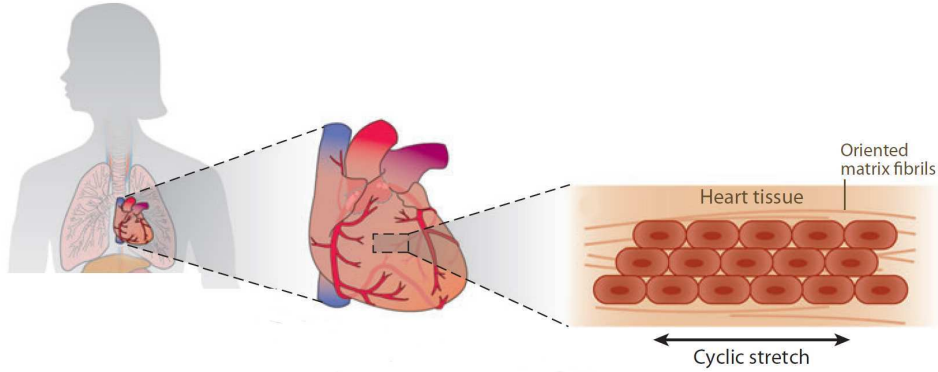
Figure 1: In a human body, mechanical forces are ubiquitous. For instance, heart cells are constantly exposed to stretching cycles during heart beating. Illustration adapted from [2].

convert mechanical forces into biological responses. Reciprocally, biological and biochemical signals are known to influence the abilities of cells to sense, generate and bear mechanical forces.

Decades ago, early studies already attempted to investigate the effects of mechanical forces on cells. To that purpose, a variety of laboratory apparatuses aimed at reproducing mechanical forces that cells experience in their physiological environment were developed. Such apparatuses (see [7] for a comprehensive review) usually controlled the delivery of a mechanical input such as hydrostatic pressure, fluid shear stress, or substrate strain. However, the mechanical input could solely be applied to large tissue cultures. From the analysis of tissue cultures, the response of a particular cell could not be easily decoupled from the response of the entire cell population. The heterogeneity among cell responses was hence largely ignored.

The possibility to study isolated cells then appeared as a next crucial step to thoroughly study various mechanical aspects of cells and gain new biological insights. Both life sciences and engineering communities have been highly involved in the development of systems capable of interacting with a single cell. In particular, systems produced via microfabrication processes are today increasingly used to uncover the fundamental ways in which cells function. Micrometer-scale actuators and sensors indeed prove to be ideal interfaces to decipher how single cells receive and process extracellular mechanical signals. By essence, dimensions of these actuators/sensors are in the same order of magnitude than the sizes of most cells. They also exhibit a high functional density and the possibility to be associated with fluidic parts to create more *in-vivo* like environments in *in-vitro* settings.

In this dissertation, one is especially interested in taking advantages of the potential benefits brought by such microsystems for measuring the elastic modulus (i.e., Young's

9

modulus) of individual living cells. Scientific evidences have indeed recently revealed connections between alterations in the elastic modulus of single cells and pathophysiological states [8]. Thereby, a dramatically reduced Young's modulus is a characteristic feature of cancerous cells. By contrast, RCBs infected by malaria have a significantly higher Young's modulus than their healthy counterparts.

The elastic modulus of cells hence appears as a meaningful marker to differentiate pathogenic cells and healthy cells. For diagnostic purposes, knowing the Young's modulus of cells may hence help to detect the presence of cancer as well as other cell-based degenerative diseases at earlier stages. Besides, elasticity measurements also have the potential to disclose the specific effects of pharmaceuticals at the cellular level. Therefore, cell elasticity measurements may also prove advantageous in drug development. Nevertheless, to use the Young's modulus of cells as a reliable indicator, challenges still need to be addressed. This dissertation proposes to discuss these challenges and reports the design of a novel structure aimed at bringing new solutions to the restrictions encountered so far.

Dissertation contributions and outline

To date, the use of resonant structures in cell analysis is restricted to the detection of target biomolecules. In this context, structures that exploit resonance phenomena permit to achieve exquisite mass sensitivity. Nonetheless, extracting the Young's modulus of cells imposes additional constraints. In particular, the cell to be probed must be deformed by a known force. As a result, most micrometer-scale tools and devices that can deform individual cells or/and measure the cell response operate today in a static mode.

By contrast, this dissertation proposes a novel structure specifically adapted for measuring forces applied to living cells and extract their Young's modulus via a dynamic mode. In particular, the resonant structure does not need to be immersed into liquids for measuring the Young's modulus of cells. Major energy losses are thereby avoided, and higher performances offered by resonance phenomena can be exploited. In the mean time, cells can be preserved in culture medium directly within the structure. The structure presented also proposes solutions for dealing with different types of cells as well as for increasing measurement rates.

To discuss in details the key features and potential advantages of this new structure, this doctoral dissertation is structured in four main chapters:

- Chapter 1 is intended to provide a global overview of microfabricated tools that can deform individual cells or/and measure the cell response. Through the review of a large panel of systems that have been reported in the literature, Chapter 1 highlights and discusses specific constraints encountered in the context of cell anal-

ysis. Compared to existing devices, the potential advantages of resonant beams for measuring cell forces and extracting the cell Young's modulus are pointed out.

- Chapter 2 discusses a first case of study where one tries to take advantage of a clamped-clamped beam resonator for measuring the interaction force with a cell. Problems faced by such a simple beam in the context of cell analysis are theoretically investigated. In particular, the presence of a surrounding fluid is analyzed and it is demonstrated that such a simple beam cannot be satisfyingly used for determining the Young's modulus of a cell.

- Chapter 3 constitutes the heart of the work presented in this dissertation. It introduces the new resonant structure designed for extracting the Young's modulus of cells while taking into consideration the set of limitations identified in Chapter 1 and Chapter 2. The whole concept of the structure is explained as well as its key features and advantages. To grasp valuable insights into its working principle, energy methods are used to theoretically investigate its static and dynamic behaviors. Numerical applications are also provided to predict its performances.

- Chapter 4 reports the fabrication of a first prototype of the new structure introduced in Chapter 3. The whole experimental arrangement used for its characterization is described. Performances predicted by theory are confronted to experimental results. The possibility to conduct experiments with biological samples is also demonstrated. Coupled to a flat indenter, the prototype is used to compress a round suspension cell. An experimental method is detailed to rapidly extract the Young's modulus of the cell without the need of a descriptive model.

Finally, a general conclusion summarizes the work developed and the results obtained throughout the dissertation. This last part also discusses future work that could be addressed.

Chapter 1

Microfabricated tools for conducting mechanical studies on individual cells: state-of-the art

Since the 1990s, mechanical studies conducted on isolated cells have permitted to gain new insights into complex cellular processes. With recent technological advances, different types of actuators and sensors can today be fabricated at the micrometer-scale. With feature sizes that inherently match the sizes of most cells, such microfabricated tools appear as ideal interfaces to conduct mechanical studies at the cell level. Moreover, microactuators or/and microsensors have the potential to be combined in a single miniature package. With such a miniature unit, accurate stimulation of individual cells and quantitative measures of cellular responses can be obtained with high spatial and temporal resolutions. Microfabrication processes also permit to integrate fluidic components. More *in-vivo* like environments can be created in *in-vitro* experimental settings, and forces that cells face in their physiological environment can be mimicked more realistically. For all these reasons, microfabricated systems have been increasingly used to study various mechanical aspects of cells.

The first aim of this chapter is to provide an updated overview of such tools. Prior to their review, some fundamentals on the architecture of living cells are first reminded in Section 1.1. Then, Section 1.2 surveys a large panel of systems dedicated to cell mechanics that have been recently reported in the literature. Systems providing mechanical stimulation to cells are enumerated in Section 1.2.2 whereas devices sensing various cell mechanical features are listed in Section 1.2.3. Next, Section 1.3 provides three discussions. Section 1.3.1 introduces problems encountered due to the nature and the number of cells that must be probed. Section 1.3.2 emphasizes on specific constraints naturally imposed by the cell environment. Section 1.3.3 discusses different types of biophysical parameters that are usually investigated. It also highlights the importance of the cell Young's modulus. To conclude, Section 1.4 summarizes the chapter and emphasizes

challenges that will be more specifically addressed in the context of this thesis.

1.1 The cell architecture: some fundamentals

In the context of cell mechanical studies, this section only covers most important cellular structures that are known to play a more dominant role in the mechanical properties and mechanical integrity of the cell.

Cells involved in most mechanical studies are mammalian cells (i.e., eukaryote cells). As illustrated in Fig. 1.1, mammalian cells are surrounded by a plasma membrane, providing a barrier between the internal and the external environment. It consists of a double layer of phospholipids (lipid bilayer). The exposed heads of the bilayer are hydrophilic, whereas hidden tails of the phospholipids are hydrophobic, so the cell membrane acts as a protective barrier to the uncontrolled flow of water. The membrane is made more complex by the presence of numerous proteins. Proteins are crucial to cell activity and regulate entrance and exit of specific molecules into and out of the cell.
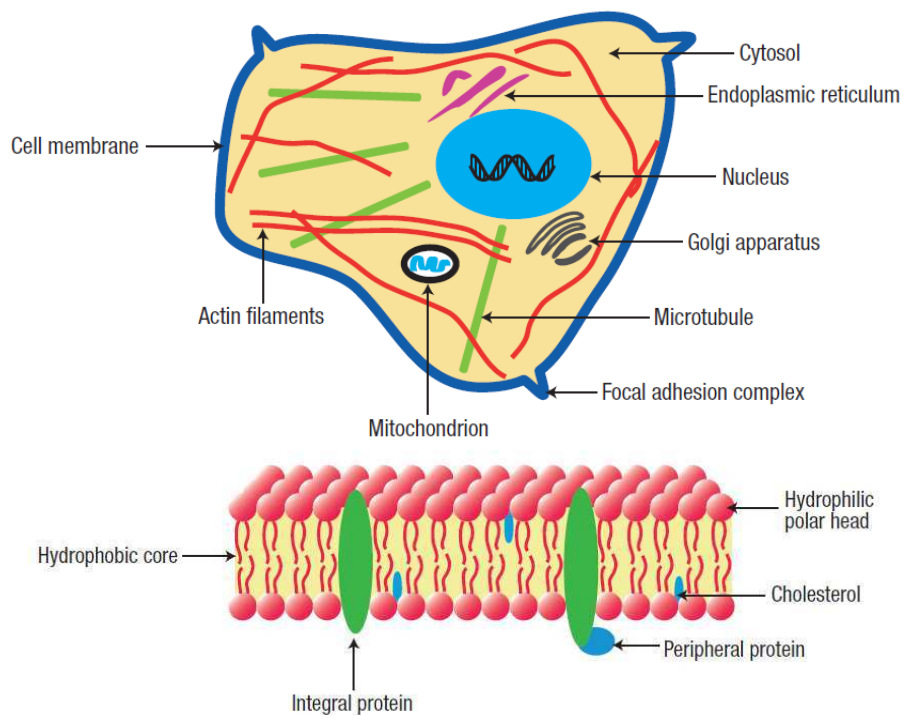
Figure 1.1: Top: schematic diagram of a typical eukaryote cell, which contains many subcellular elements. Bottom: drawing detailing the constitution of the cell membrane. Illustrations adapted from [3].

The interior of mammalian cells is filled with a semi fluid medium called cytoplasm.

The cytoplasm is composed of the largely aqueous cytosol and cell organelles. Organelles (e.g., mitochondrion, endoplasmic reticulum, etc.) act as small organs that are adapted and/or specialized for carrying out one or more vital cell functions.

The cytoplasm also surrounds the nucleus. The nucleus is of primary importance because it stores the genetic material which governs the characteristics of the cell and its metabolic functioning. It is a prominent structure with a typical diameter of about 5 μm. The nucleus has a spherical shape and is separated from the cytoplasm by the nuclear envelope surrounding the nucleoplasm, with distinct components such as the inner and outer nuclear membrane, the nuclear lamina, and the nuclear pore complexes. From a structural point of view, the nucleus is mechanically stiffer than the cell cytoplasm.

Nearly all cellular structures are connected through the cytoskeleton, a complex network of protein filaments extending throughout the entire cell. The cytoskeleton is involved in regulating cell shape, resistance to deformation, and elasticity as well as in active processes such as cell division, locomotion, and the transport of intracellular particles. The cytoskeleton is also believed to be involved in many cell signaling processes. It consists of three main components: the microfilaments (actin filaments), the microtubules, and to a lesser extend, the intermediate filaments.

As explained in [9], actin filaments assemble in a variety of structures including isotropic networks of filaments within the cytoplasm, contractile actin filament bundles often called stress fibers and highly organized parallel arrays of filaments in such structures as microspikes (thin, stiff protrusions of the plasma membrane) and lamellipodia (sheet-like extensions on the cell surface). Actin filaments are thin, typically 8 nm in diameter, flexible and appear to be the most resistant of the cytoskeleton elements to deformation.

Microtubules are long, hollow, rigid cylinders with extreme outer and inner diameters of 30 and 18 nm respectively, and with lengths of up to and exceeding 100 μm. They extend throughout the cytoplasm and determine the location of membranebound organelles and other cell components. It is believed that microtubules serve as stabilizing elements within a network of the other two cytoskeletal filaments. Although individual microtubules are stiff and rigid over cellular dimensions, microtubule networks are easily deformed and begin to flow when stretched beyond 50% of their original length.

Intermediate filaments are tough and durable fibrous proteins which are organized in ropelike arrays and have a typical diameter of 10 nm, intermediate between thin actin filaments and thick microtubules. They can be found around the nucleus, extending out through the cytoplasm and eventually forming close associations with the cell membrane at the cell adhesion sites. Moreover, intermediate filaments also appear as a fibrous protein meshwork underlying the inner nuclear membrane. These so-called nuclear lamins are believed to be connected to the nuclear membrane and other cytoskeletal elements.

Intermediate filaments are specifically found in cells, which are regularly subjected to mechanical stresses, like epithelial cells and all kinds of muscle cells. Moreover, disassembly of intermediate filaments is accompanied by dramatic changes in shape and mechanical properties of the cell.

It will go far beyond the purpose of this dissertation to describe in further details the cell anatomy and physiology. Although not exhaustive, the description of the cell interior provided above however allows one to realize the level of mechanical complexity of the cell architecture. The mechanical study of cells is further complexified by the fact that mammalian cells actually come in a wide variety of shapes and sizes. Indeed, if Fig. 1.1 represents an adherent cell, experiments can also involve suspension cells. In Table 1.1, some essential differences between adherent and suspension cells are enumerated.

	Adherent cells	Suspension cells
Property	Need to anchor to an underlying substrate	Evolve in suspension, not attached to a surface
Shape	Highly irregular	Mostly spherical
Size	~20-30 μm	RBCs: 8-12 μm Embryos - Oocytes: 100 - 600 μm

Table 1.1: Essential differences between the two main types of living cells manipulated by MEMS for conducting mechanical experiments.

1.2 Overview of microfabricated tools for conducting mechanical studies on individual cells

1.2.1 Preliminary remarks

The author now surveys different types of microfabricated tools that have been reported for conducting mechanical studies on individual cells. For the sake of clarity and conciseness, these microfabricated tools will now be referred as microelectromechanical systems (MEMS). By essence, the acronym MEMS is however a broad definition. Throughout the thesis, the terminology MEMS employed will refer to systems that encompass electrical, mechanical, but also optical or fluidic parts manufactured via microfabrication

processes. In particular, focus will be given on MEMS with a high functional density, namely MEMS that try be as portable and autonomous as possible by maximizing the integration of actuation or/and sensing capabilities in a compact single-chip piece.

Therefore, devices such as micropipettes [10, 11, 12], microcantilevers used in atomic force microscopes (AFM) [13, 14, 15, 16, 17, 18], microplates [19, 20, 21, 22, 23] or microindenters [24, 25, 26] will not be described in details in this chapter (further details can be found in several relevant reviews [7, 27, 28, 29, 30, 31, 32, 33]). Notwithstanding the presence of microscopic components, actuators (e.g., positioning stages) and measurement means (e.g., microscopes, cameras, etc.) utilized in these systems are all distant (off-chip) from the extremity entering in contact with the cells. Besides, such tools are usually considered as experimental techniques or laboratory apparatus by the research community (see for instance classifications adopted in [2, 32]).

The choice to exclude micropipettes, AFM cantilevers, microplates or microindenters is representative of the difficulty to adopt a proper classification for introducing MEMS dedicated to cell mechanics. This classification is further complexified by the fact that a broad class of cell mechanical studies can be carried out. These studies may concern how cells move, deform and interact, as well as how cells sense, generate, and respond to mechanical forces. Accordingly, a large variety of MEMS can be found in the literature.

However, in many cell studies, stresses (i.e., forces) or/and strains (i.e., deformations) must be imposed or/and measured. Hereafter, Section 1.2.2 first lists several MEMS that encompass actuation means capable of imposing stresses/strains on cells. Then, Section 1.2.3 reports MEMS capable of measuring stresses/strains developed during cell responses.

1.2.2 MEMS encompassing actuation means

In this section, it is pointed out that, to avoid too many confusing subcategories, no particular distinction is made between MEMS applying a prescribed force or a prescribed displacement. Similarly, MEMS that provide stimulation globally (i.e., a stress/strain is provided to the entire cell structure) or locally (i.e., only a given cellular region is excited) are not dissociated. In addition, MEMS that target adherent cells or suspension cells (see Section 1.3.1) are not differentiated. Finally, auxiliary equipment (e.g., laser sources, peristaltic pumps, electric power supplies) are not considered.

1.2.2.1 Electrostatic comb drives

In [34, 35], interdigitated comb fingers exploiting electrostatic phenomena were used to carry out stress-strain experiments on individual collagen fibrils. A multidimensional approach based on a single linear electrostatic structure was also reported by Scuor et al. [36], who conceived a micro in-plane biaxial cell stretcher (see Fig. 1.2). The quadrants of a sliced circular plate were actuated in mutually-orthogonal directions, that is to say
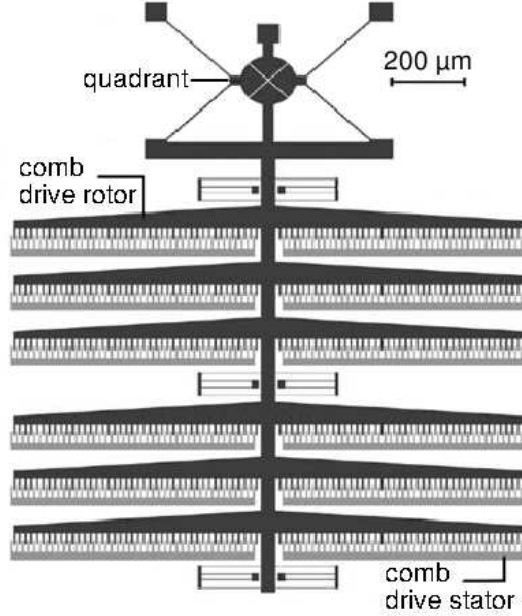
Figure 1.2: Illustration of a comb drive system actuating a bi-axial cell stretcher. Drawing adapted from [36].

that the quadrants moved in horizontal and vertical directions simultaneously. The net force developed by such a comb drive actuator is given by

$$F_{electro} = N_{ce} \left(\frac{\epsilon \, t_{ce}}{g_{ce}} \right) U^2 \tag{1.1}$$

where N_{ce} is the number of comb electrodes, ϵ is the permittivity constant of the dielectric medium, t_{ce} is the comb thickness, g_{ce} is the comb electrode gap and U is the driving voltage. Theoretically, Scuor et al. claimed that a nominal voltage of 100 V permitted such an electrostatic structure to generate actuation forces up to $60 \, \mu$N. In practice, only translation amplitudes of the plate were reported. In ambient conditions, a power supply of 100 V led to a maximum space between the quadrants of 3.4 μm.

1.2.2.2 Electrothermal beams

Thermal expansion caused by electric currents heating up the material of a microstructure constitutes a well known actuation principle used in MEMS [37, 38, 39, 40]. In particular, large rectilinear displacement parallel to the device substrate can be achieved with *chevron* (or V-shaped beam) configurations. Such a compliant beam is depicted in Fig. 1.3.

17
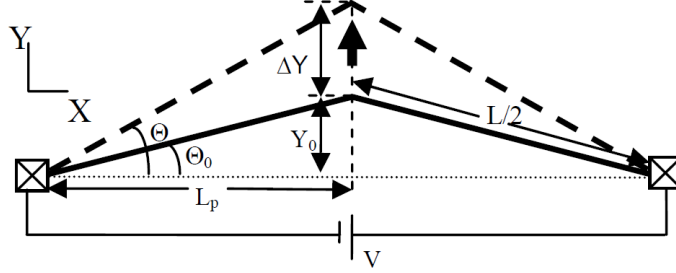
Figure 1.3: Main dimensions of a V-shaped beam (*or chevron*) anchored at its two ends: Joules heating causes thermal expansion and pushes the apex outward when an electric current passes through the structure [41].

Displacement of the beam apex ΔY can be approximated via the formula [42]

$$\Delta Y = \left(\frac{L + \Delta_L}{2} \right) \sin \left[\arccos \left(\frac{2 L_p}{L + \Delta_L} \right) \right] - Y_0 \tag{1.2}$$

where L is the total beam length, L_p is the X axis projection of $L/2$, and Δ_L is the increment in length of the beam which can be expressed by

$$\Delta_L = \frac{\alpha \, L^3}{12 \, k \, Tb_{vol} \, r_{tb}} U^2 \tag{1.3}$$

In equation 1.3, α is the thermal expansion coefficient, k is the thermal conductivity, U is the voltage applied between anchors, Tb_{vol} is the volume of the beam, and r_{tb} is the electrical resistance of the beam. Multiple pairs of such V-shaped beams can be serially combined in order to reach higher force displacement. Indeed, for small displacement, the total actuation force of several V-shaped beams can be approximated by

$$F_{therm} = N_{tb} \frac{E \, b^3 \, h}{4 \, L^3} \Delta Y \tag{1.4}$$

where E is the Young's modulus, b and h are the width and thickness of the beam, whereas N_{tb} is the number of beams.

Compression of a mouse fibroblast (NIH3T3) with an array of five *chevrons* has been reported by [43] (see Fig. 1.4). This miniature cell loading system was power supplied either by low continuous voltages (≤ 2 V) when operating in air, or by high frequency (800 kHz) sinusoidal voltages in liquids. In ambient conditions, it offered a maximum translation along one direction of $9 \, \mu$m. This MEMS allowed the authors to apply compressive strains up to 25% of the initial cell size.

1.2.2.3   Electro-active polymers

Electro-active polymers (EAP) are polymers that change in shape or size in response to an electrical stimulation. In [44], an array of 100x100 μm^2 EAP microactuators was
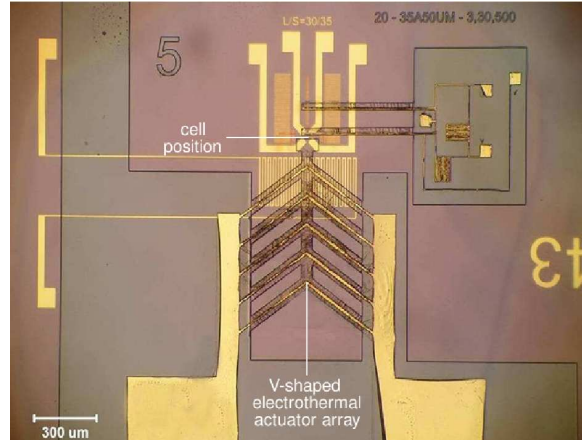
Figure 1.4: Electrothermal MEMS cell loader designed for measuring the compliance of cells. Image adapted from [43].

built to perform the individual stretching of 128 cells. In this array (see Fig. 1.5), compliant gold electrodes ($100\,\mu$m wide) were deposited by low energy ion implantation on each side of a $30\,\mu$m thick, 30% pre-stretched, PDMS (polydimethylsiloxane) membrane. Next, the membrane was placed over a rigid PDMS support composed of $200\,\mu$m wide channels. The membrane provided flexibility and could expand over the channels when high voltages were applied to the electrodes. This design permitted to restrict the stimulation areas to intersections between electrodes and channels. Although this technique was not applied to living cells, the investigators predict that each cell could potentially receive up to 10-20% uniaxial strains.
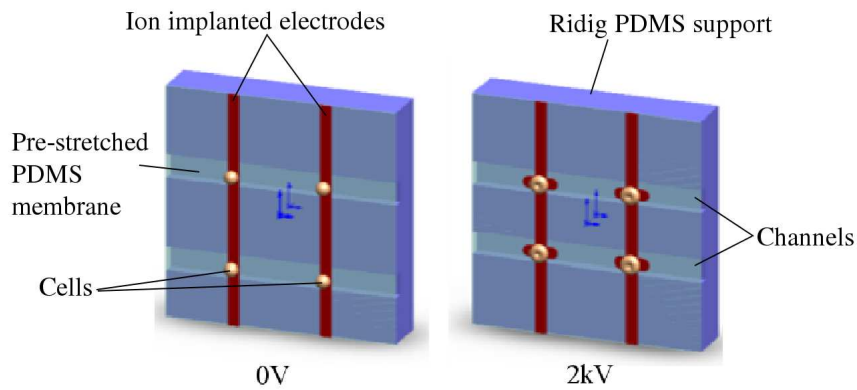
Figure 1.5: Concept of an array of EAP microactuators. Left: device at 0V with four cells placed at the intersection between electrodes and channels. Right: device when high voltage (2kV) is applied; the four cells are stretched along the channels. Drawings adapted from [44].

19

1.2.2.4 Magnetic fields

Magnetic fields have been used for studying the physical properties of cell cultures since the 1950s [45]. Recently, microscopic magnetic manipulators able to locally stress an isolated cell have been reported [46, 47, 48, 49]. For instance, in [50, 51], the authors implemented three magnetic micropoles on a glass substrate (see Fig. 1.6) in order to enable the multidimensional stimulation of one cell. Each pole tip was $4\,\mu$m wide, 6 μm thick and had a surface roughness of $0.5\,\mu$m. Poles spacing was about $20\,\mu$m to ensure the placement of a single cell between them. As in conventional magnetic tweezers (MT) (e.g., [52, 53, 54, 55]) precise forces could be applied on magnetic microbeads attached to the cell membrane. Indeed, in the presence of a spatially varying magnetic field, the force F_{mag} experienced by such a magnetic bead is

$$F_{mag} = \nabla(M_{mb} \cdot B) \tag{1.5}$$

where M_{mb} is the magnetic moment of the microbead and B is the magnetic flux density. By controlling the amplitude and the direction of the magnetic flux gradient generated at the center of the three micropoles, de Vries et al. validated actuation forces >100 pN on a magnetic microbead ($\sim$500 nm radius) injected inside the nucleus of a HeLa cell [56].
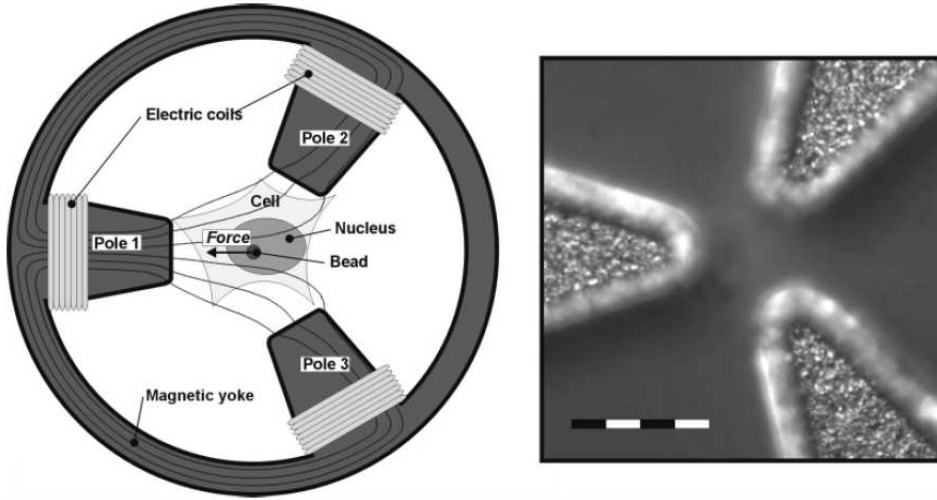
Figure 1.6: Left: Principle of the magnetic MEMS setup designed by de Vries et al.: a cell anchored to a glass plate and embedding a magnetic microbead is placed between the tips of magnetic poles. Right: Light microscopy image showing the extremities of the magnetic micropoles. Scale bar equals 20 μm. Images from [56].

Magnetic fields have also been used to actuate a dense array of vertical microposts [57, 58]. Each post measured 1.5 μm in radius, 10 μm in height and had a low stiffness of 32 nN/μm. Posts were also closely spaced with a pitch of 9 μm. Magnetic cobalt nanowires (350 nm in diameter, 5-7 μm long) were incorporated within some posts during the fabrication process of the array (1 nanowire per 200 posts). External NdFeB
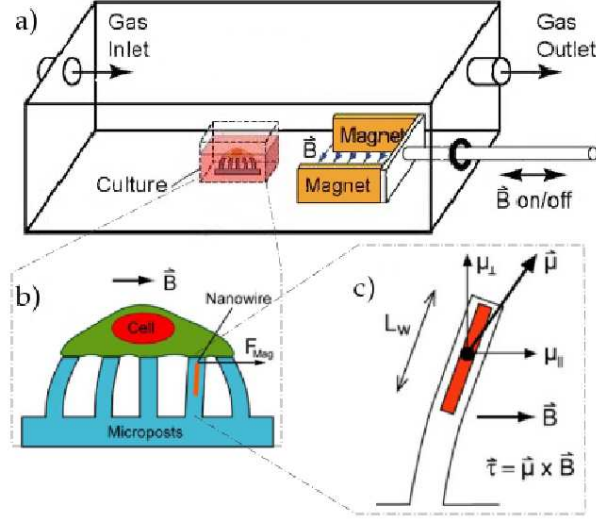
Figure 1.7: a) Micropost array of Sniadecki et al. where permanent magnets are used to bend magnetized posts. b) Close-up of the post array: an adherent cell is lying on the top of the posts, one of them incorporating a magnetic nanowire. c) Parameters influencing the bending of the magnetic post in accordance with Eq. (1.6). Drawings adapted from [57, 58].

magnets were used to generate a horizontal uniform magnetic field. This magnetic field attracted the magnetic wires and hence enabled the bending of the magnetized posts. Such bending led to a post displacement ranging from 100 nm to $1\,\mu$m. For a cell positioned at the top of a magnetic post, this displacement transferred a punctual force to the cell. The magnitude of this force was a function of the post as well as the nanowire dimensions, in accordance with the following equation

$$F_{P_{mag}} = \frac{3\,\mu_\perp\,B\,(L_{mp} + L_w)}{2(L_{mp}^2 + L_w\,L_{mp} + L_w^2)} \tag{1.6}$$

where L_{mp} and L_w are the lengths of the post and the length of the embedded nanowire respectively, and $\mu_\perp$ is the component of the dipole moment perpendicular to the magnetic field B, as represented in the inset c) of Fig. 1.7. For a nanowire $5\,\mu$m long, a maximum force of 27 nN was reported by the authors.

1.2.2.5 Electric fields

Non-uniform electric fields can physically deform an isolated cell [59, 60, 61, 62, 63]. Indeed, when a cell is subjected to an electric field, a dipole can be induced due to interfacial polarization on the cell membrane. Depending on the electric field strength and the effective polarization of the cell, stress can then occur at the interfaces and result in a deforming force. During minor deformation, the elastic strain of the cell along the

electric field direction is estimated as [64]

$$\frac{\Delta L_c}{L_{c_0}} = K_s \, J^2 \, \Re\left[C(\omega)\right] \qquad (1.7)$$

where ΔL_c represents the deformation of the cell, L_{c_0} is the original length of the cell, K_s is a constant representing the elastic properties of the cell, ω is the angular frequency of the AC electric field applied, and $\Re\left[C(\omega)\right]$ is the real part of the complex Clausius-Mossotti factor. The latter depends on the internal structure of the cell and is cell-type specific.
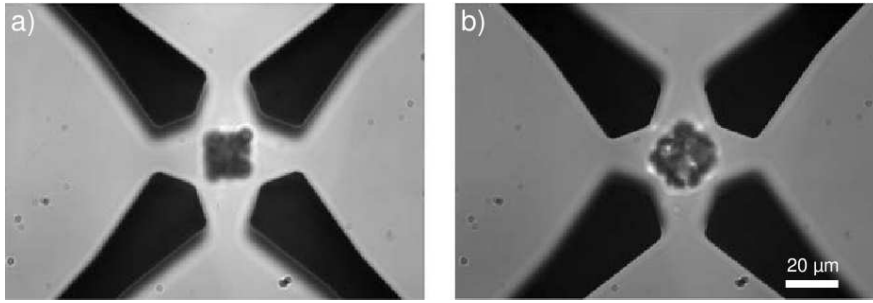
Figure 1.8: a) A GUV trapped between the electrodes of a microfield cage. b) The GUV is deformed by electric field. Images adapted from [65].

Electrodes capable of generating such electric fields can be patterned with microfabrication processes [66, 67]. For example, MEMS electrodes that were used to capture, hold, rotate and deform isolated giant unilamellar vesicles (GUVs) are shown in Fig. 1.8 [65]. Modulation of the amplitude and frequency of the voltage applied to the electrode edges permitted the authors to conduct stretch and relax experiments on isolated GUVs, whose size ranged from 5 to 25 μm.

Electric fields have also been associated with microchannels to provoke cell electroporation. In [68], electric field intensity was concentrated toward the narrow section of a microchannel (see Fig. 1.9). During experiments, field intensities of 200 V/cm, 400 V/cm as well as 600 V/cm were applied. Stress indirectly arose from the electroporation phenomenon. In effect, cells may open up pores when they experience an external electric field with an intensity beyond a certain threshold. Material exchange across the membrane may then occur. A direct consequence was the swelling of human breast epithelial cells while they were flowing through the microchannel. Even though the amount of stress induced was not explicitly quantified by the authors, such method allowed to strain suspension cells at stimulation rates as high as 5 cells/s.

1.2.2.6 Optical gradients

Both refraction and reflection of light exert forces on all objects. If these forces are negligible in the macroworld, they become significant for microscopic objects weighing
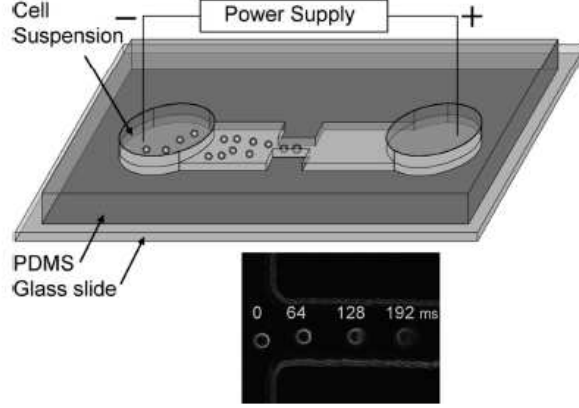
Figure 1.9: Top: electric fields used in conjunction with microfluidic channel to provoke cell electroporation. Inset: swelling evolution at different times for a cell experiencing electroporation while progressing through a microchannel [68].

less than $1\,\mu$g. Thereby, light has been used to manipulate microparticles for four decades [69]. Two optical fibers can be used to guide the light emanating from a laser source and create a dual beam laser trap system [70, 71, 72, 73, 74, 75]. In [76, 77], Guck et al. made use of optical fibers with a diameter of $125\,\mu$m to trap and stretch biological entities. The divergent laser beams were directed at diametrically opposite portions of a suspension cell placed between them, as shown in Fig. 1.10. Often termed as optical stretcher (OS) in the literature, the net stretching force F_{os} exerted by such a configuration on a single cell can be expressed by the following equation [27]

$$
\begin{aligned}
F_{os} = {} & \left(n_m - (1 - R_{rl})\, n_c + R_{rl}.n_m \right) \left(\frac{P_l}{c_l} \right) + \\
& \left(n_c - (1 - R_{rl})\, n_m + R_{rl}.n_c \right) \left((1 - R_{rl}) \frac{P_l}{c_l} \right)
\end{aligned}
\tag{1.8}
$$

where n_m and n_c are the refractive indices of the surrounding media and cell, respectively, R_{rl} is the fraction of reflected light, c_l is the speed of light in vacuum, and P_l is the total light power.

With a 500 mW power laser source, this approach allowed Guck and co-workers to generate uniaxial stretching forces up to 400 pN in aqueous media. This facilitated cell elongations between 7-30 μm. Guck et al. even predicted that given a higher power laser, the maximum stretching force could achieve or exceed 1 nN.

1.2.2.7 Fluid flows

Fluid flows permit to mimic in a simple manner a variety of stresses that vascular cells naturally undergo in the vessel architecture of the arterial system. At the macroscale, experimental apparatus such as cone-and-plate rotating chambers [79] or parallel-plate
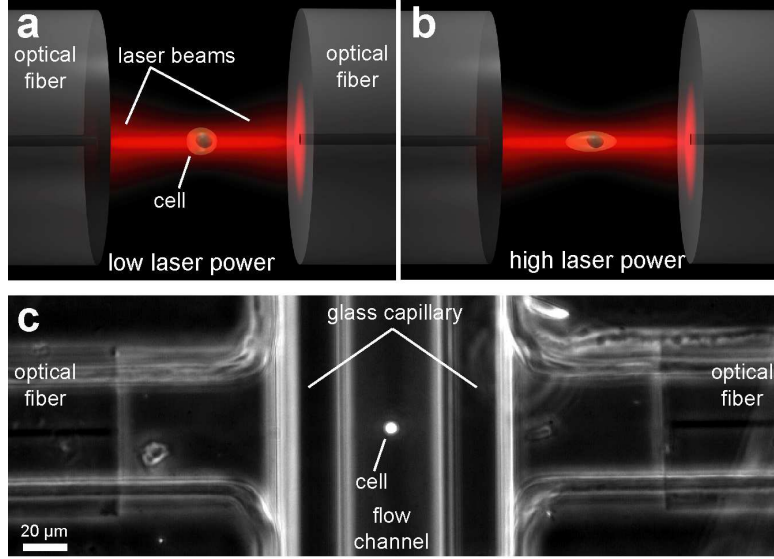
Figure 1.10: Principle of an all-fiber OS. (a) At low laser power, the OS can trap a RBC (∼10 μm in diameter). (b) At higher laser power, the OS can stretch the RBC. (c) The OS associated with a fluidic microchannel ensuring the delivery of cells. Images from [78].

flow channels [80] are conventional tools to impose hydrodynamic shear-stress on large cell cultures. With advances in microfabrication technologies, MEMS parallel-plate channels (see Fig. 1.11) have been reported [81, 82, 83]. In [84], the authors integrated four parallel-plate channels of different cross-sections on a single miniature fluidic chip. Channel height was $25\,\mu m$ whereas channel width ranged from $250\,\mu m$ to $1000\,\mu m$. Such small dimensions guaranteed a low Reynolds number ($Re \leq 1.0$), ensuring a laminar flow with no turbulence within the microchannels. For a parallel-plate channel with an infinite aspect ratio, the generated wall shear stress can be expressed as

$$\tau_w = \left(\frac{6\,\eta}{h_{mc}^2\,b_{mc}} \right) \nu \qquad (1.9)$$

where η denotes the fluid viscosity, h_{mc} and b_{mc} are the height and the width of the chamber, respectively, and ν is the volumetric flow rate. By varying the width of the channels, Lu et al. could expose a culture of fibroblasts to multiple shear stress conditions. During experiments, shear stresses up to 4000 dyne/cm^2 were generated by the authors. It is also worth noticing that if microchannels incorporate areas with narrower sections, fluid flows can also be used to deform suspension cells by forcing them to travel through the constricted areas [86].
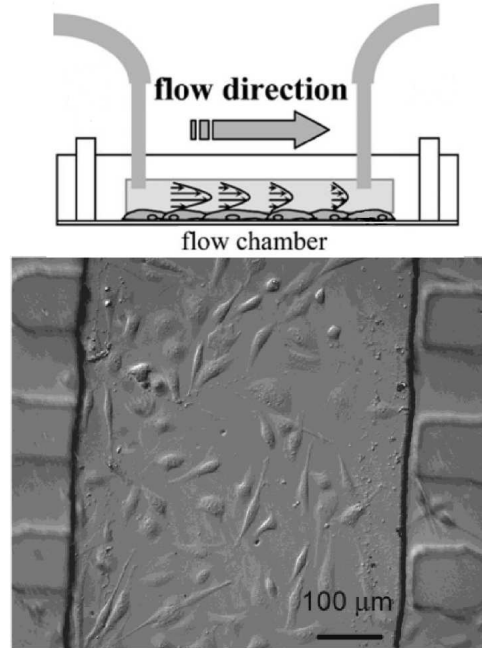
Figure 1.11: Top: sketch representing the principle of a microfluidic channel imposing shear stress to a culture of adherent cells [85]. Bottom: microscope view of fibroblasts cultured in one of a parallel-plate flow chambers. Average fibroblast diameter was about $20\,\mu$m after attachment [84].

1.2.3 MEMS providing sensing capabilities

Applying a stress or a strain to a cell is a requirement for many studies. But once the cell has been mechanically stimulated, the possibility to evaluate the mechanical behavior of the cell is also often a *sine qua non* condition. In the following paragraphs, one hence enumerates different MEMS capable of extracting various mechanical properties of cells.

1.2.3.1 Deformable beam-based sensors

Cells can migrate in response to multiple situations (e.g., wound healing). During locomotion, cells pull themselves and develop forces to move from one location to another. In precursory works, soft silicon substrates that wrinkled during cell movements constituted a first mean to detect these forces [87, 88, 89]. Distortions of the substrates were however highly chaotic and nonlinear. A quantitative evaluation of the cell forces generated was hence difficult.

To alleviate this difficulty, locomotion forces developed during cell migration were studied with cantilever-like configurations. For instance, Galbraith and Sheetz [90] reported a high functional density MEMS made up of 5904 horizontal microlevers (see Fig. 1.12). Each lever was ended by a pad. The area of the pads ranged from 4 to

25
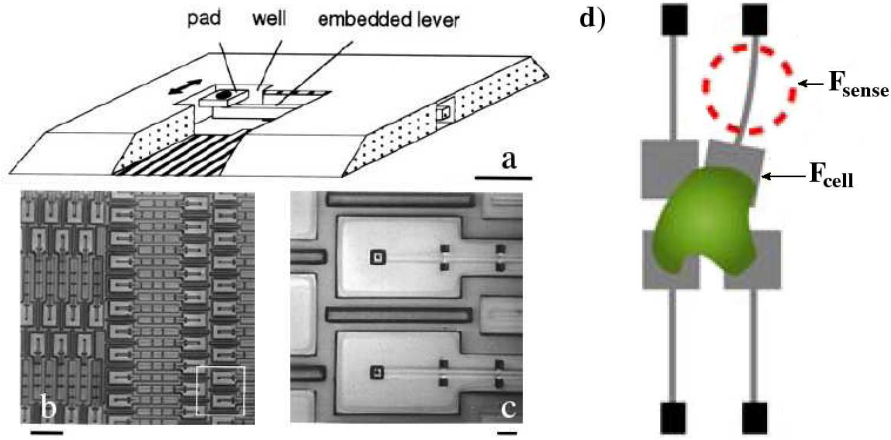
Figure 1.12: Left: different magnifications of the micromachined substrate designed by Galbraith et al: (a) is a cut-away drawing that shows a lever, a pad and a well (bar = 10 μm); (b) shows 0.18 mm long levers (bar = 1 mm); (c) corresponds to the white square area visible in (b) (bar = 10 μm). Right: (d) Sketch representating the device viewed from above: cell forces are evaluated thanks to lever deflections. Images adapted from [90, 32].

25 μm^2. The whole set of pads constituted a sensitive surface where a chicken fibroblast was seeded. Centroid of the pads were monitored optically during locomotion of the cell. The forces that the cell exerted on the pads could be determined by calculating the product of the pad displacement and the stiffness of the levers (see image (d) in Fig. 1.12). Traction forces < 1 nN and up to 100 nN were measured for different regions of the cell.
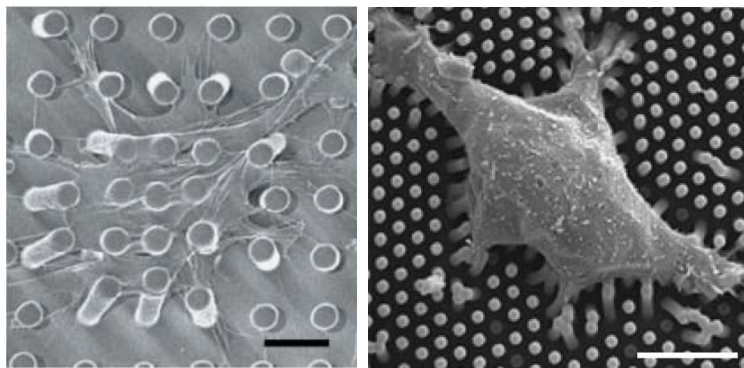
Figure 1.13: Examples of a micropost array detectors for the mapping of cell traction forces. Local forces can be estimated with Eq. (1.10). Black and white scale bars indicate 10 μm and 8 μm, respectively. Images adapted from [91, 92].

A restriction usually admitted for the MEMS of Galbraith and Sheetz is that the levers could solely bend in one direction. Hence, forces generated in other directions than the free axis could not be measured with this system. Furthermore, the spatial resolution was still limited. To circumvent these limitations, isolated cells have also been placed on the top of MEMS arrays of compliant microposts (see Fig. 1.13). In references consulted by the author [91, 92, 93, 94] (see also reviews [95, 96]), posts dimensions typically spanned 3-50 μm in length with a diameter 2-10 μm. Posts were also closely spaced with a typical pitch of 2-10 μm. Such tight post spacing allowed subcellular spatial resolution. It also helped to avoid spreading of the cells between posts. Posts could deflect independently in response to local tractions. Again, the post deflection Δ_{mp} imposed by the cells was typically measured by optical microscopy and then related to the force F_{mp} via the standard linear elastic beam theory

$$F_{mp} = \frac{3\,E_{mp}\,I_{mp}}{L_{mp}^3}\,\Delta_{mp} \tag{1.10}$$

where E_{mp}, I_{mp} and L_{mp} are the time-independent elastic modulus, the moment of inertia and the length of the post, respectively. The stiffness of the posts typically ranged from 0.47 to 1600 nN/μm. Knowing the value of the stiffness, image analysis of each post yielded an independent force vector. Combined, these force vectors formed a map of subcellular traction forces.

With microposts arrays, cell forces as low as as 1 nN were measured [92]. It is also worth pointing out the versatility and reversibility of these configurations. Section 1.2.2.4 has indeed mentioned the possibility to actuate such microposts with an external magnetic field. Microposts have hence the potential to serve alternatively as discrete actuators or sensors.

1.2.3.2 Piezoresistive strain gauges

In the literature, numerous devices intended for sensing cell forces are compliant structures that deform when interacting with the cells [97, 98, 99, 100, 101, 102, 103, 104, 105]. As in the previous section, if the stiffness of the structure is known, visual observations of structure deflections permit to calculate forces. However, for such visual observations, a microscope, a video camera and an image analysis software are required. Although a microscope remains an important tool to observe cell during manipulations, this configuration is not in favor of the functional density.

As an alternative, piezoresistive (PZR) strain gauges permit to evaluate structure deflections without optical means. PZR strain gauges can be easily deposited and patterned on microfabricated structures. By way of illustration, PZR gauges were implemented at the base of 16 AFM cantilevers embedded within a single frame [106]. Compared to a conventional AFM setup, the functional density was significantly improved. In effect, PZR gauges permitted to suppress the need of laser beams and photodiodes. This also allowed to circumvent misalignment difficulties. Although no experiment was
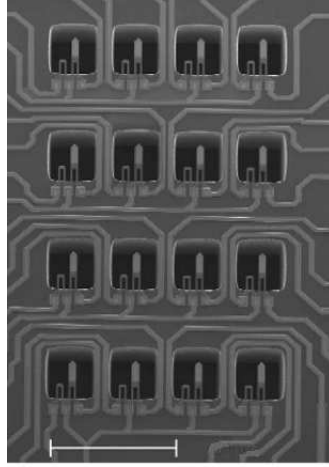
Figure 1.14: 4x4 matrix of tipless cantilevers integrating PZR gauges as reported in [106]. Unlike conventional AFM setups, lasers and photodiodes are not needed anymore. This facilitates the integration of many AFM in parallel. Scale bar is 500 μm.

directly validated on cells, this array was however able to work in liquid environments.
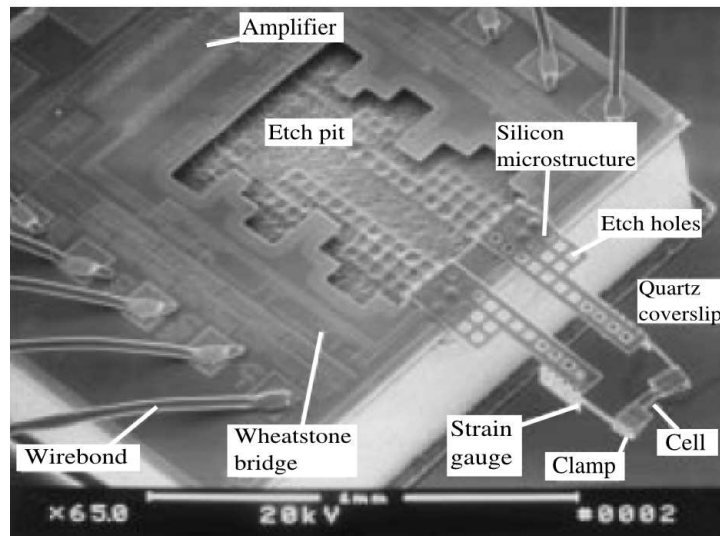
Figure 1.15: Heart cell force transducer proposed by Lin et al.: contractile force generated by a cardiac myocyte are evaluated via PZR strain gauges [107].

PZR strain gauges were also incorporated in the MEMS force transducer of Lin et al. [107]. This force transducer was designed to measure contraction forces of living heart muscle cells. The volume of this MEMS force transducer system was <1 mm^3. It was composed of two free-standing polysilicon clamps. The clamps permitted to hold

the ends of a heart cell under investigation. As shown in Fig. 1.15, each clamp was suspended by a beam. PZR strain gauges were implemented at the base of the beams. PZR gauges were connected to a Wheatstone bridge and amplification electronics for electrical readout. Cell contractions then provoked the bending of the beams, and the force generated by a cardiac cell could be evaluated by measuring the output voltage of the bridge. Theoretically, this MEMS could provide a sensitivity of 2.6 mV/μm. In experimental conditions, the authors could measure forces spanning from 100 nN to 50 μN, and an average contraction force of $\sim$12 μN was quantified for several rat cardiac myocytes.

1.2.3.3 Capacitive sensors

Measure of capacitance changes can also resolve applied displacements/forces without the need of an optical equipment. A typical example of capacitive sensors is illustrated in Fig. 1.16. A displacement Δ_{dc} applied to the probe tip caused the inner structure to move, changing the gap between each pair of interdigitated comb capacitors. In particular, the sensor in Fig. 1.16 used a differential tri-plate configuration which permitted to obtain a linear relationship between the displacement applied and resulting capacitance changes [108]. When an AC signal U_s was supplied to the outer capacitors, capacitance changes could be converted into voltages. Thereby, Δ_{dc} could be linearly related to voltage changes

$$\Delta_{dc} = d_0 \frac{U_{out}}{U_s} \tag{1.11}$$

where d_0 is a constant representing the nominal position of the comb structure (i.e., no force applied, capacitor plates equally spaced) and U_{out} is a measured voltage.

Two springs of given stiffness then allowed to convert the displacement estimated into a force. The springs being modelled as two fixed beams with a load point applied in the middle, the force-deflection relationship could be determined from

$$F_{capa} = \Delta_{dc} \frac{4\,E_{si}\,b_{sc}^3\,h_{sc}}{L_{sc}^3} \tag{1.12}$$

where F_{capa} is the resolved force applied upon the probe, E_{si} is the average Young's modulus of P-type silicon, and L_{sc}, b_{sc} and h_{sc} are the spring length, width, and thickness respectively.

It is interesting to note that capacitive configurations are capable of providing force information along multiple axes (e.g., [110]). In [109], interdigitated capacitors were orthogonally configured to make the force sensor capable of resolving in-plane forces not only along the x direction (as shown in Fig. 1.16) but also along the y direction. The sensor was then used to measure puncturing forces on embryos and oocytes. In particular, the sensor was capable of resolving forces up to 25 μN in x and 110 μN in y
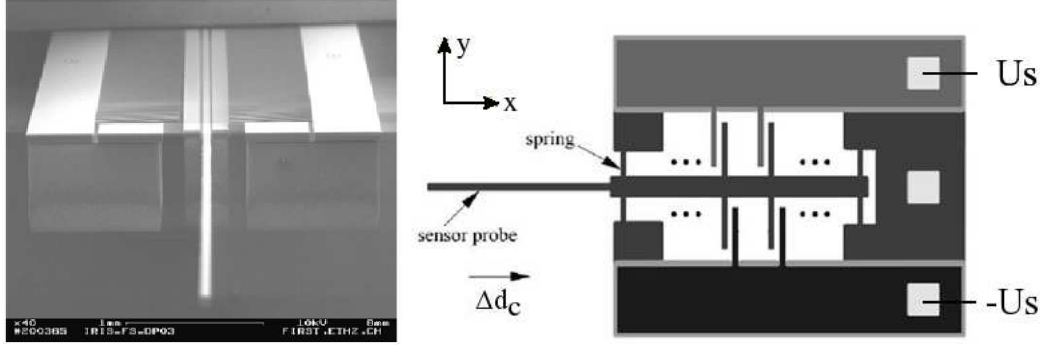
Figure 1.16: Uniaxial capacitive force sensor. This MEMS can solely sense forces along the x direction (images adapted from [108]). Evolution of the concept with capabilities for resolving forces in the x and y directions simultaneously has been reported in [109].

with a resolution of 0.01 μN in x and 0.24 μN in y.

It is also worth highlighting that configurations based on interdigitated fingers can efficiently combine electrostatic actuators and sensing parallel-plate capacitors in a compact unit. For instance, MEMS grippers that can simultaneously apply and measure forces on cells have been reported in [111, 112].

1.3 Discussions

Although the survey of the previous sections does not pretend to be exhaustive, it provides a sufficiently representative sample of MEMS to discuss the current trends and remaining challenges that must be addressed in the field of cell mechanics.

1.3.1 Nature and number of cells targeted

MEMS dedicated to the mechanical investigation of individual living cells must cope with several harsh constraints. A first problem is directly related to the nature of the cells to be tested. Indeed, living cells come in a wide variety of shapes and sizes because they all perform different functions. As a reminder, two distinct types of cells are encountered in cell studies:

- As seen in Table 1.1, adherent cells (e.g., fibroblasts, endothelial cells) need to anchor to an underlying substrate (see for instance Fig. 1.13). Adherent cells typically measure a few micrometers and have a highly irregular shape. To a first approximation, adherent cells such as endothelial cells behave more as solids.

- Suspension cells have almost a spherical shape and do not attach to a surface. Blood cells, oocytes or embryos are examples of suspension cells. The latter are however significantly bigger than the former and the size of suspension cells can

span a wide range of values. For instance, RBCs (see Fig. 1.10) typically have a diameter of 8-12 μm, whereas oocytes and embryos have a diameter that usually ranges from $\sim$100 μm to 600 μm. Compared to adherent cells, suspension cells usually behave more as liquid droplets surrounded by an elastic cortical shell.

Adherent and suspension cells hence exhibit morphologies and properties that are fundamentally different. These differences pose very different challenges for stimulating cells and measure their reactions. Accordingly, many MEMS reported in previous sections lack versatility in the sense that they can deal exclusively with a single type of cells. By way of illustration, the MEMS cell puller of Scuor et al illustrated in Fig. 1.2 does not lend itself to the stretching of suspension cells. Conversely, the OS of Guck et al. depicted in Fig. 1.10 only proved to be suitable with suspension cells showing a high degree of symmetry and/or a uniform optical density.

In addition, it is important to realize that for most MEMS cited, delicate and time-consuming protocols are often required to properly prepare and place the cells prior to experiments. For instance, in [57, 58, 97, 98, 103], the authors functionalized the probe extremities to guarantee a firm attachment of the cells under tests. In [34, 35], the authors used small drops of epoxy to attach a fibril between the two pads of their uniaxial cell tenser. Long curing times were necessary and it could take hours to conduct experiments with just a few cells.

In the mean time, it has been experimentally confirmed that cell responses are largely heterogeneous from cell to cell, even within a given cell line. A more representative overview of the cellular behavior could be obtained by considering the averaged responses of many individual cells studied independently. A new tendency based on statistical studies has hence progressively emerged (see for instance [113, 114]).

Today, MEMS with the capability to provide cell measures obtained in a short amount of time are hence highly requested by the science community. To speed up cell analysis, matrix of MEMS replicated in arrays (e.g., see Fig. 1.14) have been reported for the simultaneous analysis of several cells in parallel. Usually, the number of MEMS contained within a singly frame do not exceed 10-20. This is due to the fact that the replication of a higher number of perfectly identical MEMS may rapidly become challenging. Moreover, if patterns duplicated are deformable structures that must be optically monitored (e.g., [115, 116]), the larger field of view necessary leads to a loss of resolution. Besides, the requirement for optical observation may prevent rapid analysis and is today considered as a significant barrier to parallelization in most experiments [117].

As an alternative to alleviate these difficulties, serial approaches where individual cells are successively driven toward excitation/analysis areas have been proposed (e.g., see Fig. 1.10). Interesting results have been reported with the possibility to stimulate and analyze cell mechanical responses at rates as high as 5 cells/sec [68]. However,

MEMS exploiting this approach are always coupled to fluidic microchannels where fluid flows ensure the repetitive delivery of the cells toward excitation/analysis areas. Unfortunately, a lack of versatility is again observed since this principle works only with restrictive types of suspension cells and excludes adherent cells.

1.3.2 Constraints imposed by the cell environment

Living cells are obviously entities of exquisite fragility. For successful mechanical studies conducted on cells, a first priority is to preserve their integrity so that they can survive after experiments. Ideally, cells should be conserved in specific medium during experiments. Such cell medium allow the continuous delivery of vital nutrients in order to maintain cells alive.

But major challenges arise as soon as MEMS must face such a liquid environment. For instance, in the presence of aqueous solutions, capillary meniscus arise at the air-water interface when soft force sensors (e.g., [97, 98, 103]) are immersed and removed. Soft structures must then withstand large capillary forces. Besides, capillary forces can engender measurement artifacts.

MEMS exploiting electrostatic comb drives (see Fig. 1.2) experience significantly reduced performances when immersed in cell medium. Due to the hydrophobic nature of the silicon-water interface, air trapping between the comb drive teeth and the MEMS ground plane may arise. Furthermore, the enhanced electrical conductivity of liquids usually reduces their initial stroke.

Similarly, electrothermal beams cope with challenging phenomena if they are plunged in a liquid environment. For instance, electrothermal beams cannot be supplied with continuous power for underwater operation due to *electrolysis*. For the MEMS shown in Fig. 1.4, alternating voltages were used in electrolytic solutions. But the initial travel range of $9\,\mu$m measured in air was restricted to $4\,\mu$m in liquids. An additional feature of electrothermal actuators relates to the high temperature that they can reach during operation. Since cells are particularly sensitive to temperature fluctuations, high temperatures may potentially cause irreversible damages. Special precautions should hence be taken accordingly.

The latter remark may be extended to all types of contact-based MEMS, that is to say all MEMS for whom an extremity directly touches the cells. For instance, sharp tips (e.g., such of those used in conventional AFM) may cause damages to external lipid cell biomembranes. Moreover, contamination problems may arise once the tool has touched a cell. Therefore, the tips should be properly cleaned before each new experiment. This additional laborious step may further prevent repetitive analysis.

MEMS that exploit non-contact based techniques may alleviate such problems. Optical gradients, electric fields and magnetic fields have indeed the potential to carry

out cell stimulation without direct physical interaction with the cells. However, electric fields can directly affect cells under test [118]. Although no direct contact occurs during cell stimulation (see Fig. 1.8), electric fields cause power dissipation in the form of Joules heating in a conductive medium. Therefore, and as in the case of electrothermal actuators, the usage of electric fields requires to monitor changes in temperature that can affect cell phenotypes.

The wavelength of some highly concentrated laser beams may also be hazardous for cells [119, 120, 121, 122]. Comparatively, magnetic fields (see Fig. 1.6) are nowadays considered safe for cells. In effect, magnetic fields do not significantly disturb the cell response upon short times of exposure. Unfortunately, restrictions of magnetic setups are related the microbeads that must be locally attached to the cell membrane. Magnetic forces applied strongly depend on the beads size whereas it may be difficult to avoid size variations from bead to bead in experimental conditions. Likewise, material properties of the beads used (e.g., magnetic moment) cannot be easily controlled. Moreover, the adhesion procedure of the beads remains an unpredictable process and formation of bead aggregates may appear. Finally, since bead immersion is unpredictable, the force distribution around adhesion sites can actually be highly heterogeneous.

Taking into account the above discussion, it is clear that using MEMS in cell media remains challenging. Besides, several results of cell mechanical studies reported in the literature have been obtained in air. However, living cells naturally evolve in a liquid environment and conducting experiments with cells in a dry environment may significantly impact their mechanical properties. Therefore, it may be reasonably presume that results obtained in air could have been partly biased and could have possibly led to some misinterpretations.

1.3.3 Type of mechanical properties probed: relevance of the cell elastic modulus

MEMS reported in Section 1.2 have permitted to investigate different biophysical properties of cells. Examples of these biophysical properties are summarized in Table 1.2. In essence, all these properties permit to gain insights in the mechanics of cells. Accordingly, they all deserved to be thoroughly investigated.

Nevertheless, the notion of cell deformability appears today as an increasingly important physical marker for future biomedical applications. Cell are indeed constantly stabilized by their internal scaffolding, the cytoskeleton network. As seen in Section 1.1, the cytoskeleton is a complex biopolymer network that may undergo structural alterations leading to changes in cell rigidity. Deformation characteristics of cells may hence provide relevant information about the biological and structural function of cells.

The notion of cell deformability is however general and must be clarified. Basically, studying cell deformability requires application of an external force, and a correspond-

Cell Biophysical Properties	Examples of MEMS
Traction forces	Post arrays [91, 92]
Contraction forces	Force transducer [123]
	Post arrays [124, 125]
Adhesion forces	Cell tenser [101, 105]
Deformability	Capacitive sensors [109]
	Optical stretcher [74]
	Electrical fields [67]

Table 1.2: Typical cell mechanical parameters investigated with MEMS

ing quantification of the cellular deformation in response. Intuitively, a stiffer cell is less deformable. In the literature, quantitative measures of cell deformability are however reported in different manners. Cell deformability can indeed be expressed in terms of elasticity (i.e., elastic modulus), viscoelasticity or stiffness. Although all of these parameters provide information about the resistance of a cell to deformation, they describe distinctly different properties. For the sake of clarity, some essential distinctions between these parameters are first reminded.

A cell exhibits an elastic behavior if it deforms under stress (i.e., an external force) and returns to its orginal shape when the stress is removed (see left image in Fig. 1.17). The relationship between stress and strain (force-deformation) is linear, and the deformation energy is returned completely. Elasticity is often referred to as the elastic modulus or Young's modulus. Given the large values typical for many common materials, the Young's modulus is usually quoted in MPa or GPa. For instance, the Young's modulus of steel, bone, polystyrene or soft silicon rubber are about 200 GPa, 17 GPa, 3MPa and 2 MPa, respectively. Comparatively, most living cells range from 1 kPa to 100 kPa (see Fig. 1.18).

A cell behaves as a viscoelastic material if it exhibits both viscous and elastic characteristics when undergoing deformation. Viscosity is a measure of the resitstance of a fluid to being deformed by either shear stress or extensional stress. The reciprocal of viscosity is fluidity. The relationship between stress (force) and strain (deformation) is non linear for viscoelastic materials, and the deformation energy is not returned completely. The amount of energy loss is represented by the hysteresis of a loading and unloading cycle (hysteresis in the force deformation curve, see right image in Fig. 1.17).

Stiffness relates to the resistance of a solid body. Stiffness is not the same as the elastic modulus. Stiffness is a property of a solid body; elastic modulus is a property of the constituent material. The elastic modulus is an intensive property (it does not depend on the size, shape, amount of material and boundary conditions) of the solid
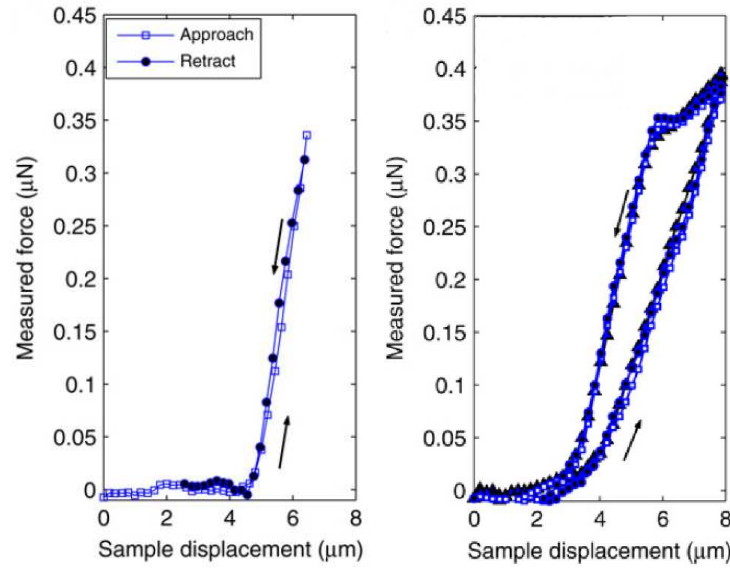
Figure 1.17: Left: typical force-deformation curve for an elastic rigid material. Right: typical force-deformation curve for a viscoelastic material (epithelial cell): the hysteresis cyle is representative of a loss of energy. Images adapted from [18].
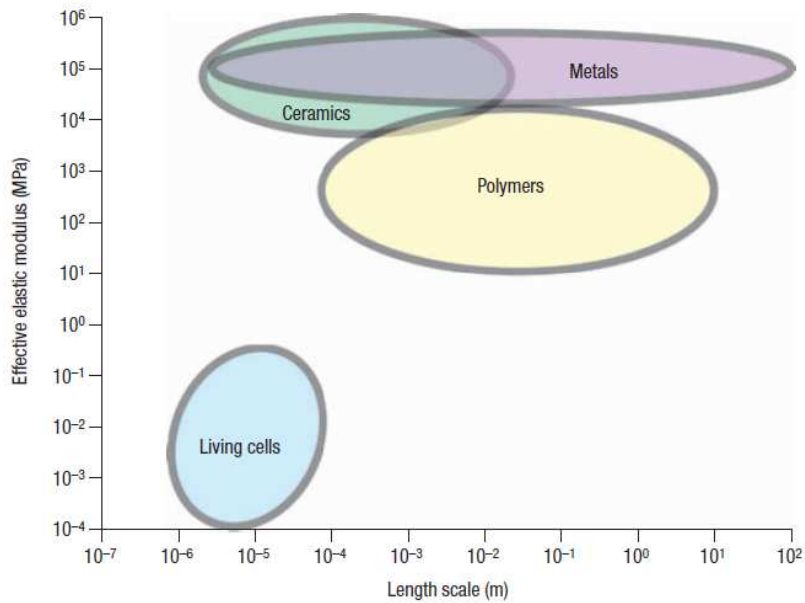
Figure 1.18: Approximate range of values for the elastic modulus of biological cells and comparisons with those of engineering metals, ceramics and polymers. Image from [3].

body. For example, a solid rock and a soft flat spring made from the same material (e.g., steel) have the same elastic modulus but a different stiffness.

In this dissertation, one will focus on measuring the Young's modulus of living cells. Scientific evidences have indeed revealed connections between alterations in the elastic modulus of single cells and pathophysiological states [16, 126, 127, 128, 129, 130, 131, 132]. As observed in Table 1.3, a dramatically reduced Young's modulus is for instance a characteristic feature of cancerous cells. The standard deviation of cancerous cell is also over five times narrower than benign cells. By contrast, RBCs infected by sickle cell disease (SCD[1]) have a Young's modulus approximately three times higher than in normal cells as well as a larger standard deviation.

Cell type	Human disease	Young's modulus (kPa)		Measurement system	Reference
		Healthy cells	Abnormal cells		
Epithelial cells	Cancer	8.6 ± 3.6	0.7 ± 0.4	AFM	[126]
Mesothelial cells	Cancer	1.97 ± 0.7	0.53 ± 0.1	AFM	[129]
Mesothelial cells	Cancer	2.53 ± 1.23	0.41 ± 0.18	AFM	[130]
RBCs Erythrocytes	SCD	1.1 ± 0.4	3.05 ± 1.09	AFM	[131]
RBCs Erythrocytes	SCD	1 ± 1.1	3 ± 2.7	AFM	[132]

Table 1.3: Mean values and standard deviations of elastic modulus for human cells affected by cancer or sickle cell disease (SCD) compared to normal cells.

Accordingly, the elastic modulus of cells appears as a meaningful marker to differentiate pathogenic cells and healthy cells. For diagnostic purposes, knowing the Young's modulus of cells may hence help to detect the presence of cancer as well as other cell-based degenerative diseases at earlier stages. Furthermore, elasticity measurements also have the potential to disclose the specific effects of pharmaceuticals at the cellular level [133, 134, 135]. Therefore, cell elasticity measurements may also prove advantageous in drug development.

Although several MEMS have been specifically devised for measuring the Young's modulus of living cells (e.g., [109]), AFM remains the most widespread tool. Thereby, all results published in Table 1.3 as well as in [16, 127, 128, 130] were derived force-deformation information measured with an AFM cantilever. Then, a model based on the Hertz theory permitted to extract the Young's modulus

$$F_c = \frac{4}{3} E^* \delta_c^{3/2} \left(\frac{R_1 R_2}{R_1 + R_2} \right)^{1/2} . \tag{1.13}$$

In Eq. 1.13, F_c and δ_c are the force and the amount of deformation applied to the cell, R_1 is radius of curvature of the cell, R_2 is the radius of curvature of the probe applying

---

[1]SCD is an inherited blood disorder. It gives rise to circulation problems due to the fact that stiffer RBCs have difficulty flowing through the small blood vessels and capillaries in the body. Some serious consequences of SCD include stroke, infection and pneumonia (see [8] for further explanations).

the deformation, and E^* is the effective Young' s modulus

$$\frac{1}{E^*} = \frac{1 - \nu_1^2}{E_1} + \frac{1 - \nu_2^2}{E_2} \tag{1.14}$$

where ν_1 and E_1 are the Poisson's ratio and Young's modulus of the cell whereas ν_2 and E_2 are the Poisson's ratio and Young's modulus of the probe.

Notwithstanding indisputable advantages to conduct cell investigations, AFM is more adapted to conduct experiments on adherent cells. Round suspension cells cannot be easily studied with AFM. Moreover, it is recognized that the throughput of AFM is severly limited. This is a major bottleneck for using the Young's modulus of cells as a reliable indicator. As discussed in Section 1.3.1, cells are indeed highly heterogeneous entities and large differences can occur during measurements, even among a particular cell line. For enabling the reliable use of the Young's modulus for diagnosis purposes, measurements must be conducted on a significant number of cells in order to obtain a statistically set of meaningful data [136].

To bridge this gap, several research teams have paved the way with MEMS intended for parallelization and automation [63, 67, 68, 137]. Interesting results have been reported. Unfortunately, to date, MEMS reported were only proven to be suitable for cells showing a high degree of symmetry and/or cells showing restrictive properties (e.g., uniform optical density).

1.4   Summary and conclusions

This first chapter has reviewed a large panel of MEMS intended for cell mechanics. MEMS encompassing actuation capabilities for cell stimulation and MEMS providing mesurement means to monitor mechanical cell responses have been surveyed separately. MEMS combining actuation and sensing capabilities have also been highlighted. Several discussions have also been provided with the aim to realize the specific constraints that apply in the context of cell analysis. In light of these discussions, it can be concluded that:

- To survive, cells must be maintained in a culture medium providing vital nutrients. Therefore, cell mechanical studies require MEMS that can cope with a liquid environment.

- MEMS capable of extracting values of cell Young's modulus turns out to be of increasing interest and show great promise for future biomedical applications. The Young's modulus of diseased cells indeed vary from their healthy counterparts. Thereby, it is presently recognized that Young's modulus values may be correlated to disease states. In the future, Young's modulus values might be used to diagnose pathological conditions at earlier stages. To quantify the Young's modulus of cells,

MEMS must be somehow capable of measuring the force applied to a cell and the corresponding cell deformation in response.

- To be used as a robust and reliable indicator for diagnosis, an averaged value of the Young's modulus must be obtained by probing numerous cells. MEMS capable of providing values of elastic modulus within minutes are highly requested by the research community. The problem is that adherent and suspension cells exhibit very different morphologies and properties that pose antagonist challenges. Although several solutions based on parallel or serial approaches have been proposed, no MEMS capable of measuring the Young's modulus of both adherent and suspended cell with high throughput capabilities has been reported so far.

To bring new solutions to the above mentioned problems, this thesis will present a planar structure where two beam resonators are exploited to extract the Young's modulus of cells. In effect, compared to a static mode, oscillating beams that exploit resonance phenomena allow for a higher dynamic range and a higher transduction sensitivity. For instance, resonance operation is usually favoured for cantilevers aimed at detecting the presence of target biomolecules. This preference can be justified by the fact that, in a static mode, a minimum amount of target molecules must bind to the cantilever surface (which is coated with specific receptors) in order to generate enough surface stress and cause the cantilever to deflect. By way of comparison, single molecule detection capabilites with exquisite mass resolution down to the attogram (10^{-18}g) and even to the zeptogram (10^{-21}g) have been achieved with dynamic modes [138, 139].

To extract the Young's modulus of cells, beam resonators can also be used to measure forces with improved sensitivity. Beyond enhanced sensitivity, beams operating in the frequency domain also permit to circumvent some typical limitations encountered for devices operating in static modes. Generally speaking, common readout schemes used to measure the static deflection of compliant structures involve analog signals that are amplitude dependent (e.g., voltages). Such signals are intrinsically sensitive to noise sources, especially at the MEMS scale. By contrast, the frequency domain output is digital in the sense that it is independent of analog level. Resonant structures hence provide inherent accuracy and easy digital interfacing (e.g., connection to a frequency counter). This further minimizes susceptibility to interferences and degradation of transmitted signals.

In spite of such potential advantages, beam resonators are rarely employed for determining the Young's modulus of living cells. This is mainly due to the fact that conventional beam resonators cannot be easily exploited when dealing with cells cultured in growth medium. This is demonstrated in the next chapter where the effects related to the presence of a surrounding fluid on a simple clamped-clamped beam are theoretically investigated. As a solution to alleviate these effects, as well as to bring new solutions to the above mentioned problems, the new resonant structure proposed in this dissertation will be introduced in Chapter 3.

Chapter 2

Sensing forces in cell studies with beam resonators: theoretical background

Chapter 1 has revealed why measuring the elastic properties (i.e., the Young's modulus) of living cells is of increasing importance. To determine its Young's modulus, the cell must be deformed with a known force. In a first step, this chapter does not address how to deform the cell. Instead, it focuses on how the force applied to the cell can be measured with a simple beam resonator. As mentioned in the conclusion of Chapter 1, the use of an oscillating beam can bring multiple benefits. Ideally, it can achieve a higher force sensitivity than conventional force sensors operating in a static mode. In addition, a beam operating in a dynamic mode can provide a higher immunity to noise sources.

To grasp fundamental concepts and gain insights into how forces can be measured with a beam resonator, Section 2.1 considers a case of study where a suspension cell applies an axial force to one extremity of a beam clamped at both ends (clamped-clamped beam). Based on Euler-Bernouilli beam theory, an exact solution predicting the dynamic behavior of the clamped-clamped (CC) beam subjected to the axial force is first derived. Because energy methods will be used in Chapter 3, Section 2.2 demonstrates that an easier energy method provides similar results and can be safely used to describe the dynamics of an oscillating beam. Energy techniques are then employed to consider a harsh constraint related to cell studies, namely the fact that studies must be conducted in liquids. In particular, Section 2.3 shows that the initial performances of the CC beam are severely altered if it is surrounded by a liquid. In Section 2.4, a parametric analysis demonstrates that problems faced by the CC beam in liquids cannot be easily minimized solely by changing the beam geometry. Finally, Section 2.5 summarizes different points highlighted in the course of the chapter and makes the transition towards Chapter 3.

2.1 Vibration of a CC beam subjected to an axial force: exact solution

The case of study considered is illustrated in Fig. 2.1. A salmon fish egg cell with a diameter of approximately 5 mm [140] enters in contact with one extremity of a CC beam. The egg cell is then compressed and an axial force N is applied to the beam. For the sake of completeness, it is supposed that N can be negative or positive. Although this may appear unrealistic in the context described, such a consideration will permit to compare more thoroughly solutions found in this section with the ones found in Section 2.2.
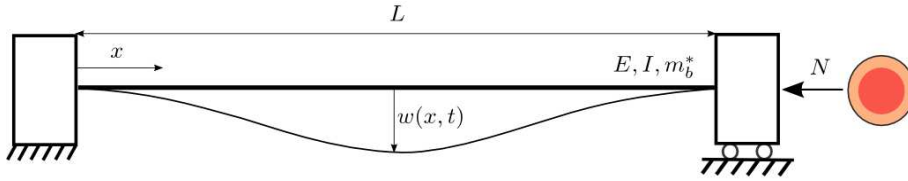
Figure 2.1: Case of study considered: a salmon fish egg cell imposes an axial force N when it touches the extremity of a CC beam. Straight bold line is the reference (undeformed) beam configuration. Thin line represents dynamical deformations imposed during vibration.

For this theoretical study, the beam is supposed to obey Euler-Bernouilli theory and the following assumptions are made:

- The beam is relatively long, namely its length L exceeds its width b and thickness h.

- The beam has a rectangular cross section S which is uniform over its entire length.

- The beam material is homogeneous, isotropic, and linearly elastic according to Hooke's law. The Young's modulus and density of this material are noted E and ρ_b, respectively.

- The beam motion is sinusoidal during vibration. Only the fundamental frequency of resonance is considered.

- The amplitude of vibration of the beam is much lower than any of the beam dimension so that shear deformation can be neglected.

- The beam is undamped and unforced.

Considering the above listed assumptions, the beam is governed by the following equation of motion [141]

$$EI\frac{\partial^4 w(x,t)}{\partial x^4} + N\frac{\partial^2 w(x,t)}{\partial x^2} + m_b^*\frac{\partial^2 w(x,t)}{\partial t^2} = 0 \tag{2.1}$$

where $m_b^* = \rho_b S$ and $I = \frac{bh^3}{12}$ are the mass per unit length and the moment of inertia of the beam, respectively.

2.1.1 Effects of an axial force on the fundamental frequency

Equation (2.1) is a linear, homogeneous partial-differential equation. Assuming that there is a separable solution $w(x,t) = W(x) Q(t)$, Eq. (2.1) can be transformed into a single differential equation

$$\frac{d^4 W(x)}{dx^4} + \sigma^2 \frac{d^2 W(x)}{dx^2} - \Omega^4 W(x) = 0 \tag{2.2}$$

where $\sigma^2 = \dfrac{N}{EI}$ and $\Omega^4 = \dfrac{m_b^* \omega^2}{EI}$.

In the case of an ideal CC beam, boundary conditions are

$$W(x)\Big|_{x=0} = 0, \quad \frac{dW(x)}{dx}\Big|_{x=0} = 0, \tag{2.3}$$

$$W(x)\Big|_{x=L} = 0, \quad \frac{dW(x)}{dx}\Big|_{x=L} = 0. \tag{2.4}$$

Substituting Eq. (2.2) into Eqs. (2.3-2.4) yields

$$1 - \cos(\alpha_1 L)\cosh(\alpha_2 L) + \frac{\sigma^2}{2\,\Omega^2}\sin(\alpha_1 L)\sinh(\alpha_2 L) = 0 \tag{2.5}$$

where

$$\alpha_1 = \sqrt{\frac{\sigma^2}{2} + \frac{1}{2}\sqrt{(\sigma^4 + 4\Omega^4)}} \qquad \text{and} \qquad \alpha_2 = \sqrt{-\frac{\sigma^2}{2} + \frac{1}{2}\sqrt{(\sigma^4 + 4\Omega^4)}}. \tag{2.6}$$

Equation (2.5) is a transcendental equation that can be solved numerically. In particular, if $N = 0$, the fundamental angular resonance frequency of a CC beam is[1]

$$\omega_1 = \frac{22.37}{L^2}\sqrt{\frac{EI}{m_b^*}}. \tag{2.7}$$

For numerical applications, a CC beam whose properties are listed in Table 2.1 is considered. These dimensions have been scaled in accordance with the size of the egg cell ($\sim$ 5mm) considered in the case of study. However, results and comments made afterwards would remain valid for a beam with any dimensions. Making use of these numerical values with Eq. (2.5) and Eq. (2.7), the evolution of the ratio ω/ω_1 as a function of the axial force applied N can be predicted. As seen in Fig. 2.2, the fundamental frequency of the CC beam increases when a tensile force is applied (i.e., for $N < 0$). By contrast, the frequency decreases in the case of a compressive force (i.e., $N > 0$). The amount of force applied to the beam can hence be estimated by measuring the amount of frequency variation.

---

[1] A detailed demonstration is given in appendix.

Length (L)	12.5 mm
Width (b)	0.25 mm
Thickness (h)	0.1 mm
Moment of inertia ($I = \frac{bh^3}{12}$)	2.08×10^{-17} m^4
Young's modulus (E)	212 GPa
Density (ρ_b)	8030 kg m^{-3}
Mass per unit length (m_b^*)	2×10^{-3} kg m^{-1}

Table 2.1: Numerical values of parameters for the thin beam considered in Fig. 2.1.
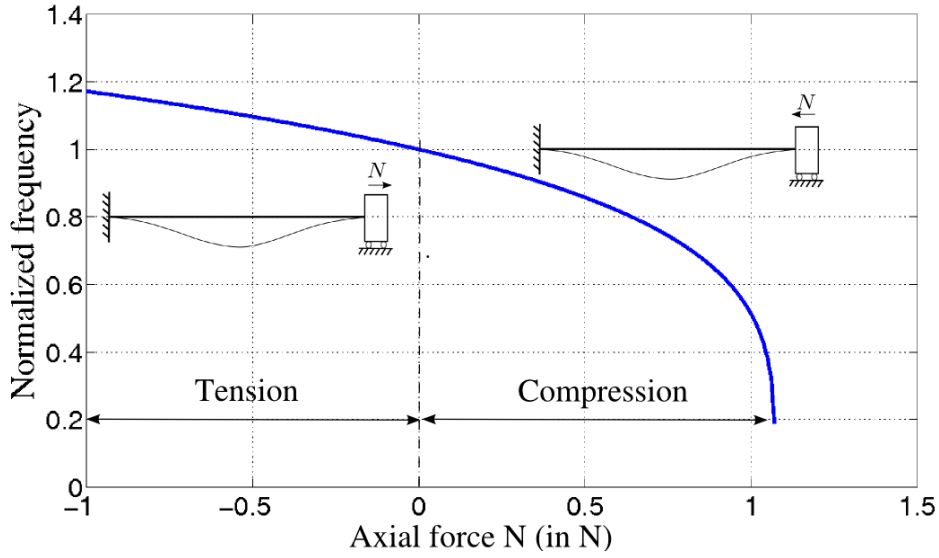
Figure 2.2: Evolution of the fundamental frequency ω_1 of a CC beam when a positive (compressive) or a negative (tensile) axial force N is applied.

For large force amplitudes (i.e., $|N| \geq 0.5$ N), it is interesting to note that the absolute value of the slope increases with a compressive force, which means that according to theory, the same amount of additional force can have a bigger effect if the beam is stressed with a compressive load. For small force amplitudes (i.e., $|N| \leq 0.5$ N), the amount of frequency variation Δ_ω is almost linearly related to the amount of force applied Δ_N. In such conditions, the force sensitivity s_F of the CC beam can thus be defined as

$$s_F = \frac{\Delta_\omega}{\Delta_N}. \tag{2.8}$$

2.1.2 Effects of an axial force on the first mode shape

Associated with ω_1 is a mode shape[2] $W(x)$

$$W(x) = C_1 \left[\sin(\alpha_1 x) + \lambda \cos(\alpha_1 x) - \frac{\alpha_1}{\alpha_2} \sinh(\alpha_2 x) - \lambda \cosh(\alpha_2 x) \right] \qquad (2.9)$$

where C_1 is a constant and

$$\lambda = \frac{\sin(\alpha_1 L) - \frac{\alpha_1}{\alpha_2} \sinh(\alpha_2 L)}{\cosh(\alpha_2 L) - \cos(\alpha_1 L)}. \qquad (2.10)$$
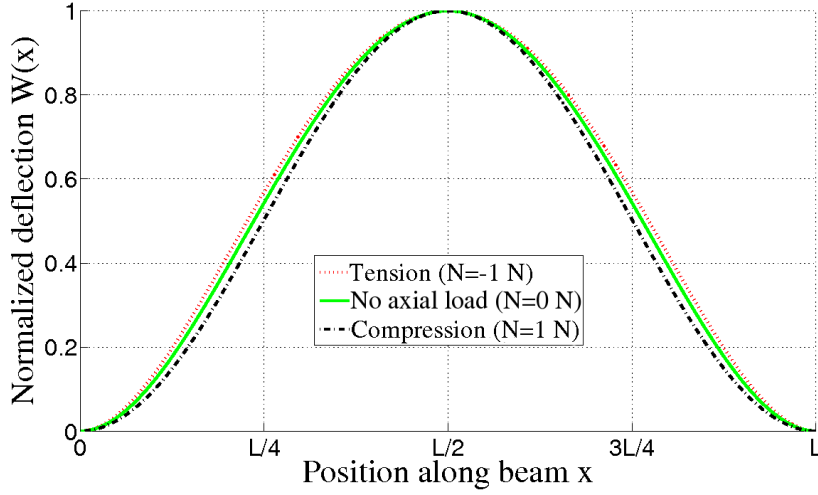
Figure 2.3: Effects of an axial force on the first mode shape of a CC beam.

If there is no axial force ($N = 0$), Eq. (2.9) becomes

$$W(x) = -C_1 \left[\sin(\Omega x) - \sinh(\Omega x) - \left(\frac{\cos(\Omega L) - \cosh(\Omega L)}{\sin(\Omega L) - \sinh(\Omega L)} \right) \left(\cos(\Omega x) - \cosh(\Omega x) \right) \right]. \qquad (2.11)$$

The first mode shape associated to ω_1 for a CC without axial force predicted by Eq. (2.11) is shown in Fig. 2.3 (solid line). By comparison, dashed and dotted lines represent the modes shapes when a tensile or compressive force of 1 N is applied to the beam. It can be observed that the initial mode shape is not significantly altered. For small force magnitudes, the impact of an axial force on the first mode shape of a CC beam is thus limited.

---

[2]Details about the derivation of the exact mode shape are also provided in appendix.

2.2 Vibrations of a CC beam subjected to an axial force: approximate solution via energy methods

In using conventional beam theory in the previous section, the analysis was restricted to small deflections and slopes. This allowed a relatively simple analytic solution to be found. However, in a number of practical situations, looking for an exact analytical solution becomes rapidly challenging (when not impossible). Such a situation will be encountered in Chapter 3 where the effects of large (i.e., nonlinear) static predeflections imposed to a resonant frame made of several coupled beams will be investigated.

As an alternative to exact solutions, energy methods can be conveniently used to grasp valuable insights on the dynamic behavior of complex resonant structures. As a first step, one here demonstrates that Lagrange's equation constitutes a powerful alternative to reasonably approximate the dynamics of a simple CC beam constrained by an axial force. Generally speaking, Lagrange's equation for a conservative system is [141]

$$\frac{\partial \mathcal{L}}{\partial q} - \frac{d}{dt}\frac{\partial \mathcal{L}}{\partial \dot{q}} = 0 \tag{2.12}$$

where q represents generalized coordinates, $\dot{q}$ is the time derivative of q, and the Lagrangian $\mathcal{L}$ is the difference between the kinetic energy V_{kin} and the potential energy V_{pot} of the system

$$\mathcal{L} = V_{kin} - V_{pot}. \tag{2.13}$$

For a CC beam of length L, the kinetic energy is [142]

$$V_{kin} = \frac{1}{2} m_b^* \int_0^L \left(\frac{\partial w(x,t)}{\partial t}\right)^2 dx. \tag{2.14}$$

When the beam is axially constrained, the total potential energy is the sum of two contributions $V_{pot} = V_b + V_a$. The first contribution V_b is related to the strain energy due to bending [142]

$$V_b = \frac{1}{2} EI \int_0^L \left(\frac{\partial^2 w(x,t)}{\partial x^2}\right)^2 dx. \tag{2.15}$$

The second contribution is due to the presence of the axial force N [143]

$$V_a = -\frac{1}{2} N \int_0^L \left(\frac{\partial w(x,t)}{\partial x}\right)^2 dx. \tag{2.16}$$

As in the previous section, $w(x,t) = W(x)\,Q(t)$. This time, however, a single mode energy analysis of the CC beam is conducted by assuming the displacement function $W(x)$. A trial function that satisfies geometric conditions for the first mode shape of a CC beam is [144]

$$W(x) = \frac{1}{2}\left[1 - \cos\left(\frac{2\pi x}{L}\right)\right]. \tag{2.17}$$
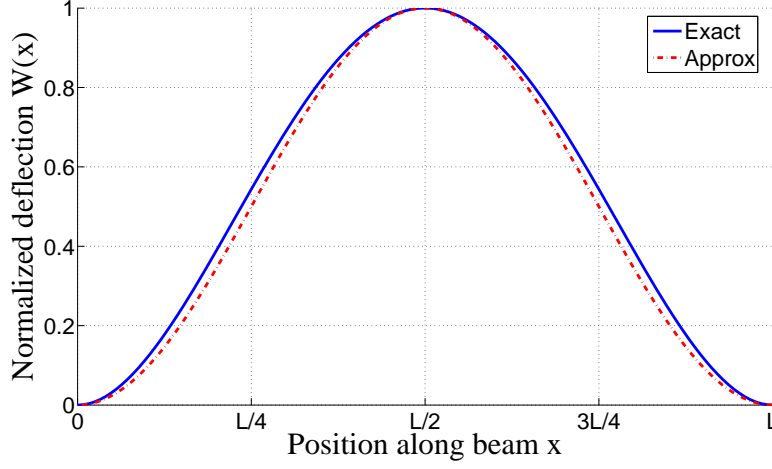
Figure 2.4: Comparison of the first mode shape of a CC beam (without axial load) predicted by Eq. (2.11) (solid line) and Eq. (2.17) (dashed line).

In Fig. 2.4, it can be observed that Eq. (2.17) is indeed a reasonable approximation when compared to the exact solution provided by Eq. (2.11). Then, energy expressions given by Eqs. (2.14-2.16) are evaluated for the assumed mode shape

$$V_{kin} = \frac{3}{16} m_b^* L \left(\frac{dQ(t)}{dt} \right)^2, \tag{2.18}$$

$$V_{pot} = \frac{1}{16} EIL \left(\frac{2\pi}{L} \right)^4 Q(t)^2 - \frac{1}{16} NL \left(\frac{2\pi}{L} \right)^2 Q(t)^2. \tag{2.19}$$

Lagrange's equation (2.12) can then be used to obtain the equation of motion for this single mode approximation

$$3 m_b^* \frac{d^2 Q(t)}{dt^2} + \left[EI \left(\frac{2\pi}{L} \right)^4 - N \left(\frac{2\pi}{L} \right)^2 \right] Q(t) = 0. \tag{2.20}$$

Since harmonic motion of the beam during oscillations is assumed, substituing $Q(t) \propto e^{j\omega t}$ into Eq. (2.20) yields

$$\omega^2 = \frac{EI}{3m_b^*} \left(\frac{2\pi}{L} \right)^4 - \frac{N}{3m_b^*} \left(\frac{2\pi}{L} \right)^2. \tag{2.21}$$

In the abscence of axial load, the fundamental frequency is

$$\omega_1 = \frac{22.79}{L^2} \sqrt{\frac{EI}{m_b^*}}. \tag{2.22}$$

45

It can be noticed that Eq. (2.22) is very similar to the result of Eq. (2.7) provided by the exact solution. The effects of the axial force N on the fundamental frequency of the CC beam can also be analysed with Eqs. (2.21-2.22) by considering the ratio ω/ω_1

$$\frac{\omega}{\omega_1} = \sqrt{1 - \frac{NL^2}{4\pi^2 EI}} \,. \tag{2.23}$$

For the same beam we considered in Section 2.1 (see Table 2.1), the evolution of Eq. (2.23) with respect to the axial force N is represented in Fig. 2.5 (dashed line).
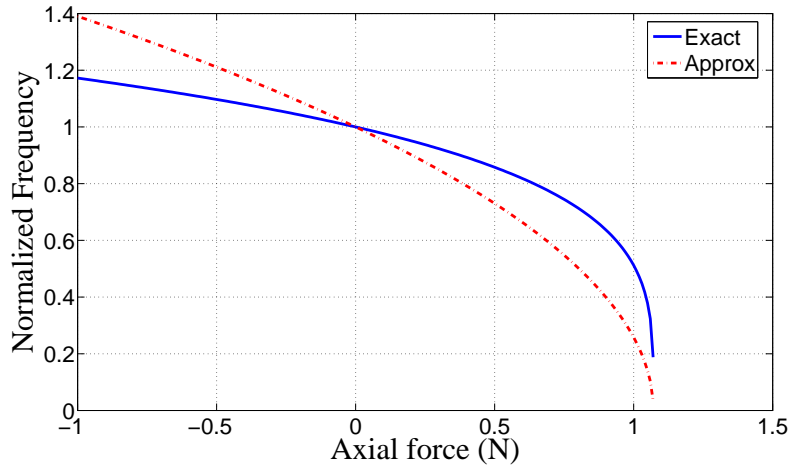
Figure 2.5: Frequency variation of a CC beam constrained by an axial force. Solid line represents the variation predicted by the exact solution of Section 2.1. In comparison, dashed line corresponds to the approximate solution based on Lagrange's equation and Eq. (2.17).

When compared to Eq. (2.5) (solid line), frequency variations predicted tend to be overestimated for tensile forces ($N < 0$) and underestimated for compressive forces ($N > 0$). Despite discrepencies with the exact solution, it is however demonstrated that Eq. (2.23) is sufficient to grasp the main dynamics of the CC beam under an axial force.

2.3 Vibration of a CC beam in fluids

So far, the CC beam was assumed to be undamped. In other words, all types of losses were neglected and the beam could be considered as vibrating in vacuum. Nevertheless, as stressed out in Chapter 1, one harsh constraint related to cell studies is that cells should always be kept in growth medium. Therefore, interaction between the CC beam and a cell must actually occur in a liquid environment. This section now shows that the initial dynamic of a resonant CC beam will be dramatically impacted as soon as the beam is plunged into liquids.

2.3.1 Presence of a fluid: impact on the resonance frequency and oscillation amplitude

The CC beam of Fig. 2.1 is now considered to be entirely immersed into a fluid. In order to neglect squeeze damping effects, the beam is supposed to be isolated in space so that it does not oscillate in the vicinity of any stationary surfaces [145]. Other assumptions previously made in Section 2.1 and Section 2.2 remain valid.

Studying the interaction between fluids and resonant beams proves to be a complex problem (see for instance [146, 147, 148]). An energy approach similar to the one of Section 2.2 can however be conveniently used to analyse such an interaction. The Lagrange equation introduced in Eq. (2.12) must however be extended. Indeed, in the presence of a surrounding fluid, a damping coefficient per unit length γ_a^* must be introduced [149]

$$\frac{d}{dt}\frac{\partial\mathcal{L}}{\partial\dot{q}} - \frac{\partial\mathcal{L}}{\partial q} + \frac{\partial\mathcal{D}}{\partial\dot{q}} = 0 \tag{2.24}$$

where the Rayleigh's dissipation function $\mathcal{D}$ is

$$\mathcal{D} = \frac{1}{2}\gamma_a^* \int_0^L \left(\frac{\partial w(x,t)}{\partial t}\right)^2 dx. \tag{2.25}$$

The beam is still supposed to oscillate harmonically. It is also assumed that the fluid does not affect the first mode shape so that it can be still described by Eq. (2.17). Evaluation of the Rayleigh's dissipation function then yields

$$\mathcal{D} = \frac{3L}{16}\gamma_a^* \left(\frac{dQ(t)}{dt}\right)^2. \tag{2.26}$$

The presence of a fluid also adds a mass per unit length m_a^*. Therefore, the new kinetic energy of the Lagrangian is

$$V_{kin} = \frac{3}{16} m_{tot}^* L \left(\frac{dQ(t)}{dt}\right)^2, \tag{2.27}$$

where $m_{tot}^* = m_b^* + m_a^*$. To isolate the effects exclusively engendered by the presence of the fluid, one assumes for a moment that the salmon egg cell does not touch the beam. If terms related to the axial force N are dropped, the total potential energy reduces to

$$V_{pot} = \frac{1}{16} EIL \left(\frac{2\pi}{L}\right)^4 Q(t)^2. \tag{2.28}$$

Making use of Eqs. (2.26,2.28), one obtains

$$m_{tot}^*\omega^2 + j\,\gamma_a^*\,\omega = \frac{EI}{3}\left(\frac{2\pi}{L}\right)^2. \tag{2.29}$$

If all terms are divided by m_b^*, the right hand side of Eq. (2.29) actually corresponds to Eq. (2.22). Accordingly, Eq. (2.29) can be rewritten

$$m_{tot}^* \, \omega^2 + j \, \gamma_a^* \, \omega = m_b^* \, \omega_1. \tag{2.30}$$

Solving Eq. (2.30) permits to predict the new angular frequency of the vibrating beam in fluids with respect to the undamped angular frequency ω_1, m_a^* and γ_a^* [150]

$$\omega_{fluid} = \sqrt{ -\frac{\gamma_a^{*2}}{2 \, m_{tot}^{*}{}^{2}} + \omega_1^2 \sqrt{ \frac{\gamma_a^{*4}}{4 \, m_{tot}^{*}{}^{4}} \, \omega_1^4 + \frac{m_b^{*2}}{m_{tot}^2} } } \tag{2.31}$$

where $m_{tot} = m_{tot}^* \, L$.

The mass and damping added by the fluid also affect the oscillation amplitude of the beam. In [150], it has been shown that the oscillation amplitude with respect to the angular frequency is

$$A(\omega) = \frac{A_0}{\sqrt{m_{tot}^2 \, (\omega^2 - \omega_{fluid}^2)^2 + \gamma_a^2 \, \omega^2}} \tag{2.32}$$

where $\gamma_a = \gamma_a^* \, L$ and A_0 is the initial amplitude of the CC beam.

To calculate ω_{fluid} and $A(\omega)$, parameters m_a^* and γ_a^* must be known. To evaluate the latter, it is easier to assume that the surfaces which interact with the fluid are approximately the same for a beam with a rectangular cross section and for a beam with a circular cross section. This approximation proves to be reasonable when considering transverse (i.e., out-of-plane) oscillations of the beam. For a circular beam, the added mass per unit length is given by [151]

$$m_a^* = \rho_{fluid} \frac{\pi}{4} \, b^2 \, \Gamma_1 \tag{2.33}$$

whereas the damping coefficient per unit length is [151]

$$\gamma_a^* = \rho_{fluid} \frac{\pi}{4} \, b^2 \, \omega \, \Gamma_2. \tag{2.34}$$

In Eqs. (2.33) and (2.34), ρ_{fluid} is the density of the fluid and the terms Γ_1 and Γ_2 are the real and imaginary part of the hydrodynamic function Γ [148]

$$\Gamma = 1 + \frac{4 \, j \, K_1 \, (-j \, \sqrt{j \, R_e})}{\sqrt{j \, R_e} \, K_0 (-j \, \sqrt{j \, R_e})}. \tag{2.35}$$

In Eq. (2.35), K_0, K_1 are Bessel functions of the second kind and R_e is the Reynolds number [152]

$$R_e = \frac{\rho_{fluid} \, \omega \, b^2}{4\eta} \tag{2.36}$$

where η is the dynamic viscosity of the fluid.

2.3.2 Energy losses: notion of quality factor (Q factor)

For an oscillating beam, the Q factor is a measure of energy losses. Indeed, high energy losses imply a low Q factor. Generally, three main types of energy loss mechanisms are considered for evaluating the overall Q factor of a resonant beam [153]

$$\frac{1}{Q} = \frac{1}{Q_{int}} + \frac{1}{Q_{anch}} + \frac{1}{Q_{fluid}} \tag{2.37}$$

where $1/Q_{int}$ is related to structural damping and corresponds to the energy dissipated internally within the resonator's material, $1/Q_{anch}$ represents the energy coupled through the beam supports to a surrounding solid and $1/Q_{fluid}$ is the energy lost due to the presence of a surrounding fluid.

Structural damping is mainly caused by material internal frictions. It becomes only prominent under vaccum conditions. Meanwhile, anchor loss is a frequency-dependent loss mechanism. The correlation analysis with experiments has revealed that the anchor loss becomes the primary energy loss source only for beam resonators whose center frequency increases beyond 20-50 MHz [154]. For a beam surrounded by a viscous fluid, it has been shown that viscous damping usually serves as the major energy dissipation source and dominates all other energy loss mechanisms [155, 156, 157, 158]. To a first approximation, the overall Q factor of a beam can hence be reduced to

$$\frac{1}{Q} \approx \frac{1}{Q_{fluid}}. \tag{2.38}$$

Then, estimation of the overall Q factor can be conducted by using a general definition [159]

$$\frac{1}{Q} = \frac{1}{2\pi} \frac{V_{loss}}{V_{kin}} \tag{2.39}$$

where V_{kin} represents the peak kinetic energy of the beam and V_{loss} is the dissipated energy per cycle per time period $T = 2\pi/\omega$.

When a CC beam vibrates at its first mode of vibration with a maximal deflection equal to 1, the kinetic contribution is [151]

$$V_{kin} = \frac{1}{2} m_{tot}^* \omega^2 \int_0^L W(x)^2 dx. \tag{2.40}$$

Meanwhile, V_{loss} can be found by estimating the averaged dissipated power per unit length due to the liquid surrounding the beam [151]

$$P_{loss}^* = \frac{1}{2} \gamma_a^* W(x) \tag{2.41}$$

where γ_a^* is the damping coefficient per unit length according to Eq. (2.34).

Integrating Eq. (2.41) over the time period T and the length of the beam yields

$$V_{loss} = \int_0^L \int_0^T P_{loss}^* \, dt \, dx = 2\pi\omega\gamma_a^* \int_0^L W(x)^2 dx \,. \tag{2.42}$$

Making use of Eqs. (2.39-2.40) and Eq. (2.42), the Q factor can thus be written

$$Q = \frac{(m_b + m_a)}{2\gamma_a} \omega_{fluid} \tag{2.43}$$

where $m_a = m_a^* L$, $m_b = m_b^* L$ and $\gamma_a = \gamma_a^* L$.

2.3.3 Vibration of a beam in air and in water: numerical application

For the beam of Table 2.1, Eqs. (2.31) and (2.43) can now be utilized to calculate the fundamental angular frequency and the Q factor when the beam vibrates in air and in water.

Beam dimensions (mm)			Air $\rho_{fluid} = 1.18\,kg\,m^{-3}$ $\eta = 1.18\times10^{-5}Pa\,s$		Water $\rho_{fluid} = 997\,kg\,m^{-3}$ $\eta = 8.59\times10^{-4}Pa\,s$	
L	b	h	ω_1 (rd/s)	Q	ω_1 (rd/s)	Q
12.5	0.25	0.1	21629.31	2474.53	19127.77	17.73

Table 2.2: Values of angular frequency and Q factor for the CC beam of Table 2.1 vibrating in air and in water.

Results are reported in Table 2.2. Under atmospheric pressure (i.e., in air), the initial fundamental frequency predicted is 21629.31 rd/s. However, if the same beam is plunged into water, its fundamental frequency drops to 19127.77 rd/s. More importantly, the Q factor is reduced by approximately 72%. This diminution has a drastic impact on the frequency response of the beam. Indeed, the Q factor is a figure of merit of the oscillating beam: the higher the Q factor, the sharper and more pronounced the resonance. This is confirmed in Fig. 2.6 where Eq. (2.32) has been used to predict the frequency response of the beam in air and in water.

As it can be observed, the resonance peak is indeed significantly wider when the beam oscillates in water. Furthermore, the resonance amplitude of the beam in water is ~90% less that the resonance amplitude in air. This is a severe restriction for using the CC beam as an efficient force sensor in cell studies. Indeed, a less pronounced resonance is less easily distinguishable from nonresonant vibrations. In water, the deflection amplitude of the beam may even not be high enough for good readout sensitivity, leading to a low signal to noise ratio.
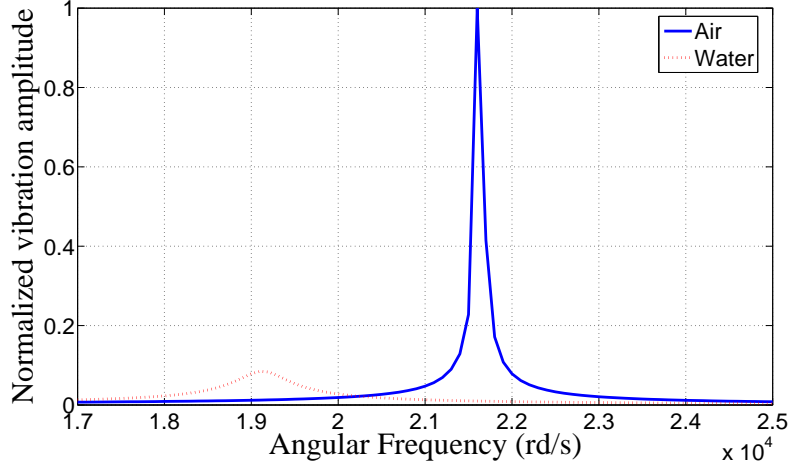
Figure 2.6: Frequency response for a CC beam (see properties in Table 2.1) when it vibrates in air and when it vibrates in water.

These phenomena (i.e., diminutions of the angular frequency, of the Q factor and of the oscillation amplitude) can mainly be explained by the density of the water. Indeed, the density of water is ∼850 times higher than the density of air. The amount of added mass m_a is hence considerably higher when the beam is surrounded by water than when it is surrounded by air. Thus, to increase beam performances in cell studies, the beam should be dimensioned to minimize the mass added by the presence of water.

2.4   Vibrations of a CC beam in fluids: parametric analysis

Section 2.3 has shown that the presence of a fluid can dramatically deteriorate the dynamics of a resonant beam. Nevertheless, a single beam with fixed dimensions (see Table 2.1) was considered so far. But what happens if the dimensions change? In actuality, it turns out that the fundamental frequency ω_1 and the Q factor are both intimately correlated to the beam geometry. Likewise, the impact of the fluid is also dependent upon the beam size. One may then wonder what beam dimensions should be selected to enhance beam performances. In this section, we analyse the evolution of relevant parameters as a function of beam dimensions.

2.4.1   Varying the beam geometry: influence on the mass added by a fluid

Obviously, changing beam dimensions changes the beam mass m_b. Nonetheless, it is rather intuitive that variations of beam dimensions will also have an impact on the mass added by a surrounding fluid m_a. To analyse this potential effect, Eq. (2.33) is used for calulating m_{tot}^* (which includes both contributions m_a^* and m_b^*) for a beam submerged into water ($\rho_{fluid} = 1.2\,kg\,m^{-3}, \eta = 1.8 \times 10^{-5}\,Pa\,s$). For different cross sections (b, h),

51

the evolution of m_{tot} with respect to the beam length is then plotted in Fig. 2.7.
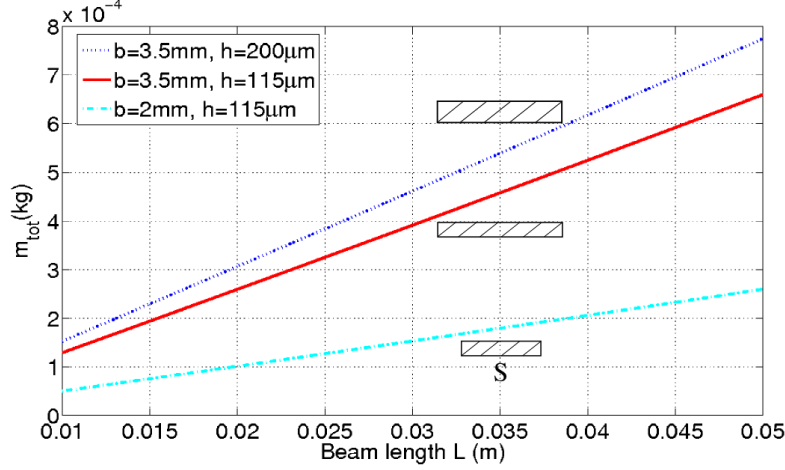
Figure 2.7: Evolution of m_{tot} with respect to the beam length for a CC beam immersed in water. Dashed rectangles illustrate variations of the beam cross sectional areas S.

Figure 2.7 confirms that the amount of added mass is mainly correlated to the surfaces of the beam that are the most exposed to the surrounding fluid. In the case of transverse vibrations, these most influent surfaces are the top and bottom surfaces whose area is $L\,b$. For all pairs (b, h), m_{tot} indeed becomes more and more prominent as the beam length increases. In the same manner, the parameter m_{tot} is sensitive to width changes. For instance, for a beam 115 μm thick, the wider the beam the higher m_{tot}. On the contrary, varying the beam thickness has a limited influence on m_{tot}. Thereby, for a beam 3.5 mm wide, decreasing the thickness from 200 μm to 115 μm does not significantly reduce m_{tot}. Consequently, to limit the mass added by the presence of a surounding fluid, the beam should be narrow and short.

2.4.2 Varying the beam geometry: influence on the resonance frequency and Q factor

In true fact, trying to adapt beam dimensions in order to limit the mass added by the surrounding water also has an impact on the resonance frequency and the Q factor of the beam. Table 2.3 reports the evolution of these two fundamental parameters for beams with different geometries that oscillate in air and in water.

Several interesting facts can be deduced from the analysis of Table 2.3. As a general trend, it can be observed that higher Q factors can be achieved with higher resonance frequencies. The most efficient way to increase the resonance frequency is to reduce the beam length. For example, if a beam 1 mm wide and 0.2 mm thick is shorten by a factor 2, its resonance frequency is multiplied by 4 in air and by ~3.5 in water.

Beam dimensions (mm)			Air		Water	
L	b	h	$\omega_1 \, (rd/s)$	Q	$\omega_1 (rd/s)$	Q
15	1	0.2	30037.91	6441.36	24513.81	41.18
15	1	0.1	15013.60	2263.47	10576.47	16.81
15	0.5	0.1	15017.93	2170.87	12145.02	14.48
30	1	0.2	7509.19	3144.48	6907.86	20.53
30	3	0.2	7504.87	3276.48	4757.91	26.58
30	3	0.1	3748.68	1149.63	1875.04	11.89

Table 2.3: Values of resonance frequency and Q factor for various CC beams vibrating in air and in water.

Comparatively, tuning the beam width has a limited impact on the resonance frequency, especially if the beam oscillates in air. Indeed, even if the width of a beam 30 mm long and 0.2 mm thick is tripled, the resonance frequency remains almost the same. This remark is not valid anymore when the beam oscillates in water. Indeed, because the density of water is ∼850 times higher than the density of air, a substantial amount of mass is added when the top and bottom surfaces of the beam are enlarged. Thereby, the resonance frequency of a beam 30 mm long and 0.2 thick is reduced by ∼30% if its width is multiplied by 3.

However, regardless of the nature of the fluid surrounding the beam, it is interesting to note that the Q factor is not very sensitive to variations of the beam width. Surprisingly, higher Q factors are even obtained for wider beams, a behavior that seems a little counterintuitive. In other words, this means that a reduction of the beam planar aspect ratio L/b (while keeping constant L and h) is in favour for an increase of the Q factor, a fact that also find confirmation in experiments [160]. On the contrary, the Q factor is strongly correlated to the beam thickness. By way of illustration, for a beam 15 mm long and 1 mm wide, doubling the thickness of the beam permits to multiply the Q factor by ∼2.8 in water. Consequently, to achieve a high resonance frequency and a high Q factor, the beam should be short whereas the ratio b/h should be minimized.

2.4.3 Varying the beam geometry: influence on the force sensitivity

A last relevant parameter to consider is the beam force sensitivity s_F defined in Section 2.1.1 (see Eq. (2.8)). As seen in Chapter 1, most biological studies involve either suspension cells with a diameter of ∼100-150 μm (e.g., embryos or oocytes), or adherent cells (e.g., fibroblasts, HeLa cells, endothelial cells) whose size can be as small as few micrometers. Depending of the type of cells investigated, forces to be measured range from nN to mN. The capability of the resonant beam to measure infinitesimal amount of force should hence be optimized. Regarding the beam dimensions listed in Table 2.1,

measuring such small forces is not possible. Indeed, in our case of study, the beam was dimensioned to interact with an egg cell having a large diameter of 5 mm. Nonetheless, varying aspect ratios for this beam allows us to analyse tendencies that will remain valid for beams with any dimensions. By substituting different values of length L, width b and thickness h into Eq. (2.23), Fig. 2.8 can be plotted.
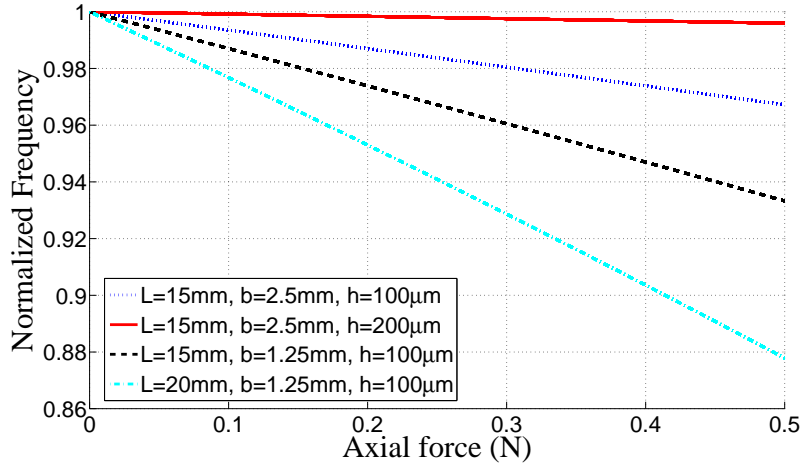
Figure 2.8: Frequency variations for CC beams with different geometries under a compressive force.

Several conclusions can be drawn from the analysis of Fig. 2.8. First, for a beam with a length of 15 mm and a width of 2.5 mm, increasing the thickness from 100 μm to 200 μm decreases its force sensitivity. By contrast, for a beam of constant ratio L/h (i.e., $L = 15$ mm and $h = 100$ μm), dividing by two the width of the beam decreases its stiffness and hence improves the force sensitivity. However, it is clear that for the same amount of force applied, the amount of frequency change is significantly higher for the longest beam ($L = 20$ mm).

Hence, for a particular ratio b/h, a resonant CC beam subjected to an axial force should be preferably long to achieve a high force sensitivity. However, this is in contradiction with dimensions required for increasing the resonance frequency and improving the Q factor. As discussed above, increasing beam length will indeed augment the mass added by the presence of water. It will hence lower both the resonance frequency and the Q factor. As a consequence, only a trade-off appears possible because all parameters cannot be optimized simultaneously: the maximization of the force sensitivity leading to the degradation of the Q factor and *vice versa*.

2.5   Conclusion

This chapter has demonstrated that a simple CC beam oscillating at its fundamental frequency could in theory be used to measure the axial force imposed by a salmon fish egg cell. An exact solution has been derived to predict how the resonance frequency should vary with respect to the axial force applied. An energy approach has also been introduced and compared with the exact solution. Similar results have been found. In addition, energy methods have allowed us to conveniently study realistic cases. In particular, because real cell studies must be conducted into liquids, the effects of a surrounding fluid on the beam dynamics have been studied. Severe limitations on the beam performances have been observed and discussed. When the beam is plunged into water, the initial resonance frequency shifts to a smaller value. Moreover, the frequency response becomes significantly wider and the resonance amplitude is dramatically reduced. This leads to a very poor quality factor, which can be as low as 10-20, and a low force sensitivity. To minimize this set of negative effects, the possibility to change the length and the cross section of the beam has been investigated. Nonetheless, it has been revealed that beam performances could not be enhanced simultaneously. Indeed, trying to optimize the force sensitivity by varying the beam geometry leads to the deterioration of the quality factor and *vice versa*. Hence, it is clear that a simple CC beam is not a satisfying option to conduct proper cell analysis in a liquid environment. To measure the Young's modulus of cells cultured in growth medium without the aforementioned problems, Chapter 3 next introduces a novel structure made of two beam resonators that can be exploited to measure forces applied on cells without the need to plunge them in the liquid.

Chapter 3

Design of a planar resonant structure sensitive to out-of-plane forces

In the context of this dissertation, one seeks to evaluate the Young's modulus of adherent and suspension cells. A quantitative measure of the elastic properties of living cells can indeed lead to potential breakthroughs in biotechnologies and medicine, with relevant applications in the diagnosis of cell-based degenerative diseases (e.g., cancer, malaria). To determine the Young's modulus of a cell, it is necessary to measure the force applied to deform the cell. To that purpose, Chapter 1 has underlined that, compared to force sensors operating in a static mode, resonant beams may be a valuable option to achieve high force sensitivity with less suceptibility to noise sources. Accordingly, Chapter 2 has investigated the possibility to use a CC beam to measure interaction forces with a single suspension cell. Unfortunately, it has been concluded that such a simple structure is not appropriate to measure forces on cells maintained in a growth medium. Performances of CC beams are indeed dramatically reduced in the presence of a surrounding liquid. Furthermore, with a CC beam, it is mandatory to apply the force to be sensed at the extremeties of the beam. In experimental conditions, such a configuration would actually be very unpractical to use for measuring forces on cells anchored to a surface. This chapter still focuses on force measurement aspects and introduces a novel resonant structure designed to bring new solutions to these problems.

To discuss this structure, the chapter is organized in five sections. First, Section 3.1 provides an overall description of the structure. Key advantages offered by the structure are also discussed. To finely grasp the behavior of the structure, energy methods are used in Section 3.2 in order to theoretically investigate the static and dynamic behaviors of the structure. In light of theoretical predictions, Section 3.3 provides a discussion that explains how the structure dimensions have been selected in order to optimize performances while taking consideration of fabrication constraints. In Section 3.4, a numerical application is provided to predict the sensitivity of the structure. At last, concluding remarks are given in Section 3.5.

3.1 Overall description and key features of the structure

As already discussed, it is now clear that an oscillating CC beam cannot be used in a satisfying manner for measuring forces on cells that are cultured in a growth medium. In order to overcome the limitations inherent to such a configuration, the structure shown in Fig. 3.1 is introduced.
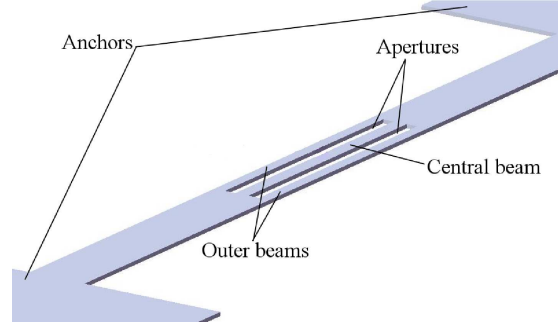
Figure 3.1: Three dimensional schematic illustrating the concept of the planar structure proposed in this work.

This structure is actually a modified CC beam which incorporates two rectangular apertures. Alternatively, it can be viewed as two cantilevers serially linked via three parallel beams. As seen in Fig. 3.1, the thickness is constant for the whole structure. The three beams (i.e., the central beam and the two outer beams) also have the same length. Provided that the width of the central beam is twice the width of the two outer beams, and if the structure is mechanically excited, it provides the modes shapes reported in Fig. 3.2. For cell studies, the third mode shape is of particular interest. From now on and throughout the chapter, only this mode shape will be considered.

As it can be seen in Fig. 3.2(c), the mode shape selected is an antisymmetrical vibration mode where the two outer beams oscillate vertically (out-of-plane mode) with a phase lag of 180 degrees (i.e., they oscillate in antiphase). In the mean time, the central beam remains immovable. Because the central steady beam is attached to the adjacent outer beams that oscillate, this vibration mode actually permits to measure a force applied perpendicular to the central beam via frequency shifts of the outer beams (this will be demonstrated through a thorough theoretical analysis in Section 3.2). Hereafter, we mention and discuss the advantages and possibilities offered by this mode shape.

- First advantage: the structure can be used as a versatile cell substrate sensitive to out-of-plane forces

Although force sensors constituted of several oscillating beams have been previously reported in the literature (e.g., [161, 162, 163]), these sensors could only measure axial forces applied to their extremities (i.e., in-plane forces), as in the case of the CC beam studied in Chapter 2. To measure forces perpendicular to the sensors' plane (i.e.,
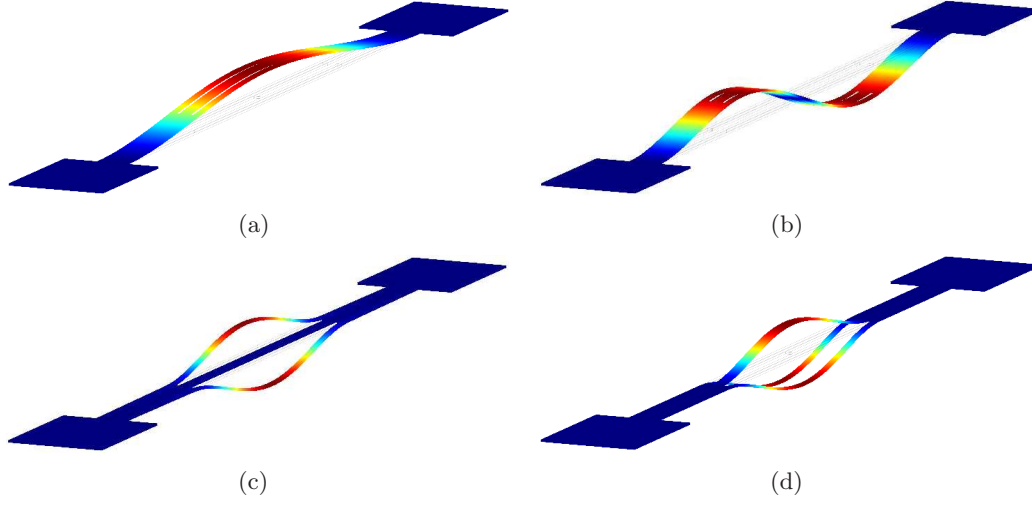
Figure 3.2: Mode shapes predicted by finite element analysis (FEA) conducted with COMSOL V.4 Multiphysics package for the structure represented in Fig. 3.1. (a) First mode shape; (b) Second mode shape; (c) Third mode shape; (d) Fourth mode shape.

out-of-plane forces), mechanical converters needed to be used (e.g., [164, 165, 166]). Unfortunately, such configurations would be unpratical for conduction mechanical studies on cells. Unlike in previous devices reported, the mode shape of Fig. 3.2(c) intrinsically permits to measure out-of-plane forces. This is an interesting feature in our context. Indeed, it enables the use of the central steady beam as a force sensitive cell substrate where cells could be placed. This concept is illustrated in Fig. 3.3.
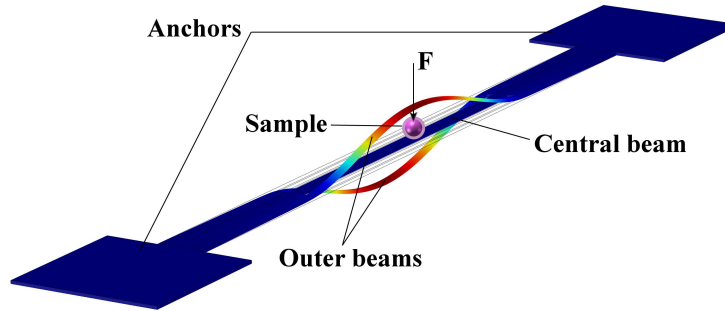
Figure 3.3: Concept of a force sensitive cell substrate illustrated with a suspended cell (trapping system for maintaining the cell not represented). To extract the elastic properties of a cell, the third vibration mode of the structure of Fig. 3.1 is exploited: the two outer beams oscillate in antiphase whereas the cell is placed on the third central beam which remains immovable.

Thereby, the central steady beam could be adapted for positioning both suspended and adherent cells. Although such an adaptation will not be addressed in this work, one

might for instance envision to integrate a microwell similar to those reported in [167] for positioning and maintaing an individual suspension cell. Alternatively, the half span of the central beam could be coated with biochemicals to culture a few adherent cells.

- Second advantage: the structure can be replicated for matrix configurations

The structure of Fig. 3.1 is a planar structure that has been designed to be MEMS compatible. In other words, it is possible to scale it down via microfabrication processes. One can hence reasonably envision to replicate the structure. In order to increase cell analysis rates, a matrix incorporating multiple structures could be produced for the characterization of tens of cells in parallel. Such a feature might permit to obtain valuable preliminary statistical results within minutes, irrespective of the type of cell investigated.

- Third advantage: the structure can be equipped with a fluidic system

Because the structure provides a steady area and is MEMS compatible, one can foresee to exploit the steady central beam for implementing a fluidic system. Such an option is inspired from works reported in [168, 169, 170] where the authors demonstrated the feasibility to use open microfluidic channels (see Fig. 3.4(a)) for applying mechanical forces with external nanoprobes on individual cells. It is however worth noticing that in these references, the microchannel is only used for cell delivery. To monitor forces applied to the cells, forces must be measured via the external nanoprobe. As discussed in Chapter 1, force measurement artifacts can however occur when such a nanoprobe enters in contact with the surface of the liquid contained in the microchannel (e.g., occurence of capillary forces). Fig. 3.4(b) shows that a similar open microchannel could be implemented into the planar structure by using microfabrication processes. Thereby, the delivery of culture medium could be ensured to the cells positioned onto the central beam. However, the microchannel would become inherently force sensitive, ideally limiting force measurement artifacts. The possibility to implement such a key feature is strengthen by other works that reported the fabrication of buried microchannels into resonant structures that aimed at detecting the presence of biomolecules into liquid samples [171, 172, 173].

- Fourth advantage: the structure does not need to be immersed into liquids

Chapter 2 has stressed out that performances of conventional CC beams are dramatically reduced as soon as the beams are plunged into a liquid environment. However, this critical issue is resolved with a structure that integrates a fluidic system as represented in Fig. 3.4(b). Indeed, cells can be kept in cell medium providing vital nutrients. In the mean time, because the microchannel is connected to the adjacent outer beams, the latter can sense an external force applied to the cells without the need to be immerged into the liquid. With the outer beams oscillating in air, the quality factor is not altered anymore and high performances can be guaranteed.
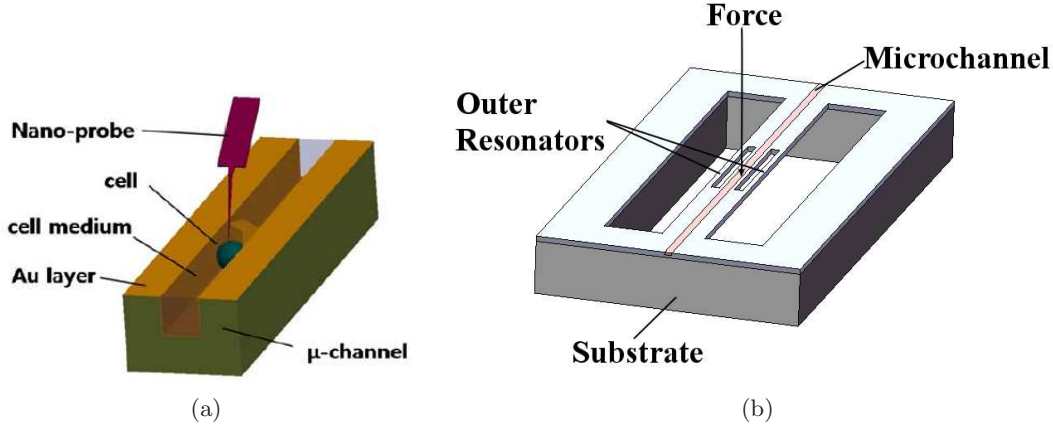
Figure 3.4: (a) Illustration of an open microfluidic channel for cell studies, as reported by Ryu et al. [169]. Forces applied to the cells must be measured via an external nanoprobe; (b) Conceptual view showing a microfabricated structure equipped with a similar open microfluidic channel. Here, the microchannel becomes intrinsically force sensitive.

3.2 Theoretical analysis

3.2.1 Preliminary remarks

The adjunction of an open microfluidic channel to the planar structure appears as a valuable concept, worth to be tested. If such a microchannel can be etched via microfabrication processes, it will be seen that precision wire cut electric discharge machining (EDM) was favoured for the fabrication of the prototype reported in Chapter 4. Wire cut EDM, however, was inappropriate for etching an open microchannel. Consequently, and for a better comparison between the theoretical results of this chapter and the experimental results provided in Chapter 4, the presence of an open microchannel is not considered in the following theoretical analysis. Nevertheless, it is worth noticing that the absence of the microchannel is not a critical issue. Finite element analysis (FEA) indeed shows that the working principle of the structure is not fundamentally affected by the presence or the absence of an open microchannel. Although slight discrepencies or bias may occur, the overall analysis and results provided in the rest of this chapter remain valid for a structure with or without a microchannel.

3.2.2 Static behavior: large deflection of the planar structure

To understand how a force F applied perpendicular to the central beam can be measured, it is first necessary to gain some insights into its static behavior. For convenience, the whole structure is supposed to be symmetric. Without loss of generality, a symmetric structure indeed permits to study the deflection of the entire structure by considering only one fourth of the structure, as sketched in Fig. 3.5.
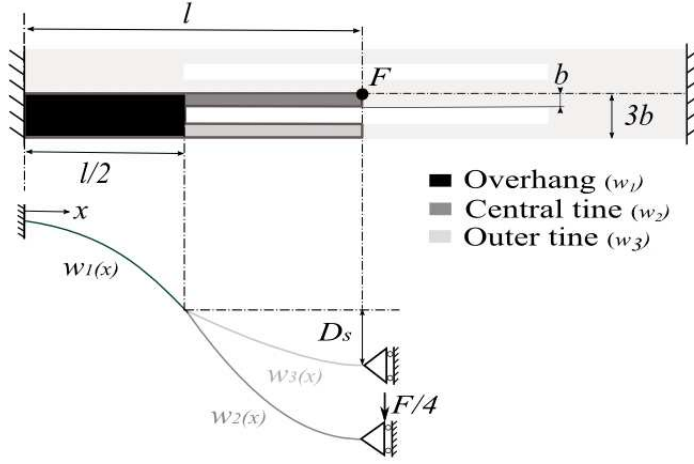
Figure 3.5: Top: for predicting the quasi-static deflection of the structure, only the darker *"tuning fork"* (top view) is considered. Bottom: equivalent one-dimensional model (side view) of the colored beams (proportions exaggerated for illustration purposes).

As it can be observed, this quarter structure has a shape similar to a tuning fork. It is composed of three segments: the overhang (colored in black), the central tine (colored in dark gray), and the outer tine (colored in light gray). To analyse the deflection of this tuning fork (and hence of the whole structure), it is assumed that:

- The three segments satisfy Euler-Bernouilli beam theory so that assumptions made at the beginning of Chapter 2 apply.

- During deflection, the length of each segment increases. This length increase produces some axial stress which can increase the stiffness of the tuning fork. This effect, often termed *midplane stretching* in the literature, may appear even for deflections that are not especially large. It is thus an important effect to consider to guarantee accurate predictions.

Nonetheless, it is worth stressing out that the midplane stretching effect is inherently a nonlinear phenomena. In true fact, trying to find an exact solution for a structure composed of several beams while taking into account such a nonlinear phenomenon can become challenging. Indeed, it then becomes necessary to solve coupled differential equations that involve integrals. This quickly leads to complex calculations. On the other hand, energy based methods offer a powerfull alternative. In particular, they permit to move from a differential eigenvalue context to an algebraic eigenvalue context. The problem then becomes quite straightforward to solve. Moreover, Chapter 2 has already revealed that energy techniques can be safely used to grasp the main behavior of elastic beams (see Section 2.2). Consequently, to predict the maximum displacement

of the outer tine when a force F is applied at the extremity of the central tine, an energy approach is favoured.

First, one-dimensional coordinate functions are used to approximate the displacement field of each segment. To guarantee enough degrees of freedom, the flexural displacement $w_{1,2,3}(x)$ of each segment is modeled by third order polynomial expressions

$$
\begin{cases}
w_1(x) = a_0 + a_1\,x + a_2\,x^2 + a_3\,x^3 \\
w_2(x) = a_4 + a_5\,x + a_6\,x^2 + a_7\,x^3 \\
w_3(x) = a_8 + a_9\,x + a_{10}\,x^2 + a_{11}\,x^3\,.
\end{cases}
\tag{3.1}
$$

The three polynomials in Eq. (3.1) are then used to calulate the total potential energy stored by the tuning fork during deflection

$$
U_{tf} = U_b + U_s
\tag{3.2}
$$

where U_b is the sum of strain energies developed by each segment during bending

$$
U_b = \sum_{i=1}^{3} \frac{1}{2}\,EI_i \int_0^{l/2} \left(\frac{d^2 w_i}{dx^2}\right)^2 dx.
\tag{3.3}
$$

In Eq. (3.3), I_i are the moments of inertia of the three segments with $I_1 = bh^3/4$ and $I_2 = I_3 = bh^3/12$, respectively.

In addition, U_s is the sum of energy contributions due to the midplane stretching of the segments that occurs during deflection

$$
U_s = \sum_{j=1}^{3} \frac{EA_j}{4l} \left[\int_{c_j}^{d_j} \left(\frac{dw_j}{dx}\right)^2 dx\right]^2
\tag{3.4}
$$

where $c_1 = 0$, $d_1 = l/2$, $c_{2,3} = l/2$ and $d_{2,3} = l$. A_j in (3.4) represents the cross section areas of the three segments with $A_1 = 3bh$ and $A_{2,3} = bh$. The total potential energy function can hence be written as

$$
\Phi = U_{tf} - W
\tag{3.5}
$$

where $W = F\,w_2(l)$ is the work done by the punctual force F.

Applying the principle of minimum potential energy, one sets for each unknown coefficient a_i

$$
\frac{\partial\,\Phi}{\partial\,a_i} = 0.
\tag{3.6}
$$

The problem is then augmented with Lagrange multipliers by considering a set of constraints. To obtain satisfactory results, mechanical constraints do not need to be considered. Enforcing geometrical constraints is indeed enough to provide an accurate solution.

For instance, because the overhang is clamped at $x = 0$, displacement and slope are both zero

$$w_1(0) = \frac{d\,w_1}{dx}(0) = 0. \tag{3.7}$$

From this, it can be immediately concluded that $a_0 = a_1 = 0$. Additional geometrical constraints can be expressed for each segment's extremity. Thereby, assuming that the central tine and the outer tine are rigidly linked to the overhang at $x = l/2$, the following conditions can be enforced

$$w_1(l/2) = w_2(l/2) = w_3(l/2), \tag{3.8}$$

$$\frac{dw_1}{dx}(l/2) = \frac{dw_2}{dx}(l/2) = \frac{dw_3}{dx}(l/2). \tag{3.9}$$

Finally, because only one-fourth of the whole structure is considered, the central and outer tines are terminated by sliding conditions, as skecthed in Fig. 3.5. Accordingly, their slope at $x = l$ must be zero

$$\frac{dw_2}{dx}(l) = \frac{dw_3}{dx}(l) = 0. \tag{3.10}$$

The augmented system can then be numerically solved for different values of F. To compute such a system, an algorithm such as the one reported in [174] can be used. The interested reader is invited to consult the original reference for further details on this algorithm.

3.2.3 Dynamic analysis: effects of a static predeflection on the oscillation of the outer beams

With the tuning fork illustrated in Fig. 3.5, previous section has introduced a numerical approach to predict the deflection profile and the deflection amplitude of the outer beams when a static force F is applied to the central beam. It is now supposed that a proper mechanical excitation is provided to the whole structure, so that the vibration mode where the outer beams oscillate in antiphase is activated (see Fig. 3.2(c)). This section demonstrates that, if the force F is applied while the outer beams oscillate, the variations of deflection imposed by F actually impacts the initial resonance frequency of the outer beams.

To demonstrate such a coupling between static and dynamic behaviors, a symmetric structure again simplifies the analysis. Indeed, and since we are only interested in the antisymmetrical vibration mode illustrated in Fig.3.2(c), valuable insights into the structure's dynamics can be grasped by restricting the analysis to a single outer beam (see Fig. 3.6).

To a first approximation, one can choose to model the outer beam as a hinged-hinged beam terminated by two rotational springs of stiffness k_{r1} (see Fig. 3.6). The presence
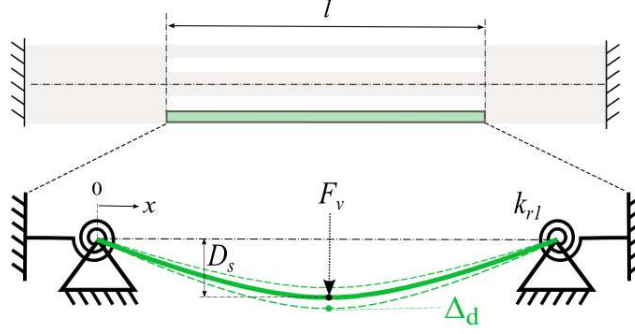
Figure 3.6: For predicting frequency shifts, only one outer beam is considered. Vibrations (dashed green lines) take place around an equilibrium position (thick green line). The curved shape is indirectly engendered by static deflections (proportions not to scale)

of rotational springs is justified by the facts that extremeties of the outer beam are attached to the overhangs. Intuitively, it can be foreseen that, although the overhangs can be considered as axially immovable ends, they should not act as ideal clamping supports. In actual practice, the outer beam should transfer energy to the overhangs through its attachement points during oscillations. Consequently, it is rather expected that the overhangs should slightly distort during oscillations of the outer beam (this is confirmed by FEA, as shown in Fig. 3.8(b)). In the literature, elastic rotational springs are often used to model such a flexibility [175, 176, 177].

Again, energy approaches can be exploited to conveniently handle the configuration of Fig. 3.6. Because the outer beam is terminated by rotational springs attached to pinned ends supports, it is conventional to assume a displacement function in the form of a sine

$$w(x) = D_s \sin\left(\frac{\pi x}{l}\right) \tag{3.11}$$

where D_s is the midspan deflection of the outer beam.

D_s is related to the force F applied upon the central steady beam, and can be estimated from the previous static analysis (see Fig.3.5)

$$D_s = w_3(l) - w_1(l/2). \tag{3.12}$$

Conceptually, it is however more convenient to consider that D_s is rather due to an unknown equivalent virtual force F_v (see Fig. 3.6). With an energy approach, a relationship between D_s and F_v can be derived. Considering that F_v is applied at the beam midspan, the potential energy stored by the beam is the sum of the following contributions

$$U_T = U_b + U_s + U_{rs}. \tag{3.13}$$

64

In Eq. (3.13) U_b is the bending energy of the beam

$$U_b = \frac{EI}{2} \int_0^l \left(\frac{d^2w}{dx^2}\right)^2 dx \tag{3.14}$$

U_s is the energy developed during the midplane stretching of the beam

$$U_s = \frac{EA}{8\,l} \left[\int_0^l \left(\frac{dw}{dx}\right)^2 dx\right]^2 \tag{3.15}$$

and U_{rs} is the energy stored by the two rotational springs of stiffness k_{r1}

$$U_{rs} = \frac{k_{r_1}}{2}\theta_0^2 + \frac{k_{r_1}}{2}\theta_l^2 \tag{3.16}$$

where θ_0 and θ_l are the slopes $\dfrac{dw}{dx}$ evaluated at $x = 0$ and $x = l$, respectively.

Considering that the work done by F_v is $W_1 = F_v\,w(l/2)$, the total potential energy function Φ_1 is

$$\Phi_1 = -F_v\,D_s + \left[\frac{\pi^2 k_{r_1}}{l^2} + \frac{Ebh^3\pi^4}{48l^3}\right]D_s^2 + \frac{Ebh\pi^4}{32l^3}D_s^4\,. \tag{3.17}$$

Minimizing Eq. (3.17) with respect to D_s yields a *cubic force-centered-deflection law*

$$F_v = k_1\,D_s + k_3\,D_s^3 \tag{3.18}$$

where

$$k_1 = \frac{Ebh^3\pi^4}{24l^3} + \frac{2k_{r_1}\pi^2}{l^2} \qquad \text{and} \qquad k_3 = \frac{Ebh\pi^4}{8l^3}\,. \tag{3.19}$$

In Eq. (3.19), k_1 and k_3 are linear and nonlinear spring constants, respectively.

As in [178], it can now be assumed that small deflections of the beam about a mean deflection D_s can be described approximately by a single stiffness value. An effective spring constant is found by deflecting the beam from its equilibrium position by an arbitrary amount Δ_d (see Fig. 3.6), so that

$$F_v = k_1\,(D_s + \Delta_d) + k_3\,(D_s + \Delta_d)^3. \tag{3.20}$$

Expanding Eq. (3.20) yields

$$F_v = k_1\,D_s + k_1\,\Delta_d + k_3\,D_s^3 + 3k_3\,D_s^2\Delta_d + 3k_3\,D_s\Delta_d^2 + k_3\,\Delta_d^3. \tag{3.21}$$

Considering that vibration amplitudes Δ_d are sufficienctly small, terms proportional to Δ_d^2 and Δ_d^3 in Eq. (3.21) can be neglected. Then, an equivalent stiffness of the outer beam may be approximated by

$$k_{eq} = \frac{dF_v}{d\Delta_d} \approx k_1 + 3\,k_3\,D_s^2. \tag{3.22}$$

As often in structures involving coupled beams, vibrating beams can be modeled to a first approximation as one degree of freedom oscillators (e.g., [179, 180]). If the single outer beam is assumed to oscillate as an undamped lumped-parameter system, its natural frequency is given by

$$f = \frac{1}{2\pi}\sqrt{\frac{k_{eq}}{m_{eq}}} \tag{3.23}$$

where m_{eq} is the equivalent mass of the beam.

At rest, $D_s = 0$ and the initial resonance frequency of the beam is solely proportional to the linear spring constant

$$f_0 = \frac{1}{2\pi}\sqrt{\frac{k_1}{m_{eq}}}. \tag{3.24}$$

Nevertheless, as the predeflection D_s increases, the quadratic term in Eq. (3.22) becomes more and more prominent. As a result, the resonance frequency of the beam will vary in accordance with the following relation

$$\frac{f}{f_0} \approx \left[1 + \frac{3\,k_3}{k_1}\,D_s^2\right]^{1/2}. \tag{3.25}$$

In Eq. (3.25), D_s is directly dependent upon the amount of force F applied to the central beam (see Eq. (3.12)). Consequently, one can estimate F by monitoring the variations of resonance frequency of the outer beams.

3.3 Discussion about the dimensions of the planar structure

In Chapter 2, a parametric analysis was conducted in order to maximize the performances of the resonant CC beam. Likewise, a similar optimization should be conducted for the planar structure. Here, a rigorous parametric analysis should investigate variations of dimensions for the set of parameters represented in Fig. 3.7. Nonetheless, trying to optimize the structure with the exclusive goal to achieve the best performance indices possible can lead to unrealistic dimensions. For instance, results can lead to a structure which in practice cannot be fabricated with the equipment and/or materials available. Hereafter is discussed how experimental constraints actually imposed severe restrictions for the selection of dimensions.

- Determining the width b_2 of the central beam

The first main constraint was directly related to the type of biological samples used during experiments. For preliminary tests, suspension cells (lobster eggs) with an approximate diameter of 500 μm were used (motivations that led to the choice of this
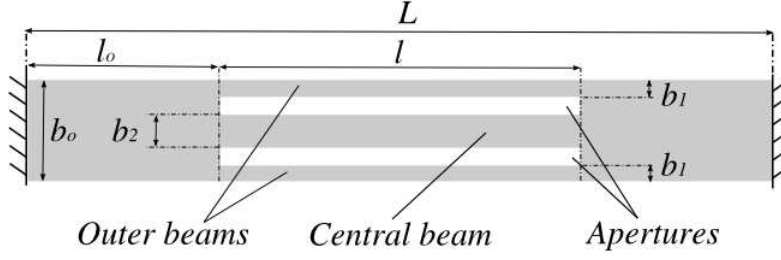
Figure 3.7: Top view of the planar resonant structure with dimensions that can be varied to impact the structure's performances. b_o and l_o are the width and the length of the overhangs, respectively. l is the length of the tree beams. b_1 and b_2 are the width of the outer beams and the central beam, respectively. The whole structure has a length L and constant thickness h (not represented).

specific type of samples are given in Chapter 4). Because no system capable of holding a cell (e.g., a microwell) is presently implemented, the positioning of suspended cells during experiments is greatly facilitated if the central beam has a width similar to the diameter of the cells. Consequently, a central beam with a width of 500 μm appeared to be ideal for a first prototype.

- Determining the width b_1 of the outer beams

In order to provide the well balanced vibration mode of Fig. 3.2(c), the two outer beams must have the same dimensions. Moreover, this specific mode mainly occurs if the width of the central beam b_2 is at least twice the width b_1 of the outer beams (i.e., $b_2 \geq 2b_1$). However, as it will be detailed in Chapter 4, laser sensors were used to monitor the vibrations of the outer beams during experiments. In this case, very narrow beams can lead to weak reflectivity and detection problems. For preliminary tests, outer beams with $b_1 = 250$ μm were hence favoured.

- Determining the thickness h of the structure

Trying to impact structure performances by varying the thickness h proved to be useless. Indeed, at the time of prototyping (see Chapter 4), only sheets of stainless steel with a thickness of 100 μm could be used for the fabrication of the prototype. In any event, it must be underlined that a prototype with a lower thickness would have been very delicate to manipulate. Because the prototype of Chapter 4 had to be manipulated with bare hands, a thickness of 100 μm proved to be ideal to avoid any warping of the structure.

- Determining the length l of the three beams

The length l was selected in order to ensure high performances of the oscillating outer beams. A high frequency was sought to obtain a high Q factor. Indeed, with a high Q

factor, small changes of frequency lead to large changes of the oscillation amplitude (see Fig. 2.6). Accordingly, a high Q factor can permit to easily detect small forces applied to the central beam. From Chapter 2, we realized that the shorter the beam the higher the resonance frequency. However, the planar structure behaves in a more complex way than a simple CC beam. In particular, although shorter beams indeed increase the frequency of the vibration mode, Fig. 3.8 shows that a significant alteration of the mode shape may occur. This demonstrates that the overhangs do definitely not act as ideal clamped-clamped end conditions. A distorted mode such as the one in Fig. 3.8(b) must be avoided at all costs for at least two reasons. First, because the outer beams in Fig. 3.8(b) twist during oscillations. This twisting can engender measurement instabilities with laser sensors. Second, vibrations can be transferred to the central beam. This can pose problems to maintain the position of the cells on the central beam. Moreover, these vibrations can provide unwanted mechanical stimuli to the cells. For a thickness $h = 100\mu$m and a width $b_1 = 250\mu$m, the length l of the outer beams (and hence the length of the central beam) was selected to be 12.5 mm. This value indeed represented a good trade-off for achieving a high resonance frequency while ensuring a proper vibration mode.

(a)   (b)
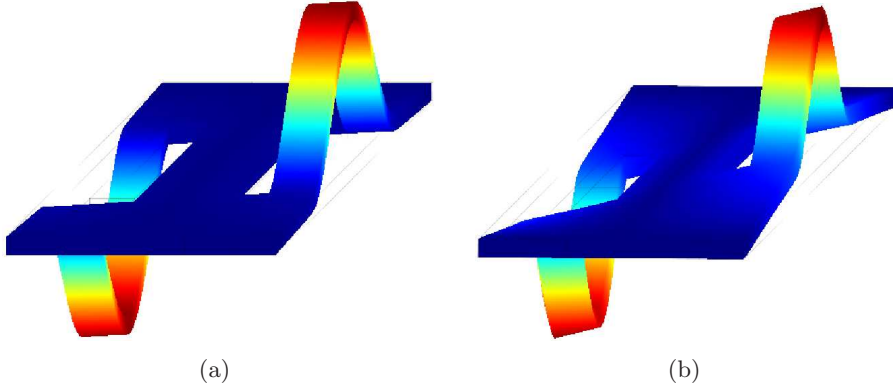
Figure 3.8: Images from FEA analysis showing two structures with the same dimensions. Only the length of the beams is different. With shorter outer beams, a significant distortion of the mode shape may occur. (a) Structure with outer beams 12.5 mm long; (b) The same structure with outer beams 8 mm long.

- Determining the width b_o of the overhangs

FEA actually shows that the width b_o of the overhangs should not be large. This is due to the fact that with larger overhangs, the attachment points that link the outer beams to the overhangs become softer. A first consequence is that the resonance frequency of the mode of interest decreases. This is not in favour of a better sensitivity. With softer attachment points, a distortion of the mode also occurs, even though it is less important than the one shown in Fig. 3.8(b). But again, vibrations that could be potentially transferred to the central beam should be absolutely avoided. For the fabrication of the prototype in Chapter 4, several FEA analysis have been conducted. As a

result, the best trade-off has been obtained for $b_o = 1.5$ mm. With this value, the attachment points are sufficiently rigid. In the meantime, the outer beams are sufficiently isolated from the central beam so that they cannot touch a large cell during oscillations.

- Determining the length l_o of the overhangs

With all other dimensions fixed, there is no real need to run numerous calculations or simulations to foresee that the planar structure becomes more and more compliant as the length of the overhangs increases. This may first appear as an advantage, because for a particular amount of force applied to the central beam, more deflection is imposed to the outers beams. Consequently, a higher amount of frequency change can be expected for the same amount of force applied. On the other hand, the structure becomes more fragile. If the structure must be manipulated by bare hands, warping can easily occur. Moreover, if the aspect ratio of the structure (L/h) is very high, fabrication of the structure may rapidly become delicate. Finally, the device becomes cumbersome. Therefore, the structure should not be designed to be as long as possible. A reasonable and convenient limit was found by fixing $l_o = l/2 = 6.25$ mm.

3.4   Static and dynamic behavior of the structure: numerical application

Dimensions for the fabrication of a first prototype were selected according to the aforementioned justifications. Numerical values for these dimensions (see list in Table 3.1) can now be used to compute the theory developed in Section 3.2. To validate the analytical approaches developed for predicting the static and dynamic behaviors of the structure, FEA was used as a reference tool. To run FEA, additional material properties were specified within COMSOL V4 multiphysics package. Since stainless steel has been utilized to manufacture the prototype of Chapter 4, a density of 8030 kg/m^3 and a Poisson's ratio of 0.29 were set during simulations.

3.4.1   Theoretical results: static deflection

The static deflection of the structure was first investigated. To consider the midplane stretching effect, COMSOL simulations were run in the nonlinear (i.e., large) deflection mode. COMSOL simulations were run for the entire structure. For a point force $F = 260$ mN applied at the half span of the central beam, Figure 3.9 shows that static behavior predicted the theory developed in Section 3.2.2 is in excellent agreement with the one predicted by COMSOL.

Several facts can be observed from Fig. 3.9. First, it is confirmed that the outer beam indeed deflects in a way very similar to a sine, as assumed in Section 3.2.3. Second, the deflection amplitude of the outer beam is smaller than the deflection amplitude of the central beam. This intuitive result is also confirmed by Fig. 3.10 which compares

Beams length (l)	12.5 mm
Outer Beams width (b_1)	0.25 mm
Central Beam width (b_2)	0.5 mm
Overhangs width (b_o)	1.5 mm
Overhangs length (l_o)	6.25 mm
Total length (L)	25 mm
Thickness (h)	0.1 mm
Young's modulus of stainless steel (E)	212 GPa

Table 3.1: Numerical values selected for prototype fabrication and theoretical predictions (see also Fig. 3.7)
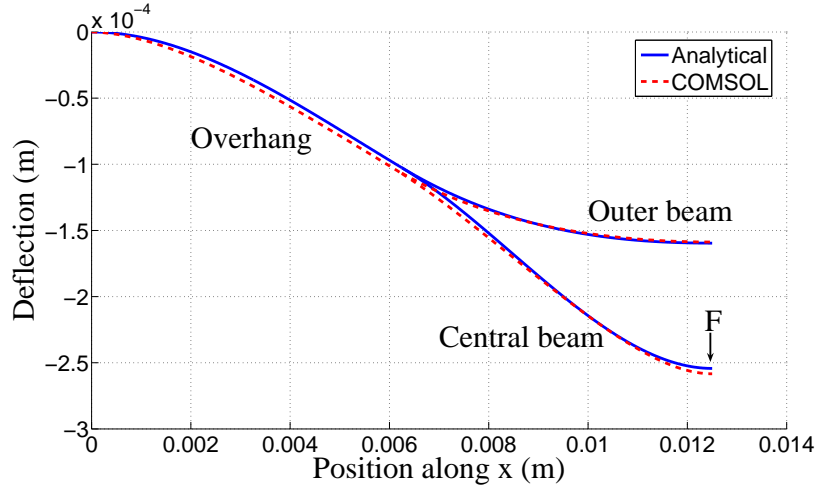
Figure 3.9: Deflection profile and deflection amplitude when a normal force $F = 260$ mN is applied at the half span of the central beam.

the deflection amplitude of both beams as a function of the force F applied. Again, Fig. 3.10 proves that analytical and FEA results are in accordance. It also clearly demonstrates that the stretching effect progressively dominates as the beams deflection increases. Thereby, for large deflection amplitudes, the structure is clearly stiffer.

3.4.2 Theoretical results: variations of resonance frequency

Once the static deflection is known, the amount of frequency change engendered can be estimated. For COMSOL predictions, a prestressed modal analysis was run. This consisted of the previous static analysis in which the nonlinear deflection of the structure was obtained. This was followed by a subsequent modal analysis, which calculated the new resonant frequency of the strained structure. With the analytical model developed,
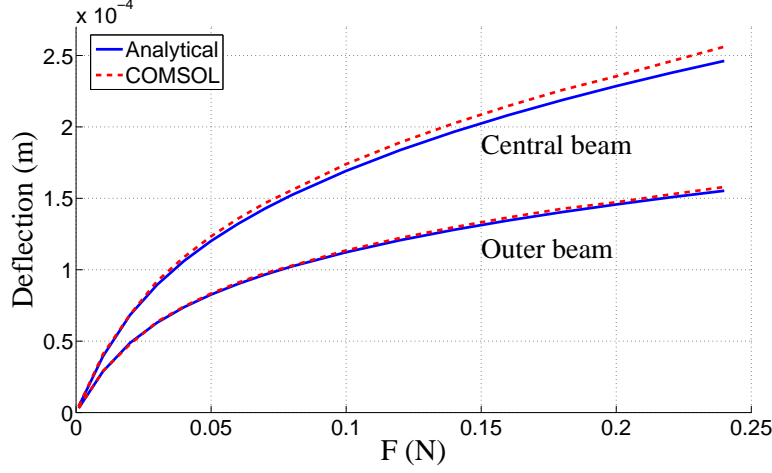
Figure 3.10: Half span deflections of the central beam and one outer beam as a function of the force F applied to the central beam. Due to symmetry, the second outer beam deflects excactly in the same manner.

the amount of frequency change can be estimated with Eq. (3.25). Nevertheless, to compute Eq. (3.25), a numerical value must be attributed to the rotational stiffness k_{r1}. An order of magnitude was found in [181] where a formula is given to estimate the rotational spring constant of anchors for a CC beam

$$k_{r1} = \frac{16\,E\,I_3}{l} \tag{3.26}$$

where $I_3 = b_1 h^3/12$ is the moment of intertia of the outer beam drawn in Fig. 3.6. For a structure whose dimensions are given in Table 3.1, Eq. (3.26) gives $k_{r1} \approx 5.6 \times 10^{-3}$ Nm/rd. This numerical value provides an order of magnitude for k_{r1}. However, as previously revealed, the outer beams do not excactly behave as ideal CC beams during oscillations. Therefore, the value of k_{r1} was adapted by fitting curves with COMSOL predictions. With $k_{r1} = 3.45 \times 10^{-3}$ Nm/rd very satisfactory results were obtained, as seen in Fig. 3.11.

COMSOL simulations were run for the whole structure so that the specific vibration mode where the two outer beams oscillate in antiphase could be considered. By way of comparison, the analytical approach of Section 3.2.3 has only considered one outer beam with approximate boundary conditions. Notwithstanding these simplifications, Fig. 3.11 proves the applicability of the analytical model developed. When analysing Fig. 3.11, a quasi linear region is observed if the force applied to the central beam exceed 100 mN. In particular, the inset shows that for small variations of force F applied around the point P, a linear force sensitivity of 2.91 Hz/mN is predicted. In the mean time, it is worth noting that most digital oscilloscopes can today at least provide frequency measurement with an accuracy of 0.01 Hz. This means that, in theory, a minimum force of about
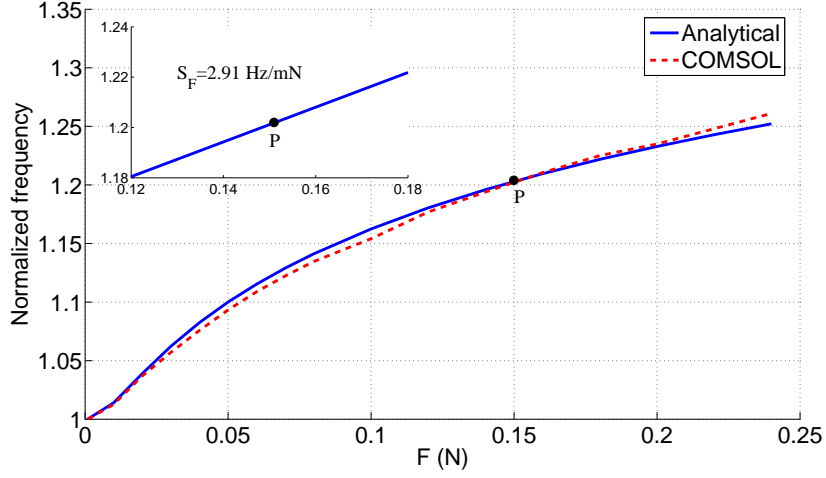
Figure 3.11: Evolution of the resonance frequency of the outer beams when a vertical force F is applied upon the half span of the central beam.

3.4 μN could be resolved by the structure. An even higher force resolution could be obtained with a frequency counter providing higher precision.
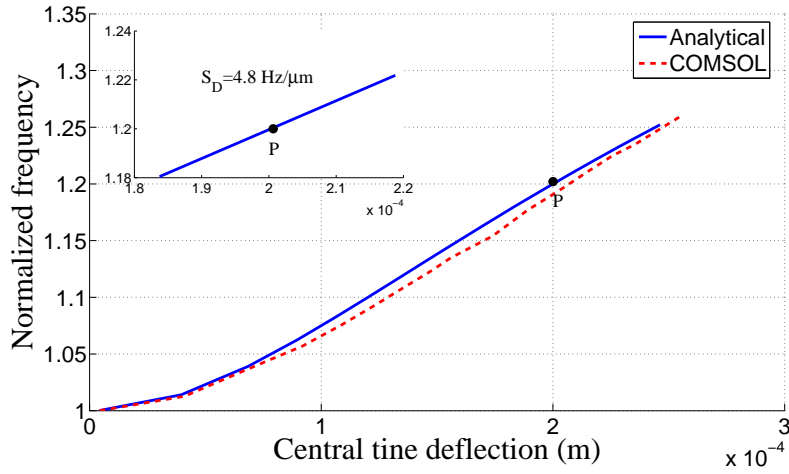
Figure 3.12: Evolution of the resonance frequency of the outer beams when a vertical displacement is imposed upon the half span of the central beam.

Alternatively, and because displacements of the central beam can also be predicted with respect to the force F applied, the amount of frequency change can also be estimated as a function of a displacement imposed to the central beam. As seen in Fig. 3.12, a linear displacement sensitivity of 4.8 Hz/μm is expected. If the frequency can be measure with an accuracy of 0.01 Hz, a minimum displacement of $\sim$2 nm can theoretically

be detected by the structure.

3.5 Conclusion

This chapter has introduced a novel planar structure that constitutes the heart of this thesis work. This planar structure is intended to act as a force sensitive cell substrate for measuring the Young's modulus of living cells. It provides a steady area where suspended and adherent cells can be placed. Because the steady area is connected to two adjacent beam resonators, the force applied to the cells can be estimated by monitoring the frequency changes of the beam resonators. This is an interesting feature considering the fact that, as outlined in Chapter 1, most MEMS dedicated to cell mechanics can exclusively deal with only one type of cells. Moreover, the steady area could be equipped with an open microfluidic channel. Thereby, cells could be cultured in growth medium. In the mean time, forces applied upon cells can be sensed with the beam resonators without the need to plunge them into liquids. This provides a solution to problems identified in Chapter 2 that are inherent to most resonators dealing with biological samples in liquids. Furthermore, the structure has been designed to be MEMS compatible in the sense that it can be duplicated via microfabrication processes for matrix configurations. An extensive theoretical analysis has been conducted to investigate the static and dynamic behaviors of the structure. When the central beam is bent, a quasi linear displacement sensitivity $\sim$4.8 Hz/μm has been predicted. For measuring forces on cells in order to extract their Young's modulus, the force sensitivity expected is about 3 Hz/mN. Since most digital oscilloscope can today at least measure frequencies with an accuracy of 0.01 Hz, this means that the structure can in theory detect a displacement of about 2 nm, and resolve a minimum force of 3.4 μN. To confirm these predictions, Chapter 4 next reports the fabrication and the experimental characterization of a first prototype.

Chapter 4

Experimental validation and first investigations conducted on biological samples

From Chapter 2, it is clear that measuring forces with a simple beam resonator in a liquid environment is challenging. This drawback usually prevents the use of beam resonators for estimating the Young's modulus of living cells. To bridge this gap, Chapter 3 has introduced a new force sensitive structure constituted of two narrow outer beams and a wider central beam. It exploits a specific vibration mode where the two outer beams oscillate in antiphase whereas the central beam remains immovable. A key feature of the structure is that the central steady beam has the potential to be used for the implementation of a microfluidic system for maintaining cells in culture medium. Meanwhile, the outer beams can be used to measure vertical forces applied to individual cells. The fact that the resonant beams can measure forces without the need to plunge them in the liquid is another strength of the structure. In Chapter 3, the static and dynamic behaviors of the structure have been theoretically analysed. In this Chapter, experiments are first conducted in order to validate the performances predicted.

To that purpose, Section 4.1 reports the fabrication of a first prototype as well as the experimental arrangement used for its characterization. The section also details the implementation of an optical fiber displacement probe specifically developed for measuring the resonance frequency of the outer beams. Then, the static and dynamic behaviors of the prototype are experimentally explored in Section 4.2. Each experimental result is confronted to theoretical predictions. In a second part, the prototype is used to conduct first investigations on biological samples. In Section 4.3, the prototype is associated with an indenter. The whole system is used to compress a suspension cell. An indirect method that could be easily automated is also presented in order to rapidly extract a first estimation of the Young's modulus of the cell. Finally, Section 4.4 concludes the chapter.

4.1 Experimental arrangement

4.1.1 Overview

To validate the theoretical analysis developed in Chapter 3, a first prototype of the planar structure (see Fig. 4.1) was fabricated in accordance with dimensions listed in Table 3.1. As a reminder, these dimensions were selected in order to deal with suspension cells with a diameter ranging from 100 to 500 μm. For preliminary tests, such large cells indeed appeared ideal since it is relatively easy to localize them, even with bare eyes. They are also inherently more robust to manual manipulation than smaller cells. Considering the length of this prototype (25 mm), microfabrication processes were not required for its fabrication. Although the planar structure has been designed to be MEMS compatible, precision wire cut electric discharge machining (EDM) proved to be an efficient technique for rapid and inexpensive prototyping.
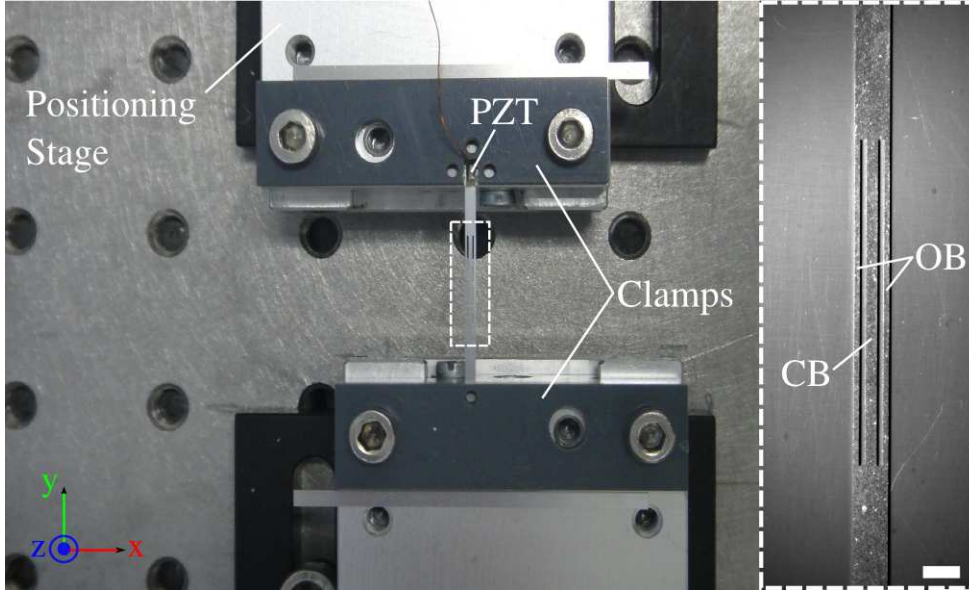
Figure 4.1: Top view of the prototype and experimental arrangement used during experiments. The planar structure fabricated is hold between two clamps tightened with screws. A manual positioning stage can translate one of the clamps along the y direction. The PZT element is used to activate the resonance mode of interest. The right inset provides a microscope view of the area indicated by dashed lines. For conciseness, CB and OB stands for central beam and outer beams, respectively. The white scale bar equals 1.5 mm.

The selection of the material to be used for the fabrication of the prototype was based on three main criteria. First, wire cut EDM had to be capable of machining the material selected with a high precision. Second, the material had to be biocompatible

75

since the structure is intended to be directly in contact with living cells. Third, the material preferably had to be reflective so that optical sensors could be used during experiments (see Section 4.1.2). Several stainless steel alloys gather up all these features. The prototype was hence cut from a single sheet of stainless steel whose thickness was 100 μm. This thickness proved to be convenient to avoid any risk of warping when the prototype had to manipulated with bare hands.

To activate the antisymmetrical resonance mode of interest (see Fig. 3.3), mechanical excitation was provided by a 3 mm long, 2 mm wide and 200 μm thick piezoelectric (PZT) element (Physik Instrumente PIC151). This PZT element was bonded onto the prototype with conductive paste and driven by an AC signal with a function generator (Agilent 33120A) connected to a laboratory power amplifier (Newtons4th LPA400).

During experiments, the prototype was suspended between two clamps. One of the clamps was fixed to a manual micropositioning stage that allowed horizontal translations along the y direction (see Fig. 4.1). To ensure a firm attachment of the prototype and to avoid slipping, the clamps were tightened with screws. It is also worth underlining that the whole setup was mounted on a pneumatic antivibration isolation table to minimize the presence of external disturbances.

4.1.2 Implementation of an optical fiber displacement probe

To extract the Young's modulus of a cell, one must know the force that deforms the cell. Chapter 3 has demonstrated that if a vertical force is applied to the central beam of the structure, the force applied should provoke frequency shifts. Hence, to measure forces with the planar structure, the resonance frequency of the outer beams must be measured. A large variety of techniques can be employed for such a measure.

The integration of strain gauges made of sensitive films was first investigated. Such strain gauges indeed enable straightforward detection of resonance vibrations. They can also be easily deposited and patterned at the surface of microfabricated structures. Besides, a PZT element has been already favored to provide excitation to the prototype. Reciprocally, PZT sensing elements could have been bonded near the attachment points of the outer beams to convert mechanical vibrations into electrical signals. Because stress is maximum near attachment points, this location would have maximized the mechanical to electrical coupling. However, to test this configuration with the prototype of Fig. 4.1, the only available option was to bond the PZT elements by bare hands. With such a manual bonding, neither the amount of conductive paste deposited nor the alignment of the PZT elements could have been precisely controlled. Accordingly, the risk of altering the structure symmetry and distorting the vibration mode of Fig. 3.3 was high.

To avoid any alteration of the balanced vibration mode exploited, a non-contact based measurement technique was favoured. Among other techniques (e.g., see reviews

[182, 183]), optical fibers rapidly appeared as excellent candidates. Indeed, optical fibers can provide exquisite displacement resolutions with high bandwidth. They are also inherently very compact and could be used for future MEMS version of the planar structure. For instance, optical fibers with a diameter of 125 μm can be easily found. Moreover, dense networks of multiplexed optical fibers are extensively used in numerous applications (e.g., in telecommunications). Optical fibers are thus inherently adapted for measuring the frequency of multiple structures in a matrix-like configuration.

When associated with interferometric techniques, optical fibers can measure displacements up to several millimeters with a resolution of 10 nm (e.g., fiber Fabry-Perot interferometers [184, 185, 186]). Despites appealing advantages, interferometers fiber probes involve complex demodulation techniques such as fringes counting for extracting the information of interest. They also involve expensive optical equipment (e.g., laser sources).

Alternatively, fiber displacement sensing heads based on variations of light intensity can achieve similar performances [187]. Compared to interferometric methods, their exploitation can be simpler. In this work, such a configuration was preferred. As illustrated in Fig. 4.2, the implemented sensing head is made of two optical fibers. One of the fiber is used as a transmitter. This transmitting fiber is connected to a light source and guides the light toward a reflective target (i.e., in our case, the surface of the outer beams). The second fiber is used as a receiver and collects the light reflected by the target. Theoretically, it has been shown that the amount of optical power returning to the receiving fiber P_r depends on the gap g between the end of the head and the mirroring target [188]

$$\frac{P_r(g)}{P_t} = \frac{2}{\zeta^2} \ \exp\left(-\frac{8}{\zeta^2}\right) \tag{4.1}$$

where

$$\zeta = 1 + 2g/z_a. \tag{4.2}$$

In Eqs. (4.1, 4.2), P_t is the optical power exiting the transmitting fiber and z_a is the light asymptotic cone apex (see Fig. 4.2).

During experiments, the light source used was a vertical cavity surface emitting laser (VCSEL) diode (Honeywell HFE4080-321-XBA). This diode was originally intended for high-speed data communications. Compared to most commercial laser sources, the external case of the HFE4080-321 is only 12.7 mm long. With a wavelength centered around 850 nm, the light emitted from this diode proved to be insensitive to potential disturbances originating from the ambient light. This preserved the quality of the signal of interest during measurements. As recommended by the manufacturer, the diode was supplied with a regulated forward current of 11 mA to guarantee stable and safe operation without temperature control. The VCSEL diode was connected to the transmitting fiber via a standard ST-LP fiber connector. With a forward current limited to

77
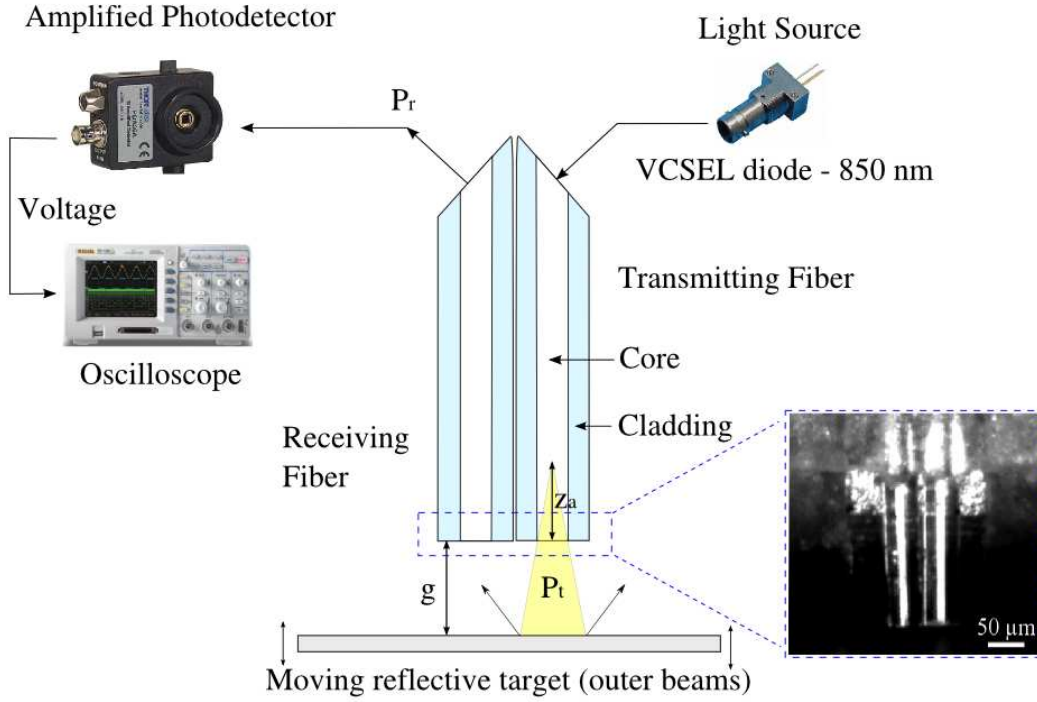
Figure 4.2: Illustration of the double-fiber displacement sensor used to measure the oscillation amplitude of the outer beams during experiments. The inset on the right corner shows a magnified view of the two fibers used during experiments.

11 mA, the optical power exiting the transmitting fiber was 800 μW (measured with a powermeter Thorlabs PM100).

For the two optical fibers, step index multimode fibers with a cladding diameter of 125 μm and a numerical aperture of 0.22 were used (Thorlabs AFS50/125Y). Theoretically, performances of the sensor head can be modified by using two fibers with a different core and cladding diameters [189]. In experimental conditions, however, such a configuration proves to be very unpractical for the alignment of the fibers, especially considering the small size of the fibers adopted here. Therefore, the possibility to implement fibers with different geometries was not considered. For optimal performances, fibers extremities were cleaved (i.e., fibers were cut perpendicularly to their longitudinal axis). This process ensured perfectly flat endfaces. It is worth noticing that cleaving the fibers extremities partly removed their cladding and reduced their diameter to $\sim$50 μm. Such dimensions offered an even more compact sensing head, with high capabilities of integration.

To be tested with the prototype of Fig. 4.1, fibers were aligned manually with the help of an optical microscope (see inset in Fig. 4.2). Aligning the fibers with bare hands proved to be a labor intensive and time-consuming operation. In effect, any offset in

the vertical alignment, the lateral separation or the parallelism of the fibers could affect the sensor's performances [190, 191, 192, 193]. The two fibers were then attached to a rigid plastic support simply by using adhesive tape. In spite of its apparent simplicity, this method proved to be sufficient for preliminary tests with the prototype. It is worth mentioning that possible temperature or humidity fluctuations did not significantly impact the tension of the adhesive tape. The latter remained constant over time and did not alter the fiber alignment.

At the receiving side, the fiber was connected via a FC/PC fiber connector to a photodetector equipped with a photodiode and a high gain transimpedance amplifier (Thorlabs PDA-10CF). Although the PDA-10CF was optimized for detecting light centered around 1550 nm, it provided a sufficient responsivity of 0.2 A/W at 850 nm. With this photodetector, any variations of the gap g were converted into electrical signals proportional to the modulation of light intensity entering the receiving fiber.

The double-fiber sensor shown in Fig. 4.2 was then tested and characterized on the stainless steel of the prototype. The vertical gap g was varied from 0 to 5 mm with a micropositioning stage (Physik Instrumente M112-1DG). Normalized variations of light intensity captured by the receiving fiber are plotted in Fig. 4.3. Variations predicted by Eq. (4.1) for $z_a = 371$ μm are also given for comparison. This value of z_a was not computed from the a priori knowledge of the fibers parameters. In practice, these parameters can indeed fluctuate according to the surface quality of the fibers' ends and can be difficult to evaluate. Instead, it was more practical to determine the value of z_a directly from the experimental curve.

From Fig. 4.3, it can be observed that the optical power detected by the receiving fiber monotonically increases for a maximum distance $g \approx 500$ μm. At larger distances, the optical power decays gradually, approximately like $1/g^2$. Good agreement is obtained between theoretical predictions and experimental measures. This proves that, despite the manual alignment of the two fibers, the displacement sensor worked properly.

In the subsequent experiments, the linear region offered by the fiber probe around the point P (see Fig. 4.3) was exploited to measure both static and dynamic displacements of the structure. During operation, the only real restriction encountered was the sensitivity of the technique to the reflectivity of the target surface. In practical terms, this means that the sensitivity of the fiber sensor could slightly vary depending on the area of the prototype targeted. Sometimes, a tedious recalibration of the sensor was required. Compensation techniques however exist and could be implemented in the future (e.g., [194]). Moreover, it is worth mentioning that with the use of an additional optical coupler, the same sensing principle could be used with a single optical fiber [195, 196].
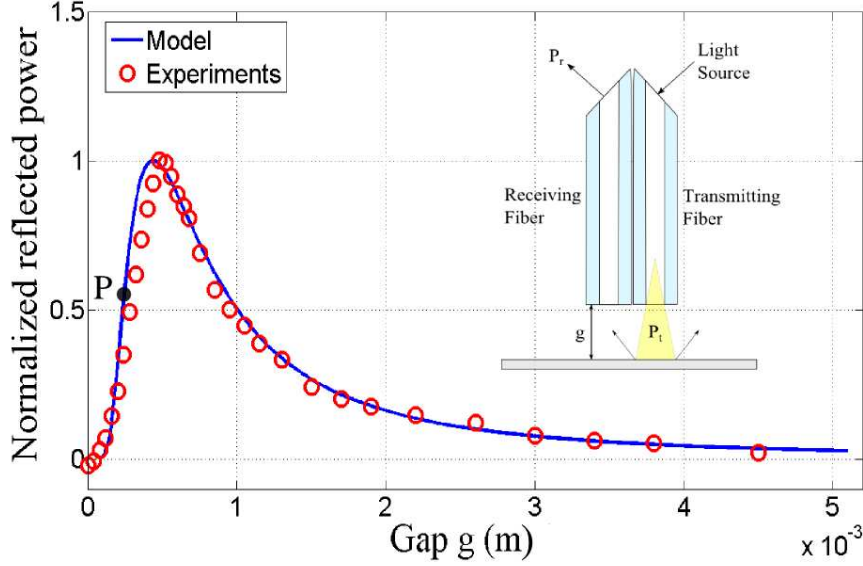
Figure 4.3: Normalized variations of light intensity captured by the receiving fiber for variations of the gap g up to 5 mm. Solid line represents variations predicted by Eq. (4.1) with $z_a = 371$ μm. Circles corresponds to experimental measurements.

4.2 Comparison between theory and experiments

4.2.1 Evaluation of static deflections

Experiments were first carried out to investigate the static deflection of the prototype. The gap between the optical fiber displacement probe and the prototype's surface was set to $\sim$220 μm. This height was set in order to exploit the steep slope offered by the fiber probe around the point P (see Fig. 4.3). This region provided a displacement sensitivity about 9 mV/μm when the gain of the photodetector was set to 50 dB. The bandwidth of the photodetector was 90 KHz for this gain. During experiments, voltage variations could be measured with an accuracy of 0.1 mV. This provided a displacement resolution of about 10 nm. A commercial laser sensor providing a resolution of 0.01 μm (Keyence LK - G10) was also used as a reference to verify displacement measured with the fiber probe.

To bend the structure, an indenter terminated by a metal bead with an approximate diameter of 500 μm was used. The stiffness of the metal bead was much higher than the stiffness of the structure. From now on, it is important to note that this indenter was only controlled in position. Indeed, no appropriate force sensor could be used in conjunction with the experimental bench arranged. As a result, the force F applied to the central beam could not be directly controlled during experiments. In a few paragraphs, however, this indenter will be characterized so that force information can be retrieve

from displacements (see Section 4.2.2.5). The reader could hence legitimately wonder why the author here mentions that no force information was available. The problem is that the characterization of the indenter logically led to a linear force-displacement relationship (see Fig. 4.9). If this relationship can be safely used for small displacements of the indenter, it cannot be used anymore if large displacements are imposed to the structure. Thereby, several nonlinear phenomena that will be observed and discussed in the following sections would not have been revealed.

To control the position of the indenter, a micropositioning stage equipped with a position encoder and providing a minimum incremental motion of 50 nm was utilized (Physik Instrumente M112-1DG). Considering the small space available, the indenter had to be placed beneath the prototype, so that the indenter was translated along the z direction (see Fig. 4.1). To measure deflection of the structure, the optical fiber probe (or alternatively the laser sensor) was positioned above the structure.

Without a force sensor that could serve as a reference, Fig. 3.10 could not be directly retrieved. Comparison with theory could all the same be made by following the subsequent steps. The indenter was translated in the z direction so that the metal bead entered in contact with the central beam. Incremental motions of 10 μm were then imposed to the structure. Hence, deflection amplitudes of the central beam were known. In the mean time, corresponding deflections of the outer beams were measured with the optical fiber probe or the laser sensor. Considering the prototype symmetry, data were acquired solely for one outer beam. The difference of deflection amplitudes between the central beam and the outer beam Δ_d (see inset in Fig. 4.4) could then be calculated. This difference is plotted in Fig. 4.4 (circles and dashed line). Likewise, by subtracting the two solid curves of Fig. 3.10, Δ_d could also be extracted from theoretical predictions (solid line).

When compared to experimental results, the deflection of the outer beams predicted by theory is overestimated about 12% when the deflection of the central beam is above 30 μm. Uncertainties related to the fabrication process or the clamping of the prototype could explain this slight estimation error. The latter is however more likely due to numerical values used for calculations. For instance, values of Young's modulus and Poisson's ratio selected for calculations in Chapter 3 were extrapolated from material databases that provided typical values for various stainless steel alloys. But these values were not experimentally checked. In any event, theoretical and experimental results have very similar trends. This demonstrates that the prototype deflected as expected.

4.2.2   Evaluation of dynamic performances

4.2.2.1   Resonance frequency of the antisymmetric vibration mode

The dynamic behavior of the prototype was then explored. In a first step, no force was applied to the central beam. To actuate the prototype, the PZT element was driven
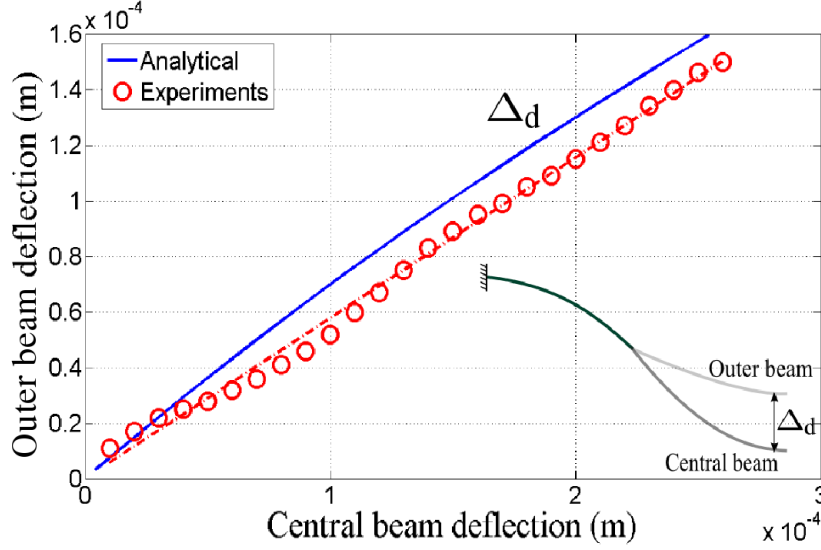
Figure 4.4: Difference of static deflection between the central and the outer beams (see Δ_d in inset). Solid line is plotted thanks to the curves from Fig. 3.10. Circles are experimental data (here obtained from the commercial laser sensor) and dashed line is a fitting curve.

with a sinusoidal voltage. The peak-peak amplitude of this sine signal was ∼9V at the exit of the power amplifier. The excitation frequency was then swept with the function generator in order to find the resonance modes of the prototype. As illustrated by Fig. 4.5(a), the antisymmetrical mode of interest where the two outer beams oscillate in antiphase was found at 3180 Hz.

By way of comparison, it is interesting to notice that COMSOL simulations predicted the occurrence of this mode at 3015 Hz in vacuum. It may seem a bit counterintuitive to find a higher resonance frequency for the real prototype oscillating in air. This can actually be simply explained by the clamping arrangement used during experiments. The prototype's anchors were indeed hold between clamps tightened with several screws. However, it was very delicate to obtain a homogeneous pressure over the entire surface of the prototype's anchors. In true fact, the resonance frequency of the prototype proved to be very sensitive to this setting.

4.2.2.2 Vibrations at the central beam

When the PZT element was driven with a voltage supply of 9 V, the peak-peak oscillation amplitude of the outer beams was 22 μm. During oscillations of the outer beams, a lot of attention was paid to check if potential vibrations were transferred to the central beam. As a matter of fact, they were very limited. As shown in Fig. 4.5(b), they never exceeded 500 nm, that is to say 2% of the oscillation amplitude of the outer beams. This
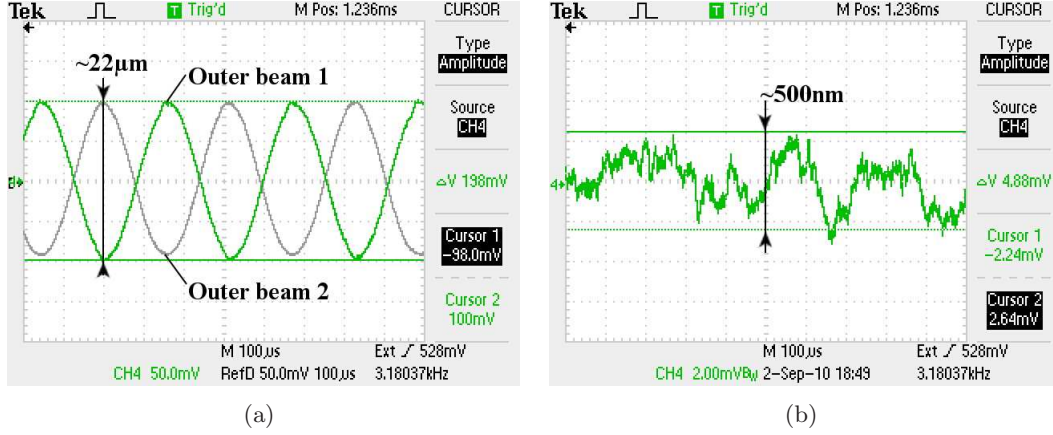
Figure 4.5: Oscilloscope screenshots showing: (a) The two outer beams oscillating in antiphase when the structure is driven at 3180 Hz; (b) Vibrations measured at the half span of the central beam with no force applied.

proves that the antisymmetrical mode obtained during experiments was well balanced. It is important to note that these vibrations could be even more attenuated simply by reducing the oscillation amplitude of the outer beams (i.e., by decreasing the voltage supply of the PZT element). Furthermore, these vibrations actually disappeared when the indenter was used to bend the central beam. Indeed, a significant stabilizing effect occurred each time the indenter entered in contact with the central beam.

4.2.2.3 Quality factor

As discussed in Chapter 2, the quality factor (Q factor) is a parameter of vital relevance that must be maximized for every resonant structure. The Q factor of the prototype could be experimentally evaluated by exploring the frequency response of the antisymmetrical mode. To that purpose, the frequency of the sine voltage supplying the PZT element was slightly swept around 3180 Hz. In ambient conditions, and with no force applied to the central beam, a pronounced resonance peak was observed (see Fig. 4.6).

From this resonance peak, the Q factor can be extracted by using [153]

$$Q = \frac{f}{\Delta_f} \tag{4.3}$$

where the frequency f corresponds to the maximum vibration amplitude a_m, whereas Δ_f is the difference between frequencies f_1 and f_2. Frequencies f_1 and f_2 correspond to vibration amplitudes 3 dB lower than a_m.

Applying Eq. (4.3) with Fig. 4.6 yields a Q factor of about 700. By comparison, calculations made in Chapter 2 for a CC beam with the same dimensions predicted a Q factor of 2474 in air (see Section 2.3.3). Even though the outer beams of the prototype rather oscillate as hinged-hinged beams (see Section 3.2.3), the Q factor found from
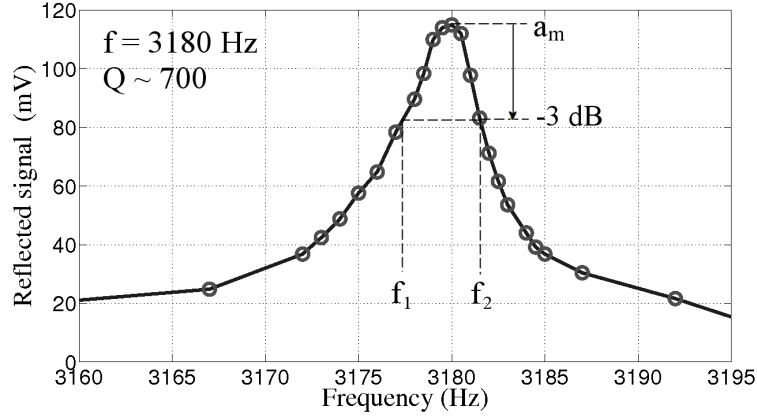
Figure 4.6: Experimental frequency response for the prototype of Fig. 4.1 driven around 3180 Hz.

Fig. 4.6 is more than three times lower. This corroborates the fact that, somehow, a substantial amount of energy is lost. This energy loss is most likely due to the overhangs that act as elastic end supports. One, however, must put this remark into perspective. For instance, a Q factor of 800 was reported for a CC beam in [197]. But in this reference, the authors operated the CC beam in vacuum. Therefore, obtaining a Q factor of 700 in air already constitutes an excellent achievement. Furthermore, one must remain conscious of the fact that Q factors of most cantilevers that are plunged into liquids for biological studies do not exceed 20 [198].

4.2.2.4 Frequency variations induced by large displacements

Oscillations of the outer beams were then monitored while the central beam was bent. Vertical translation steps along the z direction (see Fig. 4.1) were successively applied to the central beam with the indenter. For exploring the entire dynamics of the prototype, vertical steps of 10 μm were applied. Each incremental motion of the indenter caused the oscillation amplitude of the outer beams to suddenly drop. This amplitude drop corresponded to a frequency shift. However, with a step magnitude of 10 μm, the amplitude drop was significant and the signal measured with the optical fiber probe was often lost. To retrieve the frequency shift engendered, the frequency of the sine signal sent to the PZT element driving the prototype was modified with the function generator. The frequency was swept until a new maximum oscillation amplitude was found. The corresponding frequency was then noted and compared to the initial frequency. This procedure was iterated 25 times. For a total displacement of the indenter of 250 μm, the oscillation frequency of the outer beams evolved as shown in Fig. 4.7.

Interesting conclusions can be drawn from the analysis of Fig. 4.7. Compared to frequency variations predicted by theory, a more complex behavior is observed during experiments. From theoretical results, only a monotonically increase of the outer beams

84
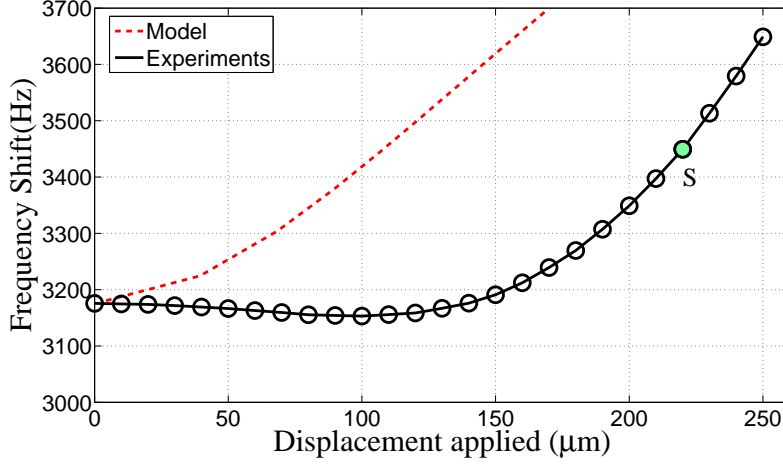
Figure 4.7: Frequency variations measured for a normal displacement applied to the half span of the central beam. Circles and solid line correspond to experimental data. Dashed line represents variations predicted by theory of Chapter 3 for the same initial frequency (corresponds to Fig. 3.12).

frequency was expected (see dashed line). Experimentally, it is actually observed that for small deflections of the central beam (i.e., deflections lower than 100 μm), the frequency of the outer beams slightly decreases. Such a behavior has actually been reported for buckled and deflected beams subjected to axial loads [199, 200, 201, 202, 203, 204]. This would mean that, somehow, the vertical displacement (or force) applied to the central beam is partly converted into weak axial force components that are transferred to the outer beams. From this hypothesis, one can try to give an explanation regarding the frequency shift experimentally measured.

As long as the deflection applied to the central beam is small (i.e., the displacement imposed to the central beam in Fig. 4.7 is lower than 100 μm), the curvature of the outer beams is negligible. This situation is represented in Fig. 4.8 (a). At this stage, axial forces seem to dominate. Because the resonance frequency decreases, it can be supposed that these axial forces are inherently compressive. But when the deflection of the central beam reaches 100 μm, the deflection of the outer beams is about 60 μm (this can been seen from Fig. 4.4). At this point, the curvature of the outer beams becomes significant (see Fig. 4.8 (b)) so that the midplane stretching effects begins to compensate the compressive axial forces. As the curvature of the outer beams continues to increase, the stretching effect clearly dominates and the resonance frequency of the outer beams steeply increases.

Due to the fact that no decreasing of the resonance frequency was predicted by theory, a significant bias is observed when compared to experimental measures. Nevertheless, the decreasing of the resonance frequency measured experimentally finally
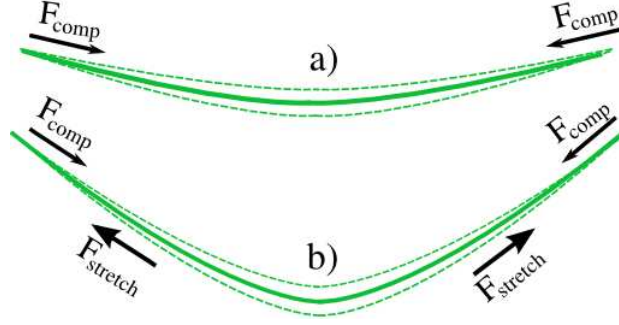
Figure 4.8: Illustration of an outer beam for explaining the experimental curve of Fig. 4.7. a) For small deflection of the central beam (<100 μm), the curvature of the outer beam (bold line) is negligible. During oscillations (dashed lines), compressive forces lower the frequency of the beam. b) For large deflection of the central beam (>100 μm), the induced deformation of the outer beam becomes significant. Stretching forces likely appear and progressively increase the resonance frequency of the outer beam. Proportions are greatly exaggerated for illustration purposes.

appears as a transition period. Indeed, a much steeper slope is provided at large deflections. In particular, it is very interesting to note that the curve in Fig. 4.7 offers a linear displacement sensitivity 5.75 Hz/μm around the point S. This displacement sensitivity is actually $\sim$17% better than the one expected initially by theory (4.8 Hz/μm).

4.2.2.5   Frequency variations induced by small forces

From the analysis of Fig. 4.7, it is now clear that the prototype provides a much better sensitivity when the central beam is largely bent. Because displacement sensitivity and force sensitivity curves are finally intimately correlated (see Fig. 3.11 and Fig. 3.12), the same behavior should still hold when thinking in terms of force sensitivity.

Hence, to exploit higher linear sensitivities, the transition period that takes place during small deflections of the central beam was suppressed by maintaining the prototype permanently deflected. This was possible since clamps were attached to manual micropositioning stages. As previously, the indenter was first used to deflect the central beam. A deflection of 220 μm was imposed to exploit the region around the point S seen in Fig. 4.7. Then, one of the manual micropositioning stages was translated until the prototype remained constantly curved at this position (i.e., even when the indenter was removed). Obviously, this axial translation compressed the whole structure. As a result, the initial resonance of the antisymmetrical vibration mode decreased from 3180 Hz to 3080 Hz. Nevertheless, no significant impact of this bias on the dynamic behavior of the prototype was noticed.

Unlike in Section 4.2.1, the amount of force generated by the indenter can now be estimated by characterizing the indenter for small displacement intervals. This be-
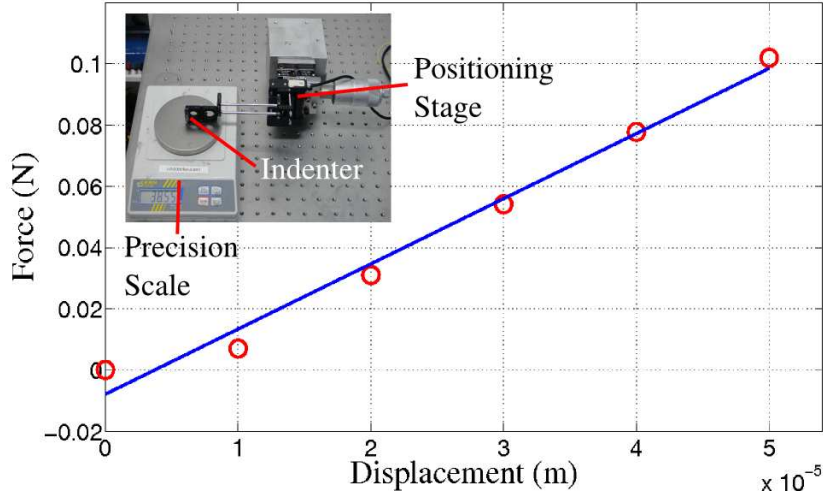
Figure 4.9: Experimental characterization of the force generated by the indenter. For small displacements, the force was determined from measurements made with a precision scale (see inset). Circles correspond to experimental data. Solid line is a fitting curve.

comes possible only because the analysis is now exclusively restricted to the linear region around the point S. For characterizing the indenter, the latter was pressed against a precision scale providing a mass resolution of 0.01 g (Kern 430-33). Five translation steps of 10 μm were applied on the precision scale. A linear relationship between the force generated by the indenter with respect to its displacement was found (see Fig. 4.9).

Then, frequency variations with respect to the force generated by the indenter were measured. Since the prototype was maintained predeflected, only a linear increase of the frequency was observed, as expected. This linear increase corresponds to a force sensitivity of 2.56 Hz/mN. Theoretically, a force sensitivity of 2.91 Hz/mN was predicted. Although the theoretical analysis of Chapter 3 has not initially considered a predeflection of the whole structure, the force sensitivity is only ∼12% lower than expected.

4.3 Measuring the elastic properties of supersoft materials

Previous sections have validated the static and dynamic behaviors of the prototype. It is worth noticing that, so far, the rigid bead of the indenter always entered directly in contact with the central beam. In this section, the possibility to use the prototype for biological applications is finally demonstrated by considering the presence of a living cell.

If one imagines to replace the metal bead of the indenter by a spherical suspension cell, the indenter can be used as an external actuator to deform the cell. With the indenter placed beneath the slightly predeflected prototype, the cell can be gen-
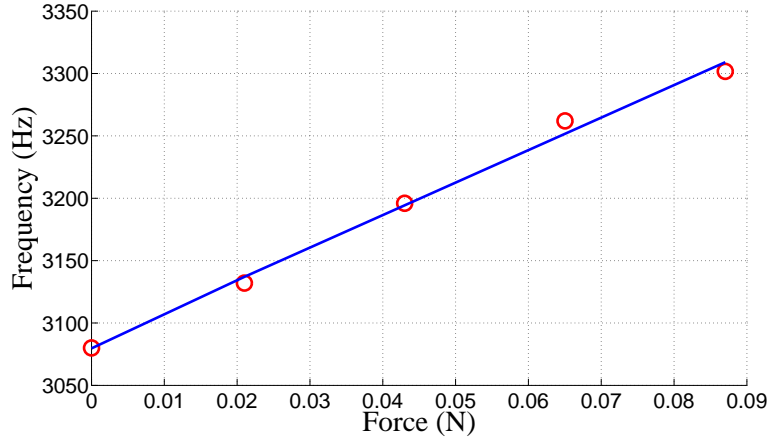
Figure 4.10: Frequency variations for a force applied to the half span of the central beam with the indenter. By translating one of the clamps, the whole prototype was slightly curved so that only the steepest linear sensitivity offered by the prototype was exploited. Circles correspond to experimental data. Solid line is a fitting curve.

tly pressed upon the central beam if the indenter is translated upwards (along the z axis, see Fig. 4.1). Such a configuration is very similar to the case of a cell compressed between two flat surfaces. In this case, the force applied to the cell can be measured by monitoring linear frequency variations of the outer beams. If cell deformations are also monitored during the compression of the cell, force and deformation information acquired can be used to retrieve the Young's modulus of the cell. Nonetheless, as seen in Chapter 1, a descriptive model is then required.

In many works, Hertz theory is used (see Eq. (1.13)). Hertz theory, however, is subjected to a number of important assumptions. In particular, when dealing with a living cell, the condition of negligible force adhesion is not always fulfilled. Ideally, extended models that take consideration of adhesion and friction forces, such as the JKR (Johnson, Kendall and Roberts) or DMT (Derjaguin, Muller and Toporov) models must be used [205]. In any event, the evolution of the contact surface area between the cell and the flat surface must be continuously monitored during cell compression. Usually, an optical microscope and a video camera are used (e.g., [206, 207, 208]). Large measurement uncertainties can however occur. Moreover, the cell radius must also be optically measured prior to each new compression tests.

To alleviate these difficulties, the author here proposes to adapt a technique inspired from several works where ceramic PZT rod-shaped transducer operating in resonance state have been used to probe the elastic properties of biological samples [209, 210, 211]. Such a technique permits to exploit the resonant prototype in an alternative manner so that the Young's modulus of a cell can be estimated simply and rapidly.

More interestingly, subsequent paragraphs demonstrate that, under certain conditions, a sufficient estimation of the Young's modulus of the cell can be obtained without the use of a descriptive model.

4.3.1   Calibration of the prototype with gel samples

To avoid the use of an analytical model for extracting the Young's modulus of a cell, the prototype was calibrated with materials that serve as reliable references. Gels of known mechanical properties were used. Two silicone gel samples (T5 and T7) from the company Gelmec[1] were ordered. Although these silicone gels were originally intended for vibration damping in mechanical systems, they were very soft. The gel T7 was the softest with a Young's modulus of 37.5 kPa. As for the gel T5, its Young's modulus was 119.5 kPa. These two gels seemed ideal for calibration tests since the Young's modulus of most living cells is known to range from 1 kPa to 100 kPa [3, 212, 213, 214]. Both gels were cautiously prepared in order to obtain small pieces with equivalent dimensions. Efforts were also made to obtain gel samples with a size as similar as possible to the size of the cells targeted.

As previously, the prototype was maintained slightly curved and the indenter placed beneath the structure. Nevertheless, the metal bead mounted on the indenter was here removed and the indenter tip was adapted so that it became perfectly flat. The gel samples were then simply posed on the flat indenter. The indenter was then translated towards the prototype until the gel sample entered in contact with the central beam. This contact could be easily detected by monitoring the frequency of the outer beams with the optical fiber probe.

From the contact point, small incremental motions of 10 μm were then applied in order to gently press the gels upon the central beam. Compression of the gel was monitored with an optical microscope coupled to a video camera that provided a side view of the experiment arrangement. During calibration, attention was paid to verify the contact area between the gels and the central beam. This task was however delicate, mainly because the outer beams sometimes hid the view of the contact area. To probe only the elastic properties of the gels, the amount of compression applied did not exceed 10% of their thickness [215]. In addition, the velocity of the translation steps was kept very slow (4 μm/s) to minimize the occurrence of viscoelastic effects [216, 208]. For a total displacement of 50 μm of the indenter, linear frequency variations measured are plotted in Fig. 4.11 (dashed and dotted lines).

As one could expect, the amount of frequency change for a particular displacement is clearly lower for the gel having the lowest Young's modulus.

---

[1]Further information can be found at http://www.gelmec.co.uk
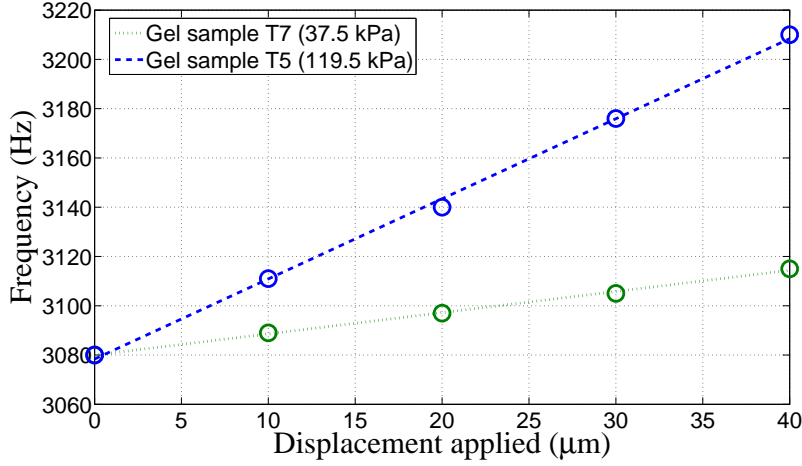
Figure 4.11: Frequency variations of the outer beams for two gel samples. The Young's modulus of the gels were known so that they could be used for calibration. Circles are experimental data. Dashed and dotted lines are fitting curves.

4.3.2 Direct extraction of the Young's modulus of a lobster egg

Once reference curves were obtained with the two gel samples, the protocol previously described was repeated for evaluating the Young's modulus of a living cell. Ideally, experiments could have been conducted on an animal embryo or oocyte. For instance, mouse or zebrafish embryos/oocytes are often used in cell mechanical studies. Therefore, values of Young's modulus have already been reported in the literature for such cells (e.g., [109]). Unfortunately, animal embryos or oocytes could not be obtained.

As a viable alternative, a lobster egg with a similar size was preferred for preliminary tests. In accordance with the initial specifications of the prototype which has been initially designed to deal with large suspended cells, an egg with a diameter of 500 μm was selected. The egg was then handled with great care and manually placed on the flat indenter. Once the egg was placed, the indenter was again translated towards the prototype (see Fig. 4.12).

As for the calibration with the gel samples, a gentle displacement of 50 μm was applied after the egg touched the central beam. Fig. 4.13 compares frequency variations measured with the egg with frequency variations previously obtained with the gel samples.

Interestingly, frequency variations provoked by the lobster egg are greater than the ones generated with the gel T7 (37.5 kPa). Notwithstanding, they are lower than frequency variations measured for the gel T5 (119.5 kPa). It may hence be presumed that the Young's modulus of the lobster egg probed is somewhere between 37.5 kPa and

90
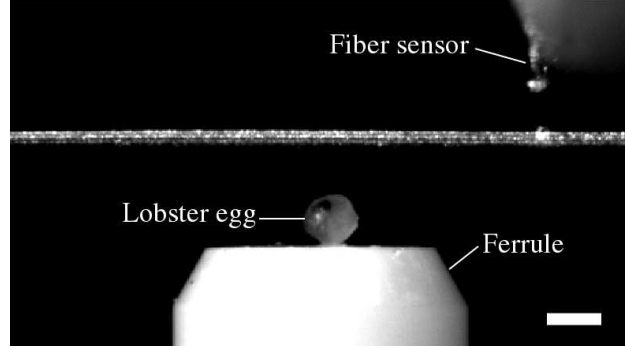
Figure 4.12: Side view of the slightly curved prototype for measuring the Young's modulus of a lobster egg. The latter lies on an optical fiber connector ferrule. The double-fiber displacement probe is visible in the upper right corner. Scale bar represents 500 μm.
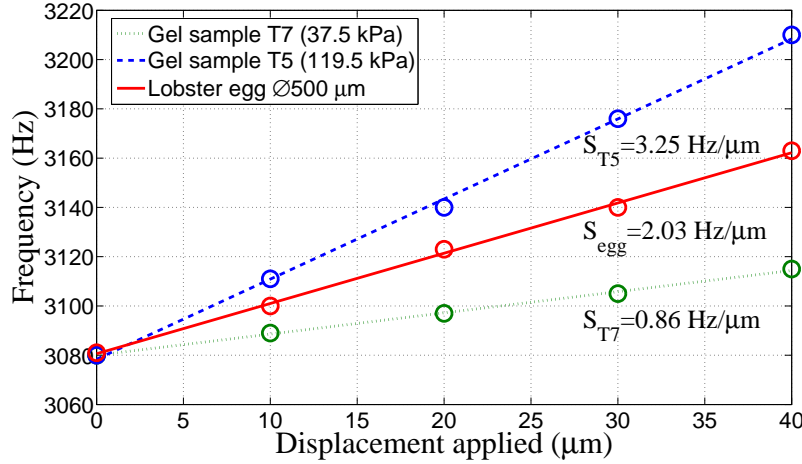
Figure 4.13: Frequency variations measured for one lobster egg. The egg had a diameter of 500 μm and was gently pressed upon the central beam. Curves obtained with the gel samples during calibration are also shown for comparison.

119.5 kPa. To determine more precisely its value, Fig. 4.14 is used.

To construct Fig. 4.14, slopes S_{T5} and S_{T7} (see Fig. 4.13) were used as single values. As indicated by the two squares, these values were plotted against the Young's modulus of the gels. Since only the elastic (i.e., linear) properties of the materials were probed, a linear regression equation linking the two squares could be determined [217]

$$S_{egg} = 0.02914 \times E_{egg} - 0.2329 \tag{4.4}$$

where S_{egg} is the slope of variations frequency measured for the lobster egg and E_{egg} is its Young's modulus. With $E_{egg} = 2.03$ Hz/mN (see Fig. 4.13), Eq. (4.4) yields

91
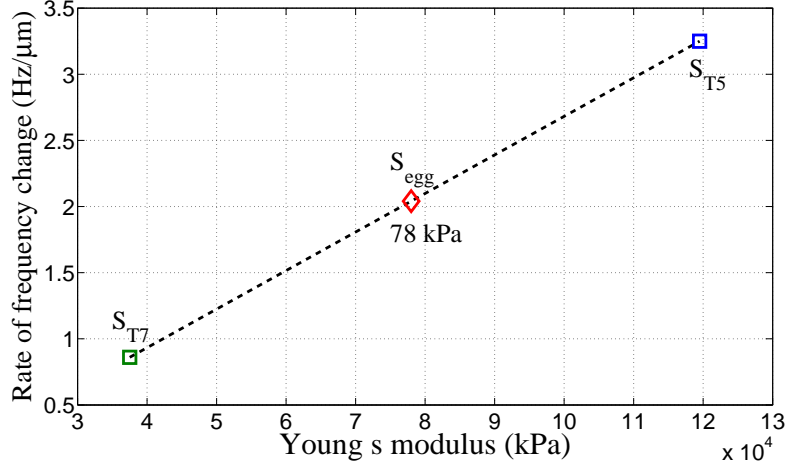
Figure 4.14: Figure proposed for extracting the Young's modulus of the lobster egg (see text for further explanations).

a Young's modulus of 78 kPa for the lobster egg (indicated by the diamond in Fig. 4.14).

In the future, potential estimation errors could be further minimized via a more accurate calibration of the prototype. This could be achieved by using calibrated soft microspheres (e.g., hydrogel or collagen microspheres) having a tight size distribution instead of the manually prepared gels. Ideally, by using cell size sorting systems, a larger number of cells with a similar size should also be tested to confirm the reliability and the repeatability of the method.

The preliminary result obtained with the lobster egg however tends to prove the applicability of the method. Indeed, although no reference value has been found in the literature for lobster eggs, the Young's modulus estimated is in accordance with orders of magnitude usually reported for most cells.

Moreover, it is worth underlining that for diagnosis applications, an absolute value of the Young's modulus is not necessary a mandatory condition to have a useful device. Very often, relative changes or observation of tendencies may be sufficient to bring valuable information of the cell state. Since the planar structure could ultimately keep cells alive in cell medium while estimating their Young's modulus periodically over time with a sufficient accuracy (e.g., for assessing the effects of drugs), it could already prove to be useful for potential clinical utility.

92

4.4 Conclusion

This chapter has reported the fabrication and the experimental characterization of a first prototype intended to deal with suspension cells. The experimental arrangement used has been described. In particular, a specific optical fiber sensor for measuring the static deflection of the structure as well as the oscillation frequency of the outer beams has been developed and implemented. Experiments have been carried out in order to validate the static and dynamic behaviors of the prototype. With the prototype maintained slightly curved, experimental results have proved to be in good agreement with theoretical predictions of Chapter 3. Thereby, a linear displacement sensitivity of 5.75 Hz/μm has been experimentally measured. Via the characterization of an indenter for small displacements, a force sensitivity of $\sim$3 Hz/mN has also been determined. In addition, a quality factor of 700 has been obtained in air. The prototype has also been used with biological samples in order to demonstrate the possibility to use it as a cell diagnosis tool. After a calibration of the prototype with gel samples, a Young's modulus of 78 kPa has been found for a lobster egg with a diameter of 500 μm. Since this prototype was first intended to serve as a proof of concept, necessary improvements could be made. The prototype has however demonstrated the capability to estimate the Young's modulus of a suspension cell in a rapid and sufficiently accurate manner. Preliminary results reported in this chapter are thus encouraging. Future work and challenges that still need to be addressed for the successful implementation of the planar structure in a workable platform will now be discussed in the general conclusion.

Conclusions and suggestions for future research

In the future, versatile MEMS that will be capable of measuring the Young's modulus of various types of cells in a high throughput manner could mark a new milestone in biomedical research. Indeed, the Young's modulus of single cells has been shown to be correlated to pathophysiological states in several major diseases such as cancer or malaria. The Young's modulus might hence prove to be useful to differentiate pathogenic cells among healthy cells and detect diseases at earlier stages. Additionally, values of Young's modulus have the potential to disclose the specific effects of pharmaceuticals at the cellular level. Therefore, cell elasticity measurements may also prove advantageous in drug development.

In this context, this dissertation has presented a new force sensitive structure capable of extracting the Young's modulus of living cells. The first contribution and originality of the structure reported is the use of a dynamic mode to probe the elastic modulus of living cells. Although oscillating devices have been previously successfully used for detecting the presence of target biomolecules, resonant structures have been rarely utilized to extract the elastic properties of living cells. To the best of the author's knowledge, this is the first time that a resonant structure is designed to measure mechanical forces applied to cells and extract their Young's modulus in a liquid environment while keeping high dynamic performances. The possibility to adapt the structure's design with minimum modifications for addressing both suspension and adherent cells also appears as a new feature.

To develop the structure, this dissertation has considered both theoretical and experimental aspects. On a theoretical point of view, a modelling approach based on energy concepts has been developed for investigating the static and dynamic behaviors of the structure. Compared to exact analytical solutions, such an energy approach has proved to be convenient to handle nonlinear effects for a structure incorporating multiple beam resonators. Therefore, the method developed in this work constitutes a valuable tool to investigate structures with a relatively complex geometry. For instance, it could be

transposed in straightforward manner to the theoretical study of coupled resonant mechanical filters where lumped parameter models based on simple spring-mass systems are often used.

To validate theoretical predictions obtained via the modelling approach, a mesoscale prototype intended to serve as a first proof of concept has also been fabricated and experimentally characterized. For monitoring the resonance frequency of the prototype, a fiber displacement probe made of two optical fibers and providing a displacement sensitivity of about 9 mV/μm has been implemented. With this fiber probe, a quality factor of about 700 has been measured in ambient conditions for the prototype fabricated. A linear force sensitivity of about 3 Hz/mN has also been obtained when the prototype was slightly curved. The prototype reported has therefore the potential to resolve a minimum force of at least 3.4 μN if accurate frequency counters can be used. An experimental method has also been presented for calibrating the prototype and for estimating the Young's modulus of a suspension cell without the need of a descriptive model. Such an indirect technique might prove to be useful for rapidly evaluating relative changes in the Young's modulus of cells or for observing tendencies with increased throughput cell measurements.

Preliminary results reported in this dissertation are hence encouraging. Nevertheless, several of the key features considered for the initial design of the structure have not been experimentally validated in this work. Moreover, for the successful use of the planar structure as a workable diagnostic platform, several necessary improvements could be addressed in future research.

- **Recommendations for improving the structure**

Tests conducted with the mesoscale prototype have shaded light on problems due to the clamping apparatus. As for all types of resonant systems, the prototype proves to be very sensitive to boundary conditions. With clamps tightened with screws, it is difficult to obtain a homogeneous pressure over the entire anchors' area of the prototype. Presently, this affects the repeatability of measurements. Likewise, maintaining the structure in a slightly curved position with the manual positioning stage turns out to be a delicate task. To overcome these problems, tests should be conducted to scale down the structure with microfabrication processes. With a MEMS version of the structure, the clamping system as presented in this manuscript would not be required anymore. Moreover, with MEMS processes, previous works have shown that stresses in the substrate could be controlled so that the structure could be fabricated directly curved [218].

Currently, the structure cannot be used as expounded in the initial concept since suspension cells cannot be held. Therefore, the implementation of a trapping system for suspension cells (e.g., a microwell, dielectrophoretic electrodes, etc.) could be investigated. The etching of a microchannel or a microwell should also be further investigated.

Tests should be conducted with the microchannel/microwell filled with liquids. Indeed, even though it has been experimentally confirmed that the amount of vibrations transferred to the central beam during the oscillation of the resonators is very low, infinitesimal vibrations could all the same interact with fluids. Such fluid movements might transfer unwanted stimuli to cells. If required, the possibility to optimize the attachment points between the overhangs and the beam resonators via the presence of stubs (see Fig. 4.15) or outriggers [219] might further limit the presence of vibrations at the half span of the central beam.
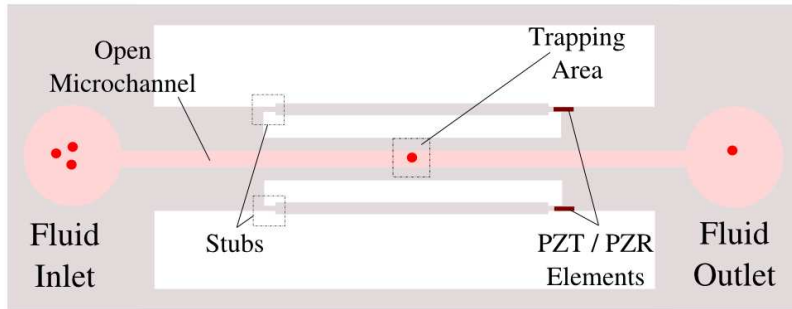
Figure 4.15: Sketch depicting a MEMS version of the structure with possible improvements that could be tested in future research. The sketch here represents a top view of the structure with an open microchannel and suspension cells. The beam resonators could be terminated by stubs to further minimize vibrations transferred to the central beam. To measure the resonance frequency, displacement probes with only one fiber could be tested (not represented). Alternatively, PZT or PZR elements could be patterned.

Finally, no test has been conducted with adherent cells yet. To validate the possibility to address such cells, the miniaturization of the structure could be optimized to exploit a higher resonance frequency. To measure the resonance frequency on a micrometer-scale structure, a fiber sensor head made of only one fiber could be tested [195]. Alternatively, the possibility to precisely pattern and deposit PZT or PZR elements at the basis of the beam resonators with microfabrication processes could prove to be a more convenient option. Since the structure is inherently a force sensor, it could also be interesting to investigate if it could be used for the force-controlled injection of adherent cells.

- **Long term prospects**

In the long term, MEMS embedded in complex lab-on-chip systems capable of estimating the elastic properties of cells in a high throughput manner could be one of the mainstream technologies in the next decades. MEMS have indeed the potential to let the system moves from the laboratory to the point-of-need. For a disease such as malaria,

which is prolific in Africa, MEMS open up the possibility for on-site analysis at low costs. Ultimately, credit-card sized and self-contained platforms integrating microfluidic systems, MEMS actuators, MEMS sensors and electronic processing units could enable diagnostic assays performed within minutes. This could allow the fast screening and monitoring of patients, and a more frequent control of drug efficiency, leading to a customized therapy and subsequently to therapy control.

Constant progresses are already paving the way for closing the gap between diagnostic needs and available technologies. However, many microfabricated devices devoted to the measurement of the cell Young's modulus act today primarily as actuation means that deform cells. Most of the time, the cell deformation must then be monitored in a way or another via an optical equipment. One of the most widespread option is to use visual feedback provided by a microscope and a video camera. This can be legitimately explained by the fact that a microscope obviously remains an essential tool for conducting cell analysis. Promising results have already been reported in laboratory environments with MEMS exploiting vision feedback for suspension cells. Nevertheless, the need of a microscope prevents the use of MEMS as portable and autonomous devices.

In this sense, the force sensitive structure presented in this dissertation has proposed a non visual-based solution. Ideally, the Young's modulus of cells could be estimated with sufficient accuracy without the need of a microscope. This is in favour of a compact sensing unit. On the other hand, and beyond the necessary improvements aforementioned, the integration of an appropriate microactuator for replacing the external indenter presently used would be required for portability. Because most microactuators presently require a bulky power supply, novel actuation solutions with limited power resources should be developed. In addition, the actuator design should fit the dimensions of the microchannel. Designing a microactuator satisfying such specifications obviously poses challenges. However, it opens up new research prospects and might also find application in related research fields such as microrobotics.

Appendix

Derivation of the undamped fundamental frequency of a CC beam

From Euler-Bernouilly theory, the equation that governs the motion of a CC beam is

$$EI\,\frac{\partial^4 w(x,t)}{\partial x^4} + N\frac{\partial^2 w(x,t)}{\partial x^2} + m_b^*\,\frac{\partial^2 w(x,t)}{\partial t^2} = 0 \tag{4.5}$$

where $m_b^* = \rho_b\,S$ and $I = \frac{bh^3}{12}$ are the mass per unit length and the moment of inertia of the beam, respectively. Other notations are defined in the list of notations provided for Chapter 2.

Equation (4.5) is a linear, homogeneous partial-differential equation. A variety of techniques can be called on to solve such an equation. Here, it is assumed that there is a separable solution; that is

$$w(x,t) = W(x)\,Q(t) \tag{4.6}$$

where $W(x)$ is a function that depends only on the spatial variable x and $Q(t)$ depends only the temporal variable t. Since the beam is supposed to be in harmonic motion during vibration, one can let

$$Q(t) \propto e^{j\omega t} \tag{4.7}$$

where $j^2 = -1$ and ω represents the angular frequency of the oscillating beam. Substituing Eq. (4.6) into Eq. (4.5) and making use of Eq. (4.7), the partial differential equation is transformed into a single differential equation

$$\frac{d^4 W(x)}{dx^4} + \sigma^2\frac{d^2 W(x)}{dx^2} - \Omega^4 W(x) = 0 \tag{4.8}$$

where $\sigma^2 = \dfrac{N}{EI}$ and $\Omega^4 = \dfrac{m_b^*\omega^2}{EI}$.

If one lets $W(x) = Ae^{\lambda x}$, it can be shown that a general solution of Eq. (4.8) is [220, 221]

$$W(x) = C_1 \sin(\alpha_1 x) + C_2 \cos(\alpha_1 x) + C_3 \sinh(\alpha_2 x) + C_4 \cosh(\alpha_2 x) \qquad (4.9)$$

where

$$\alpha_1 = \sqrt{\frac{\sigma^2}{2} + \frac{1}{2}\sqrt{(\sigma^4 + 4\Omega^4)}} \qquad (4.10)$$

$$\alpha_2 = \sqrt{-\frac{\sigma^2}{2} + \frac{1}{2}\sqrt{(\sigma^4 + 4\Omega^4)}}. \qquad (4.11)$$

The unknown constants C_n in Eq. (4.9) can be determined from the boundary conditions of the beam. In the case of an ideal CC beam, extremities of the beam are considered to be firmly attached, so that displacement and slope are zero at both ends. Therefore boundary conditions are

$$W(x)\Big|_{x=0} = 0, \quad \frac{dW(x)}{dx}\Big|_{x=0} = 0, \qquad (4.12)$$

$$W(x)\Big|_{x=L} = 0, \quad \frac{dW(x)}{dx}\Big|_{x=L} = 0. \qquad (4.13)$$

Substituing Eq. (4.9) into Eqs. (4.12-4.13), a set of four algebraic homogeneous equations in the four unknowns C_n is obtained

$$C_2 + C_4 = 0 \qquad (4.14)$$
$$C_1\,\alpha_1 + C_3\,\alpha_2 = 0 \qquad (4.15)$$
$$C_1 \sin(\alpha_1 L) + C_2 \cos(\alpha_1 L) + C_3 \sinh(\alpha_2 L) + C_4 \cosh(\alpha_2 L) = 0 \qquad (4.16)$$
$$C_1\alpha_1 \cos(\alpha_1 L) - C_2\alpha_1 \sin(\alpha_1 L) + C_3\alpha_2 \cosh(\alpha_2 L) + C_4\alpha_2 \sinh(\alpha_2 L) = 0. \qquad (4.17)$$

Equations (4.14-4.17) can be rewritten in a matrix form as

$$\mathbb{A}\,.\,\mathbb{C} = 0, \qquad (4.18)$$

where the coefficient matrix $\mathbb{A}$ is

$$\mathbb{A} = \begin{bmatrix} 0 & 1 & 0 & 1 \\ \alpha_1 & 0 & \alpha_2 & 0 \\ \sin(\alpha_1 L) & \cos(\alpha_1 L) & \sinh(\alpha_2 L) & \cosh(\alpha_2 L) \\ \alpha_1 \cos(\alpha_1 L) & -\alpha_1 \sin(\alpha_1 L) & \alpha_2 \cosh(\alpha_2 L) & \alpha_2 \sinh(\alpha_2 L) \end{bmatrix}. \qquad (4.19)$$

Equation (4.18) has non trivial solutions if and only if the coefficient matrix $\mathbb{A}$ is singular; that is, its determinant is zero. Setting the determinant of $\mathbb{A}$ equal to zero yields

$$1 - \cos(\alpha_1 L) \cosh(\alpha_2 L) + \frac{\sigma^2}{2\,\Omega^2} \sin(\alpha_1 L) \sinh(\alpha_2 L) = 0 \qquad (4.20)$$

99

The above transcendental equation can be solved numerically to find natural frequencies. It is interesting to note that if $N = 0$, then $\alpha_1 = \alpha_2 = \alpha$ and Eq. (4.20) reduces to the characteristic equation of a CC beam without axial load

$$\cos(\Omega L)\cosh(\Omega L) = 1. \tag{4.21}$$

Because the study is limited to the fundamental (i.e., first) resonance frequency of the beam, one only seeks for the smallest root of Eq. (4.21) which is $\Omega_1 L = 4.73$. With the notation $\Omega^4 = \dfrac{m_b^* \omega^2}{EI}$ previously introduced, the fundamental angular frequency of a CC beam is thus

$$\omega_1 = \frac{22.37}{L^2} \sqrt{\frac{EI}{m_b^*}}. \tag{4.22}$$

To compute the mode shape associated to ω_1, one can still refer to the set of algebraic equations (4.14-4.17). Indeed, Eq. (4.14) and Eq. (4.15) allow us to immediately conclude that $C_2 = -C_4$ and $C_3 = -\frac{\alpha_1}{\alpha_2}C_3$. A third constant can be eliminated by using Eq. (4.16). Thereby, one obtains

$$W(x) = C_1 \left[\sin(\alpha_1 x) + \lambda \cos(\alpha_1 x) - \frac{\alpha_1}{\alpha_2} \sinh(\alpha_2 x) - \lambda \cosh(\alpha_2 x) \right] \tag{4.23}$$

where

$$\lambda = \frac{\sin(\alpha_1 L) - \frac{\alpha_1}{\alpha_2} \sinh(\alpha_2 L)}{\cosh(\alpha_2 L) - \cos(\alpha_1 L)}. \tag{4.24}$$

Abbreviations and Notations

List of Abbreviations

AC	Alternative Current
AFM	Atomic Force Microscope
CC	Clamped-Clamped
EAP	Electro Active Polymers
EDM	Electro Discharge Machining
FEA	Finite Element Analysis
GUV	Giant Unilamellar Vesicle
MEMS	Micro Electro Mechanical Systems
PDMS	Polyimethylsiloxane
MT	Magnetic Tweezers
OS	Optical Stretcher
OT	Optical Tweezers
PZR	Piezoresistive
PZT	Piezoelectric
Q factor	Quality factor
RBC	Red Blood Cell
SCD	Sickle Cell Disease
VCSEL	Vertical Cavity Surface Emitting Laser

List of Notations

<u>Chapter 1</u>

b Width of thermal beams

b_{mc} Width of microchannels

B Magnetic field

c_l Speed of light in vacuum

$C(\omega)$ Clausius-Mossotti factor

d_0 Position of capacitor plates at rest

E, E_{mp}, E_{si} Young's moduli

E^*, E_1, E_2 Effective Young's modulus and Young's moduli

F_c Force applied to cell

F_{capa} Force resolved by capacitance changes

$F_{electro}$ Electrostatic force

F_{mag} Magnetic force

F_{mp} Force applied to passive microposts

F_{os} Force developed by divergent laser beams

$F_{P_{mag}}$ Force of magnetic microposts

F_{therm} Thermal force

g_{ce} Comb electrode gap

h Thickness of thermal beams

h_{mc} Thickness of microchannels

I_{mp} Moment of inertia of microposts

J Electric field

k Thermal conductivity

K_s Constant related to cells

L_{c_0}, L_c	Lengths related to cells
L, L_p	Lengths related to thermal beams
L_{mp}	Length of microposts
L_w	Length of magnetic nanowires
M_{mb}	Magnetic moment of microbeads
n_m	Refractive index of media
n_c	Refractive index of cells
N_{ce}	Number of comb electrodes
N_{tb}	Number of thermal beams
P_l	Optical light power
r_{tb}	Electrical resistance
R_1, R_2	Radii of curvature
R_e	Reynolds number
R_{rl}	Fraction of reflected light
t_{ce}	Comb thickness
Tb_{vol}	Volume of thermal beams
U, U_{out}, U_s	Voltages
X, Y	Spatial coordinates
α	Thermal expansion coefficient
δ_c	Cell deformation
Δ_{mp}	Deflection of microposts
ϵ	Permittivity constant
η	Fluid viscosity
$\mu_\perp$	Component of dipole moment perpendicular to B
ν	Volumetric flow rate
τ_w	Wall shear stress
ω	Angular frequency

Chapter 2

$A_0, A(\omega)$ Amplitudes of oscillation

b Beam width

$\mathcal{D}$ Rayleigh's dissipation function

E Young's modulus

I Moment of inertia

h Beam thickness

L Beam length

$\mathcal{L}$ Lagrangian

m_b^* Beam mass per unit length

m_b Beam mass

m_a^* Mass per unit length added by a fluid

m_a Mass added by a fluid

m_{tot}^* Total mass per unit length $m_{tot}^* = m_b^* + m_a^*$

m_{tot} Total mass $m_{tot} = m_b + m_a$

K_0, K_1 Bessel functions of the second kind

N Axial force

P_{loss}^* Averaged dissipated power per unit length due to a fluid

S Beam cross sectional area

s_F Force sensitivity

R_e Reynolds number

t Temporal variable

T Time period $T = 2\pi/\omega$

q General coordinates

$\dot{q}$ Time derivative of q

Q Overall quality factor

Q_{int} Losses related to structural damping

Q_{anch}	Losses due to beam supports
Q_{fluid}	Losses due to the presence of a fluid
V_a	Energy related to axial forces
V_b	Bending energy
V_{kin}	Kinetic energy
V_{loss}	Dissipated energy per cycle per time period
V_{pot}	Potential energy
$w(x,t)$	Transverse deflections
$W(x)$	Mode shape
x	Spatial variable
γ_a^*	Damping coefficient per unit length due to a fluid
γ_a	Damping coefficient due to a fluid
Γ	Hydrodynamic function
η	Fluid viscosity
ρ_b	Density of beam material
ρ_{fluid}	Density of surrounding fluid
ω	Angular frequency
ω_1	Undamped fundamental angular frequency
ω_{fluid}	Fundamental angular frequency in fluids

Chapter 3

A Cross sections

b Width of tuning fork's segments

b_o Width of overhangs

b_1 Width of outer beams

b_2 Width of central beam

D_s Midspan deflection

E Young's modulus

f_0, f Frequencies

F, F_v Punctual force and virtual punctual force

I_i Moments of inertia

h Thickness

k_{r1} Stiffness of rotational springs

k_1, k_3 Linear and nonlinear spring constants

k_{eq} Equivalent stiffness

l Length of outer beams

l_o Length of overhangs

L Total length

m_{eq} Equivalent mass

T Time period $T = 2\pi/\omega$

U_{tf} Total potential energy of tuning fork

U_b Strain energy due to bending

U_{rs} Energy stored by rotational springs

U_s Strain energy due to stretching

U_T Total potential energy

$w_i(x)$ Transverse displacement functions

W, W_1 Work done by punctual forces

x	Spatial variable
Φ, Φ_1	Total potential energy functions

Chapter 4

E_{egg} Young's modulus of lobster egg

g Gap between the fibers flat ends and the reflective target

P_t Optical power exiting the transmitting fiber

P_r Optical power captured by the receiving fiber

Q Quality factor

S_{egg} Rate of frequency change

z_a Light asymptotic cone apex

List of Publications

Part of the work presented in this PhD dissertation is either based on or related in some degree to the following list of refereed publications:

Chapter Book

Micro Systems for the Mechanical Characterization of Isolated Biological Cells: State-of-the-Art,
D. Desmaële, M. Boukallel, et S. Régnier, *Wearable and Autonomous Biomedical Devices and Systems for Smart Environment*, Lecture Notes in Electrical Engineering, Springer.

Journal Articles

A resonant structure designed for probing the elastic properties of suspension and adherent cells in liquid environments,
D. Desmaële, M. Boukallel, et S. Régnier, *Journal of Micromechanics and Microengineering*, 22 : 115033, 2012.

Actuation Means for the Mechanical Stimulation of Living Cells via Microelectromechanical Systems: A Critical Review,
D. Desmaële, M. Boukallel, et S. Régnier, *Journal of Biomechanics*, 44(8) : 1433–1446, 2011.

Peer-reviewed Conference Papers

Design and Fabrication of a Novel Resonant Surface Sensitive to Out-of-plane Forces for the Indentation and Injection of Living Cells,
D. Desmaële, M. Boukallel, et S. Régnier, in *Proceedings IEEE/RSJ International Conference on Intelligent Robots and Systems (IROS)*, San Fransisco, CA, USA, September 2011. *Acceptance rate - 32%.*

A Planar Structure Sensitive to Out-of-plane Forces for the Force-controlled Injection of Suspended and Adherent Cells,
D. Desmaële, M. Boukallel, et S. Régnier, *in Proceedings IEEE Engineering in Medicine and Biology Society (EMBC)*, Boston, MA, USA, September 2011.

A Planar Resonant Structure Sensitive to Out-of-Plane Forces,
D. Desmaële, M. Boukallel, et S. Régnier, *in Proceedings EuroSensors XXV*, Athens, Greece, September 2011.

Bibliography

[1] J. H. C. Wang and B. P. Thampatty, "An introductory review of cell mechanobiology," *Biomechanics and Modeling in Mechanobiology*, vol. 5, no. 1, pp. 1–16, 2006.

[2] D.-H. Kim, P. KinWong, J. Park, A. Levchenko, and Y. Sun, "Microengineered platforms for cell mechanobiology," *Annual Review of Biomedical Engineering*, vol. 11, pp. 203—-233, 2009.

[3] G. Bao and S. Suresh, "Cell and molecular mechanics of biological materials," *Nature Materials*, vol. 2, no. 11, pp. 715–725, 2003.

[4] P. A. Janmey and C. A. McCulloch, "Cell mechanics: integrating cell responses to mechanical stimuli," *Annual Review of Biomedical Engineering*, vol. 9, pp. 1–34, 2007.

[5] T. P. Lele, J. E. Sero, B. D. Matthews, S. Kumar, S. Xia, M. Montoya-Zavala, T. Polte, D. Overby, N. Wang, and D. E. Ingber, "Tools to study cell mechanics and mechanotransduction," *Methods in Cell Biology*, vol. 83, p. 443, 2007.

[6] B. D. Hoffman and J. C. Crocker, "Cell mechanics: Dissecting the physical responses of cells to force," *Annual Review of Biomedical Engineering*, vol. 11, pp. 259–288, 2009.

[7] T. D. Brown, "Techniques for mechanical stimulation of cells in vitro: a review," *Journal of Biomechanics*, vol. 33, no. 1, pp. 3–14, 2000.

[8] G. Y. H. Lee and C. T. Lim, "Biomechanics approaches to studying human diseases," *Trends in Biotechnology*, vol. 25, no. 3, pp. 111–118, 2007.

[9] E. A. G. Peeters, "Biomechanics of single cells under compression," Ph.D. dissertation, Technische Universiteit Eindhoven, 2004.

[10] E. Evans and A. Yeung, "Apparent viscosity and cortical tension of blood granulocytes determined by micropipet aspiration," *Biophysical Journal*, vol. 56, pp. 151–160, 1989.

[11] M. Sato, D. P. Theret, L. Wheeler, N. Ohshima, and R. M. Nerem, "Application of the micropipette technique to the measurement of cultured porcine aortic endothelial cell viscoelastic properties," *Journal of Biomechanical Engineering*, vol. 112, no. 3, pp. 263–268, 1990.

[12] H. Miyazaki, Y. Hasegawa, and K. Hayashi, "A newly designed tensile tester for cells and its application to fibroblasts," *Journal of Biomechanics*, vol. 33, no. 1, pp. 97–104, 2000.

[13] M. Lekka, P. Laidler, D. Gil, J. Lekki, Z. Stachura, and A. Z. Hrynkiewicz, "Elasticity of normal and cancerous human bladder cells studied by scanning force microscopy," *European Biophysics Journal*, vol. 28, no. 4, pp. 312–316, 1999.

[14] J. A. J. van der Rijt, K. O. van der Werf, M. L. Bennink, P. J. Dijkstra, and J. Feijen, "Micromechanical testing of individual collagen fibrils," *Macromolecular Bioscience*, vol. 6, no. 9, pp. 697–702, 2006.

[15] Q. S. Li, G. Y. H. Lee, C. N. Ong, and C. T. Lim, "AFM indentation study of breast cancer cells," *Biochemical and Biophysical Research Communications*, vol. 374, no. 4, pp. 609–613, 2008.

[16] S. E. Cross, Y. S. Jin, J. Tondre, R. Wong, J. Y. Rao, and J. K. Gimzewski, "AFM-based analysis of human metastatic cancer cells," *Nanotechnology*, vol. 19, p. 384003 (8pp), 2008.

[17] A. Pillarisetti, C. Keefer, and J. P. Desai, "Mechanical characterization of fixed undifferentiated and differentiating mESC," in *2nd IEEE RAS & EMBS International Conference on Biomedical Robotics and Biomechatronics*, USA, 2008, pp. 618–623.

[18] M. Boukallel, M. Girot, and S. Régnier, "Characterization of cellular mechanical behavior at the microscale level by a hybrid force sensing device," *Journal of the Mechanical Behavior of Biomedical Materials*, vol. 2, no. 3, pp. 297–304, 2009.

[19] O. Thoumine, A. Ott, O. Cardoso, and J. Meister, "Microplates: a new tool for manipulation and mechanical perturbation of individual cells," *Journal of Biochemical and Biophysical Methods*, vol. 39, no. 1-2, pp. 47–62, 1999.

[20] N. Desprat, A. Guiroy, and A. Asnacios, "Microplates-based rheometer for a single living cell," *Sensors and Actuators B: Chemical*, vol. 77, pp. 05 511 (1–9), 2006.

[21] P. Fernández, P. A. Pullarkat, and A. Ott, "A master relation defines the nonlinear viscoelasticity of single fibroblasts," *Biophysical Journal*, vol. 90, no. 10, pp. 3796–3805, 2006.

[22] E. Gladilin, A. Micoulet, B. Hosseini, K. Rohr, J. Spatz, and R. Eils, "3D finite element analysis of uniaxial cell stretching: from image to insight," *Physical Biology*, vol. 4, pp. 104–113, 2007.

[23] B. P. Chan, C. Li, K. L. Au-Yeung, K. Y. Sze, and A. H. W. Ngan, "A microplate compression method for elastic modulus measurement of soft and viscoelastic collagen microspheres," *Annals of Biomedical Engineering*, vol. 36, no. 7, pp. 1254–1267, 2008.

[24] E. Koay, A. Shieh, and K. Athanasiou, "Creep indentation of single cells," *Journal of Biomechanical Engineering*, vol. 125, p. 334, 2003.

[25] E. A. G. Peeters, C. W. J. Oomens, C. V. C. Bouten, D. L. Bader, and F. P. T. Baaijens, "Mechanical and failure properties of single attached cells under compression," *Journal of Biomechanics*, vol. 38, no. 8, pp. 1685–1693, 2005.

[26] K. Sato, T. Adachi, D. Ueda, M. Hojo, and Y. Tomita, "Measurement of local strain on cell membrane at initiation point of calcium signaling," *Journal of Biomechanics*, vol. 40, no. 6, pp. 1246–1255, 2007.

[27] K. Van Vliet, G. Bao, and S. Suresh, "The biomechanics toolbox: experimental approaches for living cells and biomolecules," *Acta Materialia*, vol. 51, no. 19, pp. 5881–5905, 2003.

[28] H. Huang, R. D. Kamm, and R. T. Lee, "Cell mechanics and mechanotransduction: pathways, probes, and physiology," *American Journal of Physiology - Cell Physiology*, vol. 287, no. 1, pp. C1–C11, 2004.

[29] A. Geitmann, "Experimental approaches used to quantify physical parameters at cellular and subcellular levels," *American Journal of Botany*, vol. 93, no. 10, pp. 1380–1390, 2006.

[30] K. A. Addae-Mensah and J. P. Wikswo, "Measurement techniques for cellular biomechanics in vitro," *Experimental Biology and Medecine*, vol. 233, no. 7, pp. 792–809, 2008.

[31] J. J. Norman, V. Mukundan, D. Bernstein, and B. L. Pruitt, "Microsystems for biomechanical measurements," *Pediatric Research*, vol. 63, no. 5, p. 576, 2008.

[32] O. Loh, V. A., and H. D. Espinosa, "The potential of MEMS for advancing experiments and modeling in cell mechanics," *Experimental Mechanics*, vol. 49, no. 1, pp. 105–124, 2009.

[33] S. Sen and S. Kumar, "Combining mechanical and optical approaches to dissect cellular mechanobiology," *Journal of Biomechanics*, vol. 43, no. 1, pp. 45–54, 2010.

[34] S. Eppell, B. Smith, H. Kahn, and R. Ballarini, "Nano measurements with microdevices: mechanical properties of hydrated collagen fibrils," *Journal of The Royal Society Interface*, vol. 3, no. 6, pp. 117–121, 2006.

[35] Z. L. Shen, M. R. Dodge, H. Kahn, R. Ballarini, and S. J. Eppell, "Stress-strain experiments on individual collagen fibrils," *Biophysical Journal*, vol. 95, no. 8, pp. 3956–3963, October 2008.

[36] N. Scuor, P. Gallina, H. Panchawagh, R. Mahajan, O. Sbaizero, and V. Sergo, "Design of a novel MEMS platform for the biaxial stimulation of living cells," *Biomedical Microdevices*, vol. 8, no. 3, pp. 239–246, 2006.

[37] Y. Zhu, A. Corigliano, and H. D. Espinosa, "A thermal actuator for nanoscale in situ microscopy testing: design and characterization," *Journal of Micromechanics and Microengineering*, vol. 16, pp. 242–253, 2006.

[38] S. Lu, Z. Guo, W. Ding, and R. S. Ruoff, "Analysis of microelectromechanical system testing stage for tensile loading of nanostructures," *Review of Scientific Instruments*, vol. 77, pp. 056 103 (1–4), 2006.

[39] H. D. Espinosa, Y. Zhu, and N. Moldovan, "Design and operation of a MEMS-based material testing system for nanomechanical characterization," *Journal of Microelectromechanical Systems*, vol. 16, no. 5, pp. 1219–1231, 2007.

[40] G. F. Christopher, J. M. Yoo, N. Dagalakis, S. D. Hudson, and K. B. Migler, "Development of a MEMS based dynamic rheometer," *Lab on a Chip*, vol. 10, pp. 2749–2757, 2010.

[41] I. Kushkiev and M. A. Jupina, "Modeling the thermo-mechanical behavior of a "V"-shaped composite buckle-beam thermal actuator," in *COMSOL Multiphysics User's Conference*, Boston, 2005.

[42] D. Girbau, A. Lázaro, and L. Pradell, "RF MEMS switches based on the buckled-beam thermal actuator," in *33rd European Microwave Conference*, vol. 2, October 2003, pp. 651–654.

[43] W. Zhang, M. Gnerlich, J. J. Paly, Y. Sun, G. Jing, A. Voloshin, and S. Tatic-Lucic, "A polymer V-shaped electrothermal actuator array for biological applications," *Journal of Micromechanics and Microengineering*, vol. 18, no. 7, p. 075020 (8pp), 2008.

[44] S. Akbari, M. Niklaus, and H. Shea, "Arrays of EAP micro-actuators for single-cell stretching applications," in *Electroactive Polymer Actuators and Devices (EAPAD)*, Y. Bar-Cohen, Ed., vol. 7642, no. 1. SPIE, 2010, p. 76420H.

[45] F. H. C. Crick and A. F. W. Hughes, "The physical properties of cytoplasm: A study of the magnetic particle method part I, Experimental," *Experimental Cell Research*, vol. 1, pp. 37–80, 1950.

[46] C.-H. Chiou, Y.-Y. Huang, M.-H. Chiang, H.-H. Lee, and G.-B. Lee, "New magnetic tweezers for investigation of the mechanical properties of single DNA molecules," *Nanotechnology*, vol. 17, no. 5, pp. 1217–1224, 2006.

[47] J. Kanger, V. Subramaniam, and R. van Driel, "Intracellular manipulation of chromatin using magnetic nanoparticles," *Chromosome Research*, vol. 16, pp. 511–522, 2008.

[48] M. K. Yapici, A. E. Ozmetin, J. Zou, and D. G. Naugle, "Development and experimental characterization of micromachined electromagnetic probes for biological manipulation and stimulation applications," *Sensors and Actuators A: Physical*, vol. 144, no. 1, pp. 213 – 221, 2008.

[49] Z. Zhang, K. Huang, and C. H. Menq, "Design, implementation, and force modeling of quadrupole magnetic tweezers," *IEEE/ASME Transactions on Mechatronics*, vol. 15, no. 5, pp. 704–713, 2010.

[50] A. H. B. de Vries, J. S. Kanger, B. E. Krenny, and R. van Driel, "Patterned electroplating of micrometer scale magnetic structures on glass substrates," *Journal of Microelectromechanical Systems*, vol. 13, no. 3, pp. 391–395, 2004.

[51] A. H. B. de Vries, B. E. Krenny, R. van Driel, and J. S. Kanger, "Micro magnetic tweezers for nanomanipulation inside live cells," *Biophysical Journal*, vol. 88, pp. 2137—-2144, March 2005.

[52] D. Simson, F. Ziemann, M. Strigl, and R. Merkel, "Micropipet-based pico force transducer: in depth analysis and experimental verification," *Biophysical Journal*, vol. 74, no. 4, pp. 2080–2088, 1998.

[53] F. J. Alenghat, B. Fabry, K. Y. Tsai, W. H. Goldmann, and D. E. Ingber, "Analysis of cell mechanics in single vinculin-deficient cells using a magnetic tweezer," *Biochemical and Biophysical Research Communications*, vol. 277, no. 1, pp. 93–99, 2000.

[54] J. Reed, M. Frank, J. Troke, J. Schmit, S. Han, M. Teitell, and J. Gimzewski, "High throughput cell nanomechanics with mechanical imaging interferometry," *Nanotechnology*, vol. 19, no. 23, p. 235101, 2008.

[55] R. C. Spero, L. Vicci, J. Cribb, D. Bober, V. Swaminathan, E. T. O'Brien, S. L. Rogers, and R. Superfine, "High throughput system for magnetic manipulation of cells, polymers, and biomaterials," *Review of Scientific Instruments*, vol. 79, no. 8, pp. 083 707 (1–7), 2008.

[56] A. H. B. de Vries, B. E. Krenn, R. van Driel, V. Subramaniam, and J. S. Kanger, "Direct observation of nanomechanical properties of chromatin in living cells," *Nano Letters*, vol. 7, no. 5, pp. 1424–1427, 2007.

[57] N. J. Sniadecki, A. Anguelouch, M. T. Yang, C. M. Lamb, Z. Liu, S. B. Kirschner, Y. Liu, D. H. Reich, and C. S. Chen, "Magnetic microposts as an approach to apply forces to living cells," *Proceedings of the National Academy of Sciences of the United States of America*, vol. 104, no. 27, pp. 14 553–14 558, 2007.

[58] N. J. Sniadecki, C. M. Lamb, Y. Liu, C. S. Chen, and D. H. Reich, "Magnetic microposts for mechanical stimulation of biological cells: Fabrication, characterization, and analysis," *Review of Scientific Instruments*, vol. 79, no. 044302, pp. 1–8, 2008.

[59] H. Engelhardt and E. Sackmann, "On the measurement of shear elastic moduli and viscosities of erythrocyte plasma membranes by transient deformation in high frequency electric fields," *Biophysical Journal*, vol. 54, no. 3, pp. 495–508, 1988.

[60] P. K. Wong, W. Tan, and C. M. Ho, "Cell relaxation after electrodeformation: effect of latrunculin a on cytoskeletal actin," *Journal of Biomechanics*, vol. 38, no. 3, pp. 529–535, 2005.

[61] K. A. Riske and R. Dimova, "Electric pulses induce cylindrical deformations on giant vesicles in salt solutions," *Biophysical Journal*, vol. 91, no. 5, pp. 1778–1786, 2006.

[62] R. Dimova, K. A. Riske, S. Aranda, N. Bezlyepkina, R. L. Knorr, and R. Lipowsky, "Giant vesicles in electric fields," *Soft Matter*, vol. 3, pp. 817–827, 2007.

[63] I. Guido, M. S. Jaeger, and C. Duschl, "Dielectrophoretic stretching of cells allows for characterization of their mechanical properties," *European Biophysics Journal*, vol. 40, pp. 281–288, 2011.

[64] V. L. Sukhorukov, H. Mussauer, and U. Zimmermann, "The effect of electrical deformation forces on the electropermeabilization of erythrocyte membranes in low-and high-conductivity media," *Journal of Membrane Biology*, vol. 163, no. 3, pp. 235–245, 1998.

[65] J. Korlach, C. Reichle, T. Müller, T. Schnelle, and W. Webb, "Trapping, deformation, and rotation of giant unilamellar vesicles in octode dielectrophoretic field cages," *Biophysical Journal*, vol. 89, no. 1, pp. 554–562, 2005.

[66] H. Zou, S. Mellon, R. R. A. Syms, and K. E. Tanner, "2-dimensional MEMS dielectrophoresis device for osteoblast cell stimulation," *Biomedical Microdevices*, vol. 8, no. 4, pp. 353–359, 2006.

[67] L. A. MacQueen, M. M. Thibault, M. D. Buschmann, and M. R. Wertheimer, "Electro-deformation of individual mammalian cells in suspension," in *10th IEEE International Conference on Solid Dielectrics (ICSD)*, Postdam, Germany, July 2010, pp. 1–4.

[68] N. Bao, Y. Zhan, and C. Lu, "Microfluidic electroporative flow cytometry for studying single-cell biomechanics," *Analytical Chemistry*, vol. 80, no. 20, pp. 7714–7719, 2008.

[69] A. Ashkin, "Acceleration and trapping of particles by radiation pressure," *Physical Review Letters*, vol. 24, no. 4, pp. 156–159, 1970.

[70] A. Constable, J. Kim, J. Mervis, F. Zarinetchi, and M. Prentiss, "Demonstration of a fiber-optical light-force trap," *Optics Letters*, vol. 18, no. 21, pp. 1867–1869, 1993.

116

[71] W. Singer, M. Frick, S. Bernet, and M. Ritsch-Marte, "Self-organized array of regularly spaced microbeads in a fiber-optical trap," *Journal of the Optical Society of America B*, vol. 20, no. 7, pp. 1568–1574, 2003.

[72] B. Lincoln, S. Schinkinger, K. Travis, F. Wottawah, S. Ebert, F. Sauer, and J. Guck, "Reconfigurable microfluidic integration of a dual-beam laser trap with biomedical applications," *Biomedical Microdevices*, vol. 9, no. 5, pp. 703–710, 2007.

[73] C. W. Lai, S. K. Hsiung, C. L. Yeh, A. Chiou, and G. B. Lee, "A cell delivery and pre-positioning system utilizing microfluidic devices for dual-beam optical trap-and-stretch," *Sensors and Actuators B: Chemical*, vol. 135, no. 1, pp. 388–397, 2008.

[74] T. W. Remmerbach, F. Wottawah, J. Dietrich, B. Lincoln, C. Wittekind, and J. Guck, "Oral cancer diagnosis by mechanical phenotyping," *Cancer Research*, vol. 69, no. 5, p. 1728, 2009.

[75] F. Lautenschläger, S. Paschke, S. Schinkinger, A. Bruel, M. Beil, and J. Guck, "The regulatory role of cell mechanics for migration of differentiating myeloid cells," *Proceedings of the National Academy of Sciences*, vol. 106, no. 37, p. 15696, 2009.

[76] J. Guck, R. Ananthakrishnan, H. Mahmood, T. J. Moon, and C. C. Cunningham, "The optical stretcher: a novel laser tool to micromanipulate cells," *Biophysical Journal*, vol. 81, pp. 767–784, August 2001.

[77] J. Guck, R. Ananthakrishnan, C. C. Cunningham, and J. Käs, "Stretching biological cells with light," *Journal of Physics: Condensed Matter*, vol. 14, pp. 4843–4856, 2002.

[78] T. W. Remmerbach, F. Wottawah, J. Dietrich, B. Lincoln, C. Wittekind, and J. Guck, "Oral cancer diagnosis by mechanical phenotyping," *Cancer Research*, vol. 69, no. 5, pp. 1728–1732, 2009.

[79] K. S. Furukawa, T. Ushida, T. Nagase, H. Nakamigawa, T. Noguchi, T. Tamaki, J. Tanaka, and T. Tateishi, "Quantitative analysis of cell detachment by shear stress," *Materials Science and Engineering: C*, vol. 17, no. 1-2, pp. 55–58, 2001.

[80] C. Dong and X. X. Lei, "Biomechanics of cell rolling: shear flow, cell-surface adhesion, and cell deformability," *Journal of Biomechanics*, vol. 33, no. 1, pp. 35–43, 2000.

[81] J. W. Song, W. Gu, N. Futai, K. A. Warner, J. Nor, and S. Takayama, "Computer-controlled microcirculatory support system for endothelial cell culture and shearing," *Analytical Chemistry*, vol. 77, pp. 3993–3999, 2005.

[82] E. W. K. Young, A. R. Wheeler, and C. A. Simmons, "Matrix dependent adhesion of vascular and valvular endothelial cells in microfluidic channels," *Lab on a Chip*, vol. 7, pp. 1759–1766, 2007.

117

[83] E. Tkachenko, E. Gutierrez, M. H. Ginsberg, and A. Groisman, "An easy to assemble microfluidic perfusion device with a magnetic clamp," *Lab on a Chip*, vol. 9, pp. 1085–1095, 2009.

[84] H. Lu, L. Y. Koo, W. M. Wang, D. A. Lauffenburger, L. G. Griffith, and K. F. Jensen, "Microfluidic shear devices for quantitative analysis of cell adhesion," *Analytical Chemistry*, vol. 76, no. 18, pp. 5257–5264, 2004.

[85] J. K. Tsou, R. M. Gower, H. J. Ting, U. Y. Schaff, M. F. Insana, A. G. Passerini, and S. I. Simon, "Spatial regulation of inflammation by human aortic endothelial cells in a linear gradient of shear stress," *Microcirculation*, vol. 15, no. 4, pp. 311–323, 2008.

[86] D. J. Quinn, I. Pivkin, S. Y. Wong, K. H. Chiam, M. Dao, G. E. Karniadakis, and S. Suresh, "Combined simulation and experimental study of large deformation of red blood cells in microfluidic systems," *Annals of Biomedical Engineering*, vol. 39, no. 3, pp. 1041–1050, 2011.

[87] A. K. Harris, P. Wild, and D. Stopak, "Silicone rubber substrata: a new wrinkle in the study of cell locomotion," *Science*, vol. 208, no. 4440, pp. 177–179, 1980.

[88] S. Munevar, Y. li Wang, and M. Dembo, "Traction force microscopy of migrating normal and H-ras transformed 3T3 fibroblasts," *Biophysical Journal*, vol. 80, pp. 1744–1757, April 2001.

[89] N. Q. Balaban, U. S. Schwarz, D. Riveline, P. Goichberg, G. Tzur, I. Sabanay, D. Mahalu, S. safran, A. Bershadsky, L. Addadi, and B. Geiger, "Force and focal adhesion assembly: a close relationship studied using elastic micropatterned substrates," *Nature Cell Biology*, vol. 3, pp. 466–472, May 2001.

[90] C. G. Galbraith and M. P. Sheetz, "A micromachined device provides a new bend on fibroblast traction forces," *Proceedings of the National Academy of Sciences*, vol. 94, no. 17, p. 9114, 1997.

[91] J. L. Tan, J. Tien, D. M. Pirone, D. S. Gray, K. Bhadriraju, and C. S. Chen, "Cells lying on a bed of microneedles: An approach to isolate mechanical force," in *Proceedings of the National Academy of Sciences*, vol. 100, USA, February 2003, pp. 1484–1489.

[92] O. du Roure, A. Saez, A. Buguin, R. H. Austin, P. Chavrier, P. Silberzan, and B. Ladoux, "Force mapping in epithelial cell migration," *Proceedings of the National Academy of Sciences*, vol. 102, no. 7, pp. 2390–2395, February 15 2005.

[93] S. Petronis, J. Gold, and B. Kasemo, "Microfabricated force-sensitive elastic substrates for investigation of mechanical cell-substrate interactions," *Journal of Micromechanics and Microengineering*, vol. 13, no. 6, pp. 900–913, 2003.

[94] Y. Zhao and X. Zhang, "Cellular mechanics study in cardiac myocytes using PDMS pillars array," *Sensors and Actuators A: Physical*, vol. 125, no. 2, pp. 398 – 404, 2006.

[95] J. le Digabel, M. Ghibaudo, L. Trichet, A. Richert, and B. Ladoux, "Microfabricated substrates as a tool to study cell mechanotransduction," *Medical and Biological Engineering and Computing*, vol. 48, no. 10, pp. 965–976, 2010.

[96] S. J. Han and N. J. Sniadecki, *Cellular and Biomolecular Mechanics and Mechanobiology.* Springer Verlag, 2011, ch. Nanotechnology Usages for cellular adhesion and traction forces, pp. 177–198.

[97] S. Yang and T. Saif, "Reversible and repeatable linear local cell force response under large stretches," *Experimental Cell Research*, vol. 305, pp. 42–50, 2005.

[98] S. Yang and M. T. A. Saif, "Force response and actin remodeling (agglomeration) in fibroblasts due to lateral indentation," *Acta Biomaterialia*, vol. 3, no. 1, pp. 77–87, 2006.

[99] A. Gopal, Z. Luo, J. Y. Lee, K. Kumar, B. Li, K. Hoshino, C. Schmidt, P. S. Ho, and X. Zhang, "Nano-opto-mechanical characterization of neuron membrane mechanics under cellular growth and differentiation," *Biomedical Microdevices*, vol. 10, no. 5, pp. 611–622, 2008.

[100] D. B. Serrell, T. L. Oreskovic, A. J. Slifka, R. L. Mahajan, and D. S. Finch, "A uniaxial bioMEMS device for quantitative force-displacement measurements," *Biomedical Microdevices*, vol. 9, no. 2, pp. 267–275, 2007.

[101] D. B. Serrell, J. Law, A. J. Slifka, R. L. Mahajan, and D. S. Finch, "A uniaxial bioMEMS device for imaging single cell response during quantitative force-displacement measurements," *Biomedical Microdevices*, vol. 10, no. 6, pp. 883–889, 2008.

[102] J. Rajagopalan, A. Tofangchi, and S. M. T. A, "Drosophila neurons actively regulate axonal tension in vivo," *Biophysical Journal*, vol. 99, no. 10, pp. 3208–3215, 2010.

[103] S. Yang and M. T. A. Saif, "Microfabricated force sensors and their applications in the study of cell mechanical response," *Experimental Mechanics*, vol. 49, pp. 135–151, 2009.

[104] J. Rajagopalan, A. Tofangchi, and M. T. A. Saif, "Linear high-resolution bioMEMS force sensors with large measurement range," *Journal of Microelectromechanical Systems*, vol. 19, no. 6, pp. 1380–1389, 2010.

[105] R. Fior, S. Maggiolino, M. Lazzarino, and O. Sbaizero, "A new transparent bioMEMS for uni-axial single cell stretching," *Microsystem Technologies*, vol. 17, pp. 1581–1587, 2011.

119

[106] J. Polesel-Maris, L. Aeschimann, A. Meister, R. Ischer, E. Bernard, T. Akiyama, M. Giazzon, P. Niedermann, U. Staufer, R. Pugin *et al.*, "Piezoresistive cantilever array for life sciences applications," in *Journal of Physics: Conference Series*, vol. 61, no. 1.   Institute of Physics Publishing, 2007, pp. 955–959.

[107] G. Lin, R. E. Palmer, K. S. J. Pister, K. P. Roos, S. M. Inc, and R. P. Verdes, "Miniature heart cell force transducer system implemented in MEMS technology," *IEEE Transactions on Biomedical Engineering*, vol. 48, no. 9, pp. 996–1006, 2001.

[108] Y. Sun, D. P. Potasek, D. J. Bell, S. N. Fry, and B. J. Nelson, "Characterizing fruit fly flight behavior using a microforce sensor with a novel comb drive configuration," *Journal of Microelectromechanical Systems*, vol. 14, no. 1, pp. pp. 4–11, 2005.

[109] Y. Sun, K. T. Wan, K. P. Roberts, J. C. Bischof, and B. J. Nelson, "Mechanical property characterization of mouse zona pellucida," *IEEE transactions on nanobioscience*, vol. 2, no. 4, pp. 279–286, 2003.

[110] E. T. Enikov and B. J. Nelson, "Three-dimensional microfabrication for a multi-degree-of-freedom capacitive force sensor using fibre-chip coupling," *Journal of Micromechanics and Microengineering*, vol. 10, no. 4, pp. 492–497, 2000.

[111] F. Beyeler, A. Neild, S. Oberti, D. J. Bell, Y. Sun, J. Dual, and B. J. Nelson, "Monolithically fabricated microgripper with integrated force sensor for manipulating microobjects and biological cells aligned in an ultrasonic field," *Journal of Microelectromechanical Systems*, vol. 16, no. 1, pp. 7–15, 2007.

[112] S. Muntwuler, B. E. Kratochwil, F. Beleyer, and B. J. Nelson, "Monolithically integrated two-axis microtensile tester for the mechanical characterization of microscopic samples," *Journal of Microelectromechanical Systems*, vol. 19, no. 5, pp. 1223–1233, 2010.

[113] Y. Mizutani, M. Tsuchiya, S. Hiratsuka, and K. Kawahara, "Elasticity of living cells on a microarray during the early stages of adhesion measured by atomic force microscopy," *Japanese Journal of Applied Physics*, vol. 47, no. 7, pp. 6177–6180, 2008.

[114] S. Hiratsuka, T. Mizutani, M. Tsuchiya, K. Kawahara, H. Tokumoto, and T. Okajima, "The number distribution of complex shear modulus of single cells measured by atomic force microscopy," *Ultramicroscopy*, vol. 109, pp. 937–941, 2009.

[115] F. M. Sasoglu, A. J. Bohl, and B. E. Layton, "Design and microfabrication of a high-aspect-ratio PDMS microbeam array for parallel nanonewton force measurement and protein printing," *Journal of Micromechanics and Microengineering*, vol. 17, no. 3, pp. 623–632, 2007.

[116] F. M. Sasoglu, A. J. Bohl, K. B. Allen, and B. E. Layton, "Parallel force measurement with a polymeric microbeam array using an optical microscope and mi-

cromanipulator," *Computer Methos and Programs in Biomedicine*, vol. 93, no. 1, pp. 1–8, 2008.

[117] C. Moraes, Y. Sun, and C. A. Simmons, *Cellular and biomolecular mechanics and mechanobiology*, ser. Studies in mechanobiology, tissues engineering and biomaterials. Springer Verlag, 2011, no. 4, ch. Microfabricated devices for studying cellular biomechanics and mechanobiology, pp. 145–175.

[118] J. Voldman, "Electrical forces for microscale cell manipulation," *Annual Review of Biomedical Engineering*, vol. 8, pp. 425–454, 2006.

[119] K. König, H. Liang, M. W. Berns, and B. J. Tromberg, "Cell damage in near-infrared multimode optical traps as a result of multiphoton absorption," *Optics Letters*, vol. 21, no. 14, pp. 1090–1092, 1996.

[120] H. Liang, K. T. Vu, P. Krishnan, D. Trang, T. C. Shin, S. Kimel, and M. W. Berns, "Wavelength dependence of cell cloning efficiency after optical trapping," *Biophysical Journal*, vol. 70, pp. 1529–1533, 1996.

[121] K. C. Neuman, E. H. Chadd, K. Liou, G. F. Bergman, and S. M. Block, "Characterization of photodamage to Escherichia coli in optical traps," *Biophysical Journal*, vol. 77, pp. 2856–2863, 1999.

[122] E. J. G. Peterman, F. Gittes, and C. F. Schmidt, "Laser-induced heating in optical traps," *Biophysical Journal*, vol. 84, pp. 1308–1316, 2003.

[123] G. Lin, K. S. J. Pister, and K. P. Roos, "Surface micromachined polysilicon heart cell force transducer," *Journal of Microelectromechanical Systems*, vol. 9, no. 1, pp. 9–17, 2000.

[124] Y. Zhao, C. C. Lim, D. B. Sawyer, R. Liao, and X. Zhang, "Simultaneous orientation and cellular force measurements in adult cardiac myocytes using three-dimensional polymeric microstructures," *Cell Motility and the Cytoskeleton*, vol. 64, no. 9, pp. 718–725, 2007.

[125] A. Kajzar, C. M. Cesa, N. Kirchgessner, B. Hoffmann, and R. Merkel, "Toward physiological conditions for cell analyses: forces of heart muscle cells suspended between elastic micropillars," *Biophysical Journal*, vol. 94, no. 5, pp. 1854–1866, 2008.

[126] M. Lekka, P. Laidler, D. Gil, J. Lekki, Z. Stachura, and A. Z. Hrynkiewicz, "Elasticity of normal and cancerous human bladder cells studies by scanning force microscopy," *European Biophysics Journal*, vol. 28, pp. 312–316, 1999.

[127] M. Zhao, C. Srinivasan, D. J. Burgess, and B. D. Huey, "Rate-and depth-dependent nanomechanical behavior of individual living Chinese hamster ovary cells probed by atomic force microscopy," *Journal of Materials Research*, vol. 21, no. 8, pp. 1906–1912, 2006.

[128] Q. S. Li, G. Y. H. Lee, C. N. ong, and C. T. Lim, "AFM indentation study of breast cancer cells," *Biochemical and Biophysical Research Communications*, vol. 374, pp. 609–613, 2008.

[129] S. E. Cross, Y.-S. Jin, J. Y. Rao, and J. K. Gimzewski, "Nanomechanical analysis of cells from cancer patients," *Nature Nanotechnology*, vol. 2, no. 12, pp. 780–783, 2007.

[130] S. E. Cross, Y.-S. Jin, Q.-Y. Lu, J. Y. Rao, and J. K. Gimzewski, "Green tea extract selectively targets nanomechanics of live metastatic cancer cells," *Nanotechnology*, vol. 22, p. 215101 (9pp), 2011.

[131] J. L. Maciaszek and G. Lykotrafitis, "Sickle cell trait human eythrocytes are significantly stiffer than normal," *Journal of Biomechanics*, vol. 44, pp. 657–661, 2011.

[132] J. L. Maciaszek, B. Andemariam, and G. Lykotrafitis, "Microelasticity of red blood cells in sickle cell disease," *Journal of Strain Analysis for Engineering Design*, vol. 44, no. 5, pp. 368–379, 2011.

[133] P. Carl and H. Schillers, "Elasticity measurement of living cells with an atomic force microscope: data acquisition and processing," *Pfügers Archiv European Journal of Physiology*, vol. 457, no. 2, pp. 551–559, 2008.

[134] M. M. Brandão, A. Fontes, M. L. Barjas-Castro, L. C. Barbosa, F. F. Costa, C. L. Cesar, and S. T. O. Saad, "Optical tweezers for measuring red blood cell elasticity: application to the study of drug response in sickle cell disease," *European Journal of Haematology*, vol. 70, no. 4, pp. 207–211, 2003.

[135] C. Rotsch and M. Radmacher, "Drug-induced changes of cytoskeletal structure and mechanics in fibroblasts: an atomic force microscopy study," *Biophysical Journal*, vol. 78, no. 1, pp. 520–535, 2000.

[136] M. Lekka and P. Laidler, "Applicability of AFM in cancer detection," *Nature Nanotechnology*, vol. 4, p. 72, 2009.

[137] J. M. A. Mauritz, T. Tiffert, R. Seear, F. Lautenschläger, A. Esposito, V. L. Lew, J. Guck, and C. F. Kaminski, "Detection of plasmodium falciparum-infected red blood cells by optical stretching," *Journal of Biomedical Optics*, vol. 15, no. 3, p. 030517 (3pp), 2010.

[138] B. Ilic, H. G. Craighead, S. Krylov, W. Senaratne, C. Ober, and P. Neuzil, "Attogram detection using nanoelectromechanical oscillators," *Journal of Applied Physics*, vol. 95, p. 3694 (10pp), 2004.

[139] Y. T. Yang, C. Callegari, X. L. Feng, K. L. Ekinci, and M. L. Roukes, "Zeptogram-scale nanomechanical mass sensing," *Nano Letters*, vol. 6, no. 4, pp. 583–586, 2006.

[140] A. Pillarisetti, W. Anjum, J. P. Desai, G. Friedman, and A. D. Brooks, "Force feedback interface for cell injection," in *Joint Eurohaptics Conference and Symposium on Haptic Interfaces for Virtual Environment and Teleoperator Systems*, Pisa, Italy, March 18-20, 2005, pp. 391–400.

[141] L. N. Virgin, *Vibration of axially loaded structures*. Cambridge University Press, 2007.

[142] H. P. Lee, "Effects of initial shapes on the natural frequencies of a beam with initial curvature and axial constraints," *Mechanics Reasearch Communications*, vol. 21, no. 6, pp. 593–598, 1994.

[143] S. Emam, "A theoretical and experimental study of nonlinear dynamics of buckled beams," Ph.D. dissertation, Virginia Polytechnic Institute and State University, 2002.

[144] G. Venkateswara Rao and K. Kanaka Raju, "Large amplitude free vibrations of beams - an energy approach," *Zeitschrift für Angewandte Mathematik und Mechanik*, vol. 83, no. 7, pp. 493–498, 2003.

[145] H. Nouira, E. Foltête, L. Hirsinger, and S. Ballandras, "Investigation on the effects of air on the dynamic behavior of a small cantilever beam," *Journal of Sound and Vibration*, vol. 305, pp. 243–260, 2007.

[146] F. J. Elmer and M. Dreier, "Eigenfrequencies of a rectangular atomic force microscope cantilever in a medium," *Journal of Applied Physics*, vol. 81, no. 12, pp. 7709–7714, 1997.

[147] S. Kirstein, M. Mertesdorf, and M. Schönhoff, "The influence of a viscous fluid on the vibration dynamics of scanning near-field optical microscopy fiber probes and atomic force microscopy cantilevers," *Journal of Applied Physics*, vol. 84, no. 4, pp. 1782–1790, 1998.

[148] J. Sader, "Frequency response of cantilever beams immersed in viscous fluids with applications to the atomic force microscope," *Journal of Applied Physics*, vol. 84, p. 64, 1998.

[149] V. De Salvo, G. Muscolino, and A. Palmeri, "A substructure approach tailored to the dynamic analysis of mult-span continuous beams under moving loads," *Journal of Sound and Vibration*, vol. 329, no. 15, pp. 3101–3120, 2010.

[150] A.-S. Rollier, "Technologies microsystèmes avancées pour le fonctionnement de dispositifs en milieu liquide et les applications nanométriques," Ph.D. dissertation, Université des Sciences et Technologies de Lille - Lille I, 2006.

[151] C. Riesch, E. K. Reichel, A. Jachimowicz, J. Schalko, P. Hudek, B. Jakoby, and F. Keplinger, "A suspended plate viscosity sensor featuring in-plane vibration and piezoresistive readout," *Journal of Micromechanics and Microengineering*, vol. 19, p. 075010, 2009.

[152] A. Maali, C. Hurth, R. Boisgard, C. Jai, T. Cohen-Bouhacina, and J. Aimé, "Hydrodynamics of oscillating atomic force microscopy cantilevers in viscous fluids," *Journal of Applied Physics*, vol. 97, p. 074907, 2005.

[153] S. Beeby, G. Ensell, M. Kraft, and N. White, *MEMS Mechanical Sensors.* Artech House, Inc., 2004.

[154] Y. H. Park and K. C. Park, "High-fidelity modeling of MEMS resonators. part ii. coupled beam-substrate dynamics and validation," *Journal of Microelectromechanical Systems*, vol. 13, no. 2, pp. 248–257, 2004.

[155] J. Vignola, J. Judge, J. Jarzynski, M. Zalalutdinov, B. Houston, and J. Baldwin, "Effect of viscous loss on mechanical resonators designed for mass detection," *Applied Physics Letters*, vol. 88, p. 041921, 2006.

[156] J. Judge, D. Photiadis, J. Vignola, B. Houston, and J. Jarzynski, "Attachment loss of micromechanical and nanomechanical resonators in the limits of thick and thin support structures," *Journal of Applied Physics*, vol. 101, p. 013521, 2007.

[157] J. Seo and O. Brand, "High q-factor in-plane-mode resonant microsensor platform for gaseous/liquid environment," *Journal of Microelectromechanical Systems*, vol. 17, no. 2, pp. 483–493, 2008.

[158] A. Herrera-May, L. Aguilera-Cortés, P. García-Ramírez, and E. Manjarrez, "Resonant magnetic field sensors based on MEMS technology," *Sensors*, vol. 9, no. 10, pp. 7785–7813, 2009.

[159] H. Tilmans, M. Elwenspoek, and J. Fluitman, "Micro resonant force gauges," *Sensors and Actuators A: Physical*, vol. 30, no. 1-2, pp. 35–53, 1992.

[160] C. Vancûra, I. Dufour, S. M. Heinrich, F. Josse, and A. Hierlemann, *Sensors and Actuators A: Physical*, vol. 141, pp. 43–51, 2008.

[161] D. S. Randall, M. J. Rudkin, A. Cheshmehdoost, and B. E. Jones, "A pressure transducer using a metallic triple-beam tuning fork," *Sensors and Actuators A: Physical*, vol. 60, no. 1-3, pp. 160–162, 1997.

[162] T. Yan, B. E. Jones, R. T. Rakowski, M. J. Tudor, S. P. Beeby, and N. M. White, "Design and fabrication of thick-film PZT-metallic triple beam resonators," *Sensors and Actuators A: Physical*, vol. 115, no. 2-3, pp. 401–407, 2004.

[163] A. Torrents, K. Azgin, S. W. Godfrey, E. S. Topalli, T. Akin, and L. Valdevit, "MEMS resonant load cells for micro-mechanical test frames: feasibility study and optimal design," *Journal of Micromechanics and Microengineering*, vol. 20, p. 125004, 2010.

[164] C. Barthod, Y. Teisseyre, C. Gehin, and G. Gautier, "Resonant force sensor using a PLL electronic," *Sensors and Actuators A: Physical*, vol. 104, no. 2, pp. 143–150, 2003.

[165] K. Fukuzawa, T. Ando, M. Shibamoto, Y. Mitsuya, and H. Zhang, "Monolithically fabricated double-ended tuning fork based force sensor," *Journal of Applied Physics*, vol. 99, p. 094901 (5pp), 2006.

[166] T. Hayashi, Y. Katase, K. Ueda, T. Hoshino, H. Suzawa, and M. Kobayashi, "Evaluation of tuning fork type force transducer for use as a transfer standard," *Measurement*, vol. 41, no. 9, pp. 941–949, 2008.

[167] T. Hoshino, T. Konno, K. Ishihara, and K. Morishima, "A nano-needle interface self-assembled by using cell migration for recording intracellular activity: Nano-needle durability," in *2nd IEEE RAS & EMBS International Conference on Biomedical Robotics and Biomechatronics (BioRob)*, Scottsdale, AZ, USA, October 2008, pp. 506–510.

[168] W. Ryu, Z. Huang, J. S. Park, J. Moseley, A. R. Grossman, R. J. Fasching, and F. B. Prinz, "Open micro-fluidic system for atomic force microscopy-guided in situ electrochemical probing of a single cell," *Lab on a Chip*, vol. 8, pp. 1460–1467, 2008.

[169] W. Ryu, S.-J. Bai, J. S. Park, Z. Huang, J. Moseley, T. Fabian, R. J. Fasching, A. R. Grossman, and F. B. Prinz, "Direct extraction of photosynthetic electrons from single algal cells by nanoprobing system," *Nano Letters*, vol. 10, pp. 1137–1143, 2010.

[170] S.-J. Bai, W. Ryu, R. J. Fasching, A. R. Grossman, and F. B. Prinz, "In vivo O_2 measurement inside single photosynthetic cells," *Biotechnology Letters*, vol. 33, pp. 1675–1681, 2011.

[171] T. P. Burg and S. R. Manalis, "Suspended microchannel for biomolecular detection," *Applied Physics Letters*, vol. 83, no. 13, pp. 2698–2700, 2003.

[172] V. Agache, G. Blanco-Gomez, F. Baleras, and P. Caillat, "An embedded microchannel in a MEMS plate resonator for ultrasensitive mass sensing in liquid," *Lab on a Chip*, 2011.

[173] J. Lee, R. Chunara, W. Shen, K. Payer, K. Babcock, T. P. Burg, and S. R. Manalis, "Suspended microchannel resonators with piezoresisitve sensors," *Lab on a Chip*, vol. 11, pp. 645–651, 2011.

[174] C. H. Edwards, "Ladders, moats and Lagrange multipliers," *The Mathematica Journal*, vol. 4, no. 1, pp. 48–52, 1994.

[175] G. Venkateswara Rao and K. Kanaka Raju, "Large amplitude vibrations of spring hinged beams," *AIAA Journal*, vol. 40, no. 9, pp. 1912–1914, 2002.

[176] H. Itoh, Y. Aoshima, and T. Egawa, "Model for a quartz-crystal tuning fork using torsion spring at the joint of the arm and the base and analysis of its frequency," *Japanese Journal of Applied Physics*, vol. 41, pp. 3422–3425, 2002.

[177] Y. C. Hu, P. Z. Chang, and W. C. Chuang, "An approximate analytical solution to the pull-in voltage of a micro bridge with an elastic boundary," *Journal of Micromechanics and Microengineering*, vol. 17, pp. 1870–1876, 2007.

[178] D. J. Morris, J. M. Yougsman, M. J. Anderson, and D. F. Bahr, "A resonant frequency tunable, extensional mode piezoeletric vibration harvesting mechanism," *Smart Materials and Structures*, vol. 17, p. 065021 (8pp), 2008.

[179] N. Lobontiu, *Dynamics of Microelectromechanical Systems*, ser. Microsystems. Springer, 2007, vol. 17, ch. 4, pp. 351–356.

[180] L. Nicu and C. Bergaud, "Modeling of a tuning fork biosensor based on the excitation of one particular resonance mode," *Journal of Micromechanics and Microengineering*, vol. 2004, pp. 727–736, 14.

[181] J. Seo and O. Brand, "High Q-factor in-plane-mode resonant microsensor platform for gaseous/liquid environment," *Journal of Microelectromechanical Systems*, vol. 17, no. 2, pp. 483–493, 2008.

[182] J. Shieh, J. E. Huber, N. A. Fleck, and M. F. Ashby, "The selection of sensors," *Progress in Materials Science*, vol. 46, pp. 461–504, 2001.

[183] D. J. Bell, T. J. Lu, N. A. Fleck, and S. M. Spearing, "MEMS actuators and sensors: observations on their performance and selection for purpose," *Journal of Micromechanics and Microengineering*, vol. 15, pp. S153–S164, 2005.

[184] M. D. Barrett, E. H. Peterson, and J. W. Grant, "Extrinsic Fabry–Perot interferometer for measuring the stiffness of ciliary bundles on hair cells," *IEEE Transactions on Biomedical Engineering*, vol. 46, pp. 331–339, 1999.

[185] H. C. Seat, E. Ouisse, E. Morteau, and V. Métivier, "Vibration–displacement measurements based on a polarimetric extrinsic fibre Fabry–Perot interferometer," *Measurement Science and Technology*, vol. 14, pp. 710–716, 2003.

[186] C.-J. Lin and F.-G. Tseng, "A micro Fabry–Perot sensor for nano-lateral displacement sensing with enhanced sensitivity and pressure resistance," *Sensors and Actuators A: Physical*, vol. 113, pp. 12–19, 2004.

[187] C. Prelle, F. Lamarque, and P. Revel, "Reflective optical sensor for long-range and high-resolution displacements," *Sensors and Actuators A: Physical*, vol. 127, no. 1, pp. 139–146, 2006.

[188] J. B. Faria, "A theoretical analysis of the bifurcated fiber bundle displacement sensor," *IEEE Transactions on Instrumentation and Measurement*, vol. 47, no. 3, pp. 742–747, June 1998.

[189] H. Z. Yang, S. W. Harun, and H. Ahmad, "Displacement sensing with two asymmetrical inclined fibers," *Microwave and Optical Technology Letters*, vol. 52, no. 6, pp. 1271–1274, 2010.

126

[190] H. Wang, "Effects of fibre geometry on the modulation function of a reflective intensity modulation sensor," *Journal of Modern Optics*, vol. 43, no. 11, pp. 2355–2366, 1996.

[191] P. B. Buchade and A. D. Shaligram, "Simulation and experimental studies of inclined two fiber displacement sensor," *Sensors and Actuators A: Physical*, vol. 128, no. 2, pp. 312–316, 2006.

[192] H. Golnabi and P. Azimi, "Design and operation of a double-fiber displacement sensor," *Optics Communications*, vol. 281, no. 4, pp. 614–620, 2008.

[193] P. B. Buchade and A. D. Shaligram, "Influence of fiber geometry on the performance of two-fiber displacement sensor," *Sensors and Actuators A: Physical*, vol. 136, no. 1, pp. 199–204, 2007.

[194] G. Perrone and A. Vallan, "A low-cost optical sensor for noncontact vibration measurements," *IEEE Transactions on Instrumentation and Measurement*, vol. 58, pp. 1650–1656, May 2009.

[195] V. K. Kulkarni, A. S. Lalasangi, I. I. Pattanashetti, and U. S. Raikar, "Fiber optic micro-displacement sensor using coupler," *Journal of Optoelectronics and Advanced Materials*, vol. 8, no. 4, pp. 1610–1612, 2006.

[196] P. Polygerinos, L. D. Seneviratne, and K. Althoefer, "Modeling of light intensity-modulated fiber-optic displacement sensors," *IEEE Transactions on Instrumentation and Measurement Science and Technology*, vol. 60, no. 4, pp. 1408–1415, 2011.

[197] R. A. Barton, B. Ilic, S. S. Verbridge, B. R. Cypriany, J. M. Parpia, and H. G. Craighead, "Fabrication of a nanomechanical mass sensor containing a nanofluid channel," *Nano Letters*, vol. 10, pp. 2058–2063, 2010.

[198] C. Ayela and L. Nicu, "Micromachined piezoeletric membranes with high nomila quality factors in a newtonian liquid media: a lamb's model validation at the microscale."

[199] S. M. Dickinson, "The lateral vibration of slightly bent slender beams subject to prescribed axial end displacement," *Journal of Sound and Vibration*, vol. 68, no. 4, pp. 507–514, 1980.

[200] N. Yamaki and A. Mori, "Non-linear vibrations of a clamped beam with initial deflection and initial axial displacement, part i: Theory," *Journal of Sound and Vibration*, vol. 71, no. 3, pp. 333 – 346, 1980.

[201] I. Elishakoff, V. Birman, and J. Singer, "Influence of initial imperfections on non-linear free vibration of elastic bars," *Acta Mechanica*, vol. 55, no. 3, pp. 191–202, 1985.

[202] C. S. Kim and S. M. Dickinson, "The flexural vibration of slightly curved slender beams subject to axial end displacement," *Journal of Sound and Vibration*, vol. 104, no. 1, pp. 170–175, 1986.

[203] S. Bouwstra and B. Geijselaers, "On the resonance frequencies of microbridges," in *International Conference on Solid-State Sensors and Actuators (TRANSDUCERS'91)*. IEEE, 1991, pp. 538–542.

[204] F. Treyssède, "Vibration analysis of horizontal self-weighted beams and cables with bending stiffness subjected to thermal loads," *Journal of Sound and Vibration*, vol. 329, no. 9, pp. 1536–1552, 2010.

[205] M. Boukallel, M. Girot, and S. Régnier, "Characterization of cellular mechanical behavior at the microscale level by a hybrid force sensing device," *Journal of the Mechanical Behavior of Biomedical Material*, vol. 2, no. 3, pp. 297–304, 2009.

[206] K. K. Liu, D. R. Williams, and B. J. Briscoe, "The large deformation of a single micro-elastomeric sphere," *Journal of Physics D: Applied Physics*, vol. 31, pp. 294–303, 1998.

[207] N. Caille, O. Thoumine, Y. Tardy, and J.-J. Meister, "Contribution of the nucleus to the mechanical properties of endothelial cells," *Journal of Biomechanics*, vol. 35, no. 2, pp. 177–187, 2002.

[208] V. Lulevich, T. Zink, H.-Y. Chen, F.-T. Liu, and G.-y. Liu, "Cell mechanics using atomic force microscopy-based single-cell compression," *Langmuir*, vol. 22, no. 19, pp. 8151–8155, 2006.

[209] Y. Murayama, C. E. Constantinou, and S. Omata, "Development of tactile mapping system for the stiffness characterization of tissue slice using novel tactile sensing technology," *Sensors and Actuators A: Physical*, vol. 120, pp. 543–549, 2005.

[210] O. A. Lindahl, C. E. Constantinou, A. Eklund, Y. Murayama, P. Hallberg, and S. Omata, "Tactile resonance sensors in medicine," *Journal of Medical Engineering & Technology*, vol. 33, no. 4, pp. 263–273, 2009.

[211] V. Jalkanen, "Hand-held resonance sensor for tissue stiffness measurements—a theoretical and experimental analysis," *Measurement Science and Technology*, vol. 21, p. 055801 (8pp), 2010.

[212] M. Radmacher, "Measuring the elastic properties of biological samples with the AFM," *IEEE Engineering in Medicine and Biology Magazine*, vol. 16, no. 2, pp. 47–57, 1997.

[213] I. Sokolov, *Cancer Nanotechnology*. American Scientific Publishers' Inc., 2006, ch. Atomic Force Microscopy in cancer cell research, pp. 1–17.

[214] T. G. Kuznetsova, M. N. Starodubtseva, N. I. Yegorenkov, S. A. Chizhik, and R. I. Zhdanov, "Atomic force microscopy probing of cell elasticity," *Micron*, vol. 38, no. 8, pp. 824–833, 2007.

[215] K. Liu, "Deformation behaviour of soft particles: a review," *Journal of Physics D: Applied Physics*, vol. 39, p. R189, 2006.

[216] A. B. Mathur, A. M. Collinsworth, W. M. Reichert, W. E. Kraus, and G. A. Truskey, "Endothelial, cardiac muscle and skeletal muscle exhibit different viscous and elastic properties as determined by atomic force microscopy," *Journal of Biomechanics*, vol. 34, no. 12, pp. 1545–1553, 2001.

[217] Y. Murayama, C. E. Constantinou, and S. Omata, "Micro-mechanical sensing platform for the characterization of the elastic properties of the ovum via uniaxial measurement," *Journal of Biomechanics*, vol. 37, pp. 67–72, 2004.

[218] J. B. Bureau, "Conception, réalisation de micro-capteurs de force à base de jauges piézo-resistives pour la caractérisation mécanique dássemblageg cellulaires en milieu liquide," Ph.D. dissertation, Université de Sciences et Technologies de Lille, 2006.

[219] S. P. Beeby and M. J. Tudor, "Modelling and optimization of micromachined silicon resonators," *Journal of Micromechanics and Microengineering*, vol. 5, pp. 103–105, 1995.

[220] F. Shaker, "Effect of axial load on mode shapes and frequencies of beam," NASA, Lewis Research Center, Tech. Rep., 1975.

[221] A. Bokaian, "Natural frequencies of beams under compressive axial loads," *Journal of Sound and Vibration*, vol. 126, no. 1, pp. 49–65, 1988.